Numerical Investigations of a High Frequency Pulsed Gaseous Fuel Jet Injection into a Supersonic Crossflow

A Dissertation Presented for the
Doctor of Philosophy
Degree
The University of Tennessee, Knoxville

Nehemiah Joel Williams
August 2016

Copyright © 2016 by Nehemiah Joel Williams
All rights reserved.

Acknowledgements

The author would like to express personal gratitude to several individuals who have made this work possible: Committee Chair Dr. Trevor Moeller, and committee members Dr. Roy Schulz, Dr. James Simonton and Dr. Phuriwat Anusoni-Inthra. Dr. Phuriwat allowed the use of UTSI's server for which the author is grateful. The author would also like to express gratitude to Dr. Charles Merkel and Dr. Joseph Schetz for their constructive and critical advice and suggestions on the technical aspects of modeling and analysis. Dr. Richard Joel Thompson has also provided significant advice and support on approaches to Computational Fluid Dynamics modeling approaches and generic support through friendship. UTSI IT Department technician Kanawful Mansangile has also produced significant technical support on running the UTSI computational machines. Finally, the author wants to thank two very important people in his life, his parents, Dallas and Deborah Williams for their undying and faithful support in the accomplishment of this study. The author is very thankful to these individuals for their invaluable efforts in allowing continued use of the computer server devices.

Abstract

The investigation of fuel delivery mechanisms is a critical design point in the development of supersonic combustion ramjet (scramjet) technology. Primary challenges include proper penetration of the jet in the supersonic crossflow while keeping total pressure losses and wall drag to a minimum. To reduce drag and heat loads especially at high burner entry Mach numbers it is desirable to use a minimally intrusive means of fuel delivery.

Pulsation of gaseous jets has been shown to increase penetration and mixing in subsonic flows. A limited number of experimental studies and even fewer numerical studies have suggested that when applied to supersonic crossflows, gaseous jets pulsed in the kilohertz range of frequencies improve jet penetration and mixing. To improve on the limited number of numerical studies of pulsed jets in supersonic crossflows (PJISF), 2D and 3D computational fluid dynamics (CFD) simulation models of non-excited (steady) and sinusoidally excited (pulsed) jets were constructed using ANSYS FLUENT 15.0. The 2D investigation included pulsation at 8, 16, 32 and 48 kHz. These simulation results showed that pulsation at 16 kHz provided the best jet penetration improvement in the jet near field and far field among all frequencies sampled.

A 3D wall-modeled Large Eddy Simulation (WMLES) was constructed with the goals resolving large scale turbulent flow structure and observing the time evolution of a jet pulsed in a supersonic crossflow, as well as to compare the effects of sinusoidal pulsation at 16 kHz with steady injection for the same flow conditions as the 2D case. A comparison of the jet trajectories between the steady and pulsed injection cases demonstrated that for sinusoidal pulsation of a jet at 16 kHz over the equivalent cycle averaged injection total pressure and momentum flux ratio, jet penetration is improved over the steady jet, up to 50% in the near field of the jet. Furthermore, improved mass concentration decay associated with

jet-crossflow mixing and far field total pressure recovery has been demonstrated as a result of pulsation of the jet.

Table of Contents

1 Introduction 1
1.1 Motivation and background 1
1.2 Physical Descriptions of Jets in Supersonic Crossflows 2
1.3 Summary of Studies of JISF 5
1.3.1 JISF Penetration Studies 5
1.3.2 JISF Trajectory Studies 6
1.3.3 Studies of JISF Turbulent Flow Structures and Mixing 8
1.3.4 Mixing Metrics 11
1.4 Mixing Performance Enhancement Studies 13
1.4.1 Passive Mixing Enhancements 13
1.4.2 Active Mixing Enhancements: Unsteady Jets 17
1.5 Problem Description and Primary Motivation 33
1.6 Primary Investigations 34
1.6.1 Thesis Statement and General Description of Study 34
1.6.2 Proposed Research Objectives and Focus 35
1.6.3 Research Approach and Specific Contributions 36
2 Theoretical Foundations and Numerical Methodology 39
2.1 General Equations 39
2.1.1 Instantaneous Conservation Laws 39
2.1.2 Equations of State 40
2.1.3 Physical Description of Turbulence 40
2.2 Theory of Turbulence Modeling 44
2.2.1 Mathematical Description of Turbulent Flows 44
2.2.2 Turbulent Modeling Description 46
2.2.3 Favre Averaged and Filtered Governing Equations 48
2.2.4 Closure Description 51
2.2.5 Menter's SST Model 55
2.2.6 Large Eddy Simulations: Sub-Grid Scale Modeling 56
2.2.7 Detached Eddy Simulation Models 60
2.3 Numerical Methodology and Approach 62
2.3.1 Control Volume Approach and Cell-Flux Discretization 62
2.3.2 Spatial and Temporal Discretization 64
2.3.3 Derivative and Gradient Evaluation 65
2.3.4 Density Based Coupled Solver 66
2.3.5 Roe Flu*x*-Difference Splitting Scheme for Convective Fluxes 67
2.3.6 Implicit Time Stepping (Dual-Time formulation) 68
2.3.7 Algebraic Multi-Grid formulation 69

3 Preliminary Investigation: 2D Pulsed Injection 72
3.1 Generic Problem Description 72
3.2 2D Investigations 75
3.2.1 Problem Setup & Boundary/Initial Conditions 75
3.2.2 Numerical Methodology and Procedure 78
3.2.3 Grid Independence Study (16 kHz Forced Case) 80
3.3 2D Simulation Results 82
3.3.1 Pulsed Injection Characteristics at Various Frequencies 82
3.3.2 Time Evolution Characteristics of Pulsed Injection 86
3.4 2-D Simulation Results Summary 89
4 Primary Investigations (3D Studies) 90
4.1 Primary Investigation Overview 90
4.2 Problem Set up and physical model 92
4.2.1 Computational Domain and Case Setup 92
4.2.2 Grid Generation 94
4.2.3 Inflow and Boundary Layer Resolution Conditions 97
4.2.4 Modeling Approach 99
4.3 Baseline Case Results (Steady Injection, $J \sim 1$) 103
4.3.1 Instantaneous Flow Field 103
4.3.2 Time Averaged Flow Field 107
4.3.3 Quantitative Analysis and Theoretical Comparisons 111
4.4 Grid Independence Study 117
4.4.1 Instantaneous Results 117
4.4.2 Time Averaged Results 119
5 Characteristics of Pulsed Injection in a Supersonic Crossflow ($f = 16$ kHz) 122
5.1 Section Overview 122
5.2 Snapshot of Pulsed Injection Flow Environment 123
5.3 Time Evolution of the Pulsed Jet (f = 16 kHz) 126
5.4 Time Averaged Characteristics of Pulsed Injection 133
5.5 Theoretical Trajectory and Species Decay of Pulsed Injection 136
6 The Effects of Pulsed Injection on Jet Penetration and Mixing 139
6.1 Primary Investigation Overview 139
6.2 Comparisons of Steady and Pulsed Injection 140
6.2.1 Instantaneous Results 140
6.2.2 Time Averaged Results 142
6.3 Performance Comparisons 144
6.4 Implications 148
7 Conclusions and Future Work 151
7.1 Primary Investigation Summary 151
7.2 Primary Accomplishments and Conclusions 152

7.3 Suggested Future work and Research Direction 154
List of References 156
Vita. 166

List of Tables

Table 1. Reynolds Number Based Grid Requirements 57
Table 2. Grid Resolution Comparison between LES and WMLES 60
Table 3: Flow Conditions for 2D Simulations 76
Table 4: Simulation Test Matrix for 2D simulation cases 77
Table 5: Flow Conditions for Baseline Case (*Steady Injection, J ~ 1*) 93
Table 6: Pulsation Characteristics (*Sinusoidal Injection, 16kHz, J_{cycle} ~1*) 93
Table 7: Grid Resolution Estimates (*Re_D = 18,400, D = 0.125"*) 95
Table 8: Stations comparing 1D Compressible Theory with CFD results 114
Table 9: Comparison of shock length and Mach disk with theory 116

List of Figures

Figure 1: Visual depictions of a JISF: (a) schlieren photograph of a JISF (unknown source), (b) conceptual diagram of primary flow structures of a JISF (reproduced from Gamba *et al.*) [8]. 3
Figure 2: 3D Visualizations of JISF: (a) 3D view of jet plume structure, (b) 3D view of shock structures (reproduced from Lin *et al.*) [9]. 4
Figure 3: Images of coherent structures in JISF: Schlieren images of hydrogen injection (a) and ethylene injection (b) in a supersonic crossflow of nitrogen. A visual diagram of the high and low shear velocities which cause the formation of LSV structures (c). All images are reproduced from Ben-Yakar *et al.* [17]. 10
Figure 4: Diagrams of passive mixing enhancement approaches: (a) unswept and swept injector ramps, (b) rear facing step with injector. Images reproduced from Drummond et al. [34] and Ben-Yakar et al [7]. 15
Figure 5: Mixing enhancement techniques: (a) Pressure contours from a CFD simulation of tandem injection with $J = 1$ at various injector spacing lengths (D5 and D7), (b) injection with an acoustic cavity diagram. Reproduced from Lee *et al.* [37] and Ben-Yakar *et al.* [7]. 16
Figure 6: Comparison of "unforced" and "forced" jet in crossflow: (a) jet with no acoustic excitation, (b) jet excited with square waveform at f = 73.5 Hz and duty cycle of 22%, (c) jet excited with sinusoidal waveform at f = 73.5 Hz. Reproduced from [47]. 19
Figure 7: Pulsed injection in supersonic crossflows: (a) schlieren image of pulsed jet at cycle time 0.26T, (b) mass fraction contours of pulsed injection. Reproduced from Cutler *et al.* [53] and Kouchi *et al.* [54]..... 21
Figure 8: Visualization of formation of vortex ring: (a) piston diagram with half – 'infinite' cylindrical vortex sheet roll up description, (b) vortex ring roll up and circulation conservation, (c) schlieren image of a vortex ring leaving an orifice. Reproduced from Gharib [66]. 24
Figure 9: Diagram of stroke ratio (L/D) as a function of dimensionless energy. Reproduced from Gharib [66]. 25
Figure 10: Pulsed jet regime map of distinct vortical structures as functions of velocity ratio, r and stroke ratio, L/D. Reproduced from Sau and Mahesh [70]. 29
Figure 11: Large and small scale structures in a round turbulent jet. Reproduced from Dimotakis [77]. 42
Figure 12: Computational domain and general flow conditions for 2D simulation cases. 75
Figure 13: 2D Simulation data: (a) instantaneous pulsed injection total pressure from time 0.1 to 1 *ms*, (b) plot of the residuals for 2D pulsed injection

simulation between 170,000 and 180,000 iterations. Both plots are from the medium grid (f = 16 kHz) case. 79
Figure 14: Results of grid independence study (t = *1 ms*, f = *16 kHz*): (a) Mach number contours and (b) vorticity contours are from the course (65k), medium (120k) and fine (450k) grids. 80
Figure 15: Comparison of time averaged mass concentration profiles for the course, medium and fine grids. Mean mass concentration of hydrogen is sampled at domain locations (a) x/D = *0*, (b) x/D = *10* and (c) x/D = *20.*..... 81
Figure 16: Comparison of steady and pulsed injection flow fields at frequencies (f = 8, 16, 32 and 48 kHz): (a) Mach number contours and (b) mass concentration contours. All images are displayed at the same instant in time (t = *1.344 ms*). 83
Figure 17: Time averaged mass concentration profiles of hydrogen for steady and pulsed jets (f = 8, 16, 32 and 48 kHz): (a) location x/D = *0*, (b) location x/D = *20* and (c) location x/D = *40*. 85
Figure 18: Time evolution of pulsed fuel jet in supersonic crossflow at 16 kHz: (a) prior to injection of current cycle (t/T =0), (b) at a quarter of a cycle (t/T = 0.25), (b) peak injection pressure (t/T = 0.5), at three quarters of a cycle (t/T = 0.75) and at the start of a new cycle (t/T = 1). Contours are of Mach number. 87
Figure 19: Mass concentration contours showing the large scale eddy rollup of the pulsed jet over one cycle (f = 16 kHz) at times (t/T = 0, 0.25, 0.5 and *0.75*). 88
Figure 20: Computational domain and flow conditions for the 3D numerical investigations. 92
Figure 21: Top view (a) and side view (b) of the block structured computational domain used in this study. Arrows indicate the crossflow direction (blue) and jet injection location (red). 94
Figure 22: An 'O' type block structured grid with high grid density near the injector nozzle. 96
Figure 23: Visualization of the application of a RANS turbulent inflow boundary condition. 97
Figure 24: Inflow velocity data at δ=*0.125"*: (a) Inflow velocity normalized with free stream velocity (U_c = *556* ms^{-1}), (b) Van Driest transformed velocity profile (blue lines) plotted against the log-law and the law of the wall [116]. 98
Figure 25: Convergence data from the steady state solution (a) and transient solution (b). 101
Figure 26: A comparison between the baseline case (Steady injection, J ~ *1*)(a) and typical features seen in JISF (b) [17]. Contours are of Mach number.

Simulation results sampled at time ($t = 0.3$ *ms*). Reproduced from Ben-Yakar *et al.* [17]. 104
Figure 27: A comparison between the baseline case (Steady injection, $J \sim 1$)(a) and the circumferential roller structures seen in JISF experiments [17]. An iso-surface of Q-criterion (s^{-1}) is colored with hydrogen mole fraction. Image (b) is reproduced from Ben-Yakar *et al.* [17]. 104
Figure 28: 3D simulation results from baseline case (Steady injection, J ~ 1): (a) Mach number contour of the JISF flow field in the central plane ($x/D < 10$), (b) *y-z* plane view at $x/D = 1$, (c) *x-z* plane view ($y/D = 1$) and (d) *y-z* plane view at $x/D = 10$. 105
Figure 29: 3D simulation results for baseline case (steady JISF, $J \sim 1$): (a) numerical schlieren image of the central plane ($x/D < 10$), (b) *y-z* plane view of hydrogen mole fraction at $x/D = 1$, (c) numerical schlieren of the x-z plane view ($y/D = 1$) and (d) mole fraction at $x/D = 10$. 106
Figure 30: Time averaged views of static pressure (a), RMS hydrogen mass fluctuations (b), hydrogen mass concentration in the *x-z* plane (c), and hydrogen mass concentration in the 108
Figure 31: Time averaged images of *x*-velocity (a) and *y*-velocity (a) normalized by the free stream velocity (U_c=556 ms^{-1}). 109
Figure 32: Mean normalized turbulent kinetic energy (TKE) (a) and mean normalized Reynolds stress distribution (b). TKE is normalized by the square of the free stream velocity ($U_c = 556$ ms^{-1}) 110
Figure 33: Penetration trajectories (based on 10% of the mean mass concentration profile) scaled with jet diameter (D) compared with Segal [3]. 111
Figure 34: Contours of Static Temperature (K) of the baseline case showing the labeled station locations (1, 2 and j) which correspond to the free stream, downstream of the bow shock and nozzle exit area locations. Data was sampled from these locations for comparison with 1D compressible theory. 114
Figure 35: Contours of Stagnation Temperature (K) showing the locations of the separation shock and Mach disk height. 116
Figure 36: Comparison of simulations results from 10M (left) and 17.8M cell grids. 118
Figure 37: Time averaged images of mass concentration (a-b) and mean velocity (c-d) for 10M and 17.8 M cell grid 119
Figure 38: Boundary Layer Profiles compared with theory for 10M and 17.8 M cell grids (taken from the location upstream of the nozzle injector $x/D = -1$). 120
Figure 39: Top: Contours of wall pressure normalized by the free stream local pressure for 10M and 17.8M grids. Bottom: Wall pressure distribution for 10M and 17.8M grids. 120

Figure 40: Instantaneous flow field of sinusoidal pulsed injection at f = 16 kHz. Pulse cycle time is t/T = 0.75. Contours are of (a) Mach number, (b) hydrogen mole fraction and (c) numerical schlieren. 123
Figure 41: Near field pulsed jet behavior ($x/D < 10$). Contour plots include numerical schlieren (a), velocity magnitude (b), hydrogen mass concentration(c) and vorticity (d). 125
Figure 42: Near field evolution of sinusoidal pulsed injection at 16 kHz over one full pulse cycle. Contours are of Mach number 127
Figure 43: Evolution of pulsed jet injection at 16 kHz over a full pulse cycle. Contours are of hydrogen mass fraction (left column), velocity (middle column) and vorticity (right column). Rows (a) – (e) represent the portions of the pulsation cycle (times t/T = 0 -1). 129
Figure 44: Iso-surfaces of Q-criterion (Q = 10^9 s^{-1}) during the rising (a), peak (b) and falling phase of a pulse cycle. Iso-surfaces include x-y plane views (left column), y-z plane vies (middle column) and (profile views of jet development). Contours are colored by vorticity (left and middle columns) and hydrogen mole fraction. 131
Figure 45: Jet penetration and shock structure at cycle time t/T = 0.5. Contours of Mach number (a) and hydrogen mass concentration of jet near field (b) are displayed in this frame 132
Figure 46: Time averaged views of pulsed injection: (a) and (b) are mean velocity and hydrogen mass concertation, (c) and (d) are RMS velocity and hydrogen mass concentration 133
Figure 47: Time averaged images of u-velocity and v-velocity (scaled with crossflow velocity U_c=556 ms^{-1}) (a-b), RMS u-velocity and RMS v-velocity (c-d). Time averaged turbulent kinetic energy (TKE) and Reynolds stress (e-f) of the PJISF. 135
Figure 48: Trajectory comparisons between Eq.(1-33) and the time averaged jet penetration of the pulsed jet. 136
Figure 49: Mass concentration decay curve (Eq. 1-36) [50] compared with current simulation results. 137
Figure 50: Comparison of steady (J~1) and pulsed injection (16 kHz) at (t = 0.134 ms). Contours shown are : (a) Mach number, (b) hydrogen mole fraction and (c) numerical schlieren. Pulse time is t/T = 0.75 141
Figure 51: Time averaged comparison of hydrogen mass concentration (top) and RMS of mass concentration (bottom) for steady (a,c) and pulsed (b,d) injection. 142
Figure 52: (Top): time averaged contours of RMS v-velocity for unforced and pulsed injection. (Bottom): turbulent kinetic energy (TKE) comparison between steady and pulsed injeection. 143

Figure 53: Top image: trajectory comparison between steady and pulsed injection cases. Bottom image: penetration improvement factor (PIF) trajectory. 145
Figure 54: Mass concentration decay plots comparing steady and pulsed cases. 146
Figure 55: Comparison of time averaged total pressure profiles for steady and pulsed injection: (a*) x/D = 10*, (b) *x/D =20* and (c) *x/D = 40*. Total pressure is normalized by the free stream value (*P_{tc} = 30 psi*)..... 147
Figure 56: Contours of instantaneous vorticity (a) and RMS hydrogen mass concetration (b) for pulsed injection displaying large regions of reciculation downwind of the wall injector 149
Figure 57: Comparison of instantaneous (*t = 0.3 ms*) mole fraction contours displaying the flammability limits of hydrogen for steady and pulsed injection at axial locations *x/D = 10* and *20*. 150

Nomenclature

English Symbols

A	Area
C	Mean Mass Concentration Decay
$C(x)$	Axial Mean Mass Concentration Decay
c	Concentration (of species)
$\bar{c}$	Mass Averaged Concentration
E	Energy
d, D	Jet Nozzle Diameter
F	Fuel-Air Ratio
F_{st}	Stoichiometric Fuel-Air Ratio
$\boldsymbol{F}$	Flux Vectory
f	Pulsation Frequency
H	Enthalpy
h	Height (e.g. Mach disk, wall)
J	Momentum Flux Ratio
J_{cycle}	Cycle Averaged Momentum Flux Ratio
k	Constant
k	Kinetic Energy (per unit mass)
L	Largest Length Scale
L_k	Kolmogorov Length Scale
L/D	Stroke Ratio
l	Mixing Length
l_s	Separation Shock Length
$\mathrm{M_w}$	Molecular Weight
M	Mach Number
$\dot{m}$	Mass Flow Rate
N	Number of Grid Points
T	Cycle Period
T	Temperature
T_c	Large Eddy Turnover Time
T_k	Kolmogorov Time Scale
T_i	Turbulence Intensity
P, p	Local Pressure
P_{eb}	Effective Back Pressure
P_{sep}	Pressure of Shock Separation Region
P_t	Total Pressure
$P_{t_{cycle}}$	Cycle Averaged Total Pressure

P_{tj}	Jet Total Pressure
P_{tA}	Pulsation Amplitude
$P_{tj}(t)$	Instantaneous Injection Total Pressure
P_{tj_P}	Peak Total Pressure
$\boldsymbol{Q}$	Second Invariant of the Velocity Tensor
$\overline{\boldsymbol{S}}$	Strain Rate Tensor
St	Strouhal Number
q	Dynamic Pressure
Re	Reynolds Number
Re_δ	Critical Reynolds Number
r	Velocity Ratio
r_e	Effective Velocity Ratio
U	Velocity
U_p	Peak Velocity
U_{ref}	Reference Velocity
$\overline{U}$	Mean Velocity
ΔU_j	Peak-to-peak Jet Velocity
ΔU_{rms}	Variance of RMS Velocity
$u(t)$	Instantaneous Velocity
u	x-direction Velocity
u_τ	Wall Friction Velocity
$\boldsymbol{u}$	Velocity Vector
V	Volume
V_k	Kolmogorov Velocity Scale
V_p	Vortex Puff Volume
v	v-direction Velocity
X_{H_2}	Mole Fraction (hydrogen)
x/D	Dimensionless Length in x-direction
Y_{H_2}	Mass Concentration (hydrogen)
$\bar{Y}_{max}$	Peak Mean Mass Concentration
y/D	Dimensionless Length in y-direction

Greek Symbols

α	Duty Cycle
Γ	Circulation
γ	Specific Heat Ratio
Δ	Grid spacing or cell dimension
δ	Boundary Layer Thickness
δ_{sh}	Shear Layer Thickness

$\overline{\boldsymbol{\delta}}$, δ_{ij}	Kronecker Delta Function
δ_p	Vortex Puff Diameter
ε	Eddy Dissipation Rate
Ω	Vorticity Magnitude
$\boldsymbol{\Omega}, \boldsymbol{\zeta}$	Vorticity Vector
η	Kolmogorov Micro-Scale Length
θ_{inj}	Wall Jet Injector Angle
λ	Bulk Viscosity
λ_t	Taylor Micro-Scale Length
μ	Dynamic Viscosity
μ_t	Turbulent Dynamic Viscosity
ν	Kinematic Viscosity
ν_T	Turbulent Kinematic Viscosity
ρ	Density
τ	Pulse Time ('on' time for given pulse)
$\overline{\boldsymbol{\tau}}$	Shear Stress Tensor
τ_w	Wall Shear Stress
φ	Generic Flow Property
ω	Turbulence Frequency

Subscripts and Superscripts

A	Amplitude
a	Region Downstream of Normal Shock
avg	Averaged Property
c	Cross Flow
$cycle$	Cycle Averaged Property
j	Injector Flow Property
$.^{sgs}$	Sub-Grid Scale Property
st	Stoichiometric Property
t	Total Flow Property
var	Variance of a Property
x	x direction
y	y direction
z	z direction
0	Free Stream Flow Property
1	Flow Property Upstream of Normal Shock
2	Flow Property Downstream of Normal Shock
$*$	Choked (Sonic) Flow Condition

∞	Free Stream Property
$\tilde{\cdot}$	Filtered Property
$\bar{\cdot}$	Averaged Property
$\nabla \cdot$	Divergence Operator
∇	Gradient Operator

Abbreviations

CVP	Counter-rotating Vortex Pair
ER	Equivalence Ratio
EVM	Linear Eddy Viscosity Model
DES	Detached Eddy Simulation
DNS	Direct Numerical Simulation
JICF	Jet in Crossflow
JISF	Jet in Supersonic Crossflow
MFP	Mixture Fraction Parameter
MP	Mixture Parameter
LES	Large Eddy Simulation
LSV	Large Scale Vortical Structure
NEVM	Non-linear Eddy Viscosity Model
PJISF	Pulsed Jet in Supersonic Crossflow
RANS	Reynolds Averaged Navier-Stokes
RMS	Root Mean Squared
RSM	Reynolds Stress Model
SGS	Sub-Grid Scale Model
TKE	Turbulent Kinetic Energy
WMLES	Wall Modeled Large Eddy Simulation
Eq(s).	Equation(s)
Ref(s).	Reference(s)
Sec(s).	Sections(s)

1 Introduction

1.1 Motivation and background

Supersonic Combustion Ramjets (scramjets) are a class of air-breathing engines which make use of high dynamic air pressure produced by inlet compression of high speed air flow to produce thrust. These engines generally operate at Mach numbers several times the speed of sound (Mach > 3). Though conceptually, scramjet technology has been in existence for over half a century, it still has not reached a point of technical maturation. Technical challenges including the efficient delivery of fuel (mixing and penetration) into the high speed core flow make scramjet propulsion still practically a futuristic technology despite decades of modeling, testing and experimentation to understand how to design an efficiently functioning system [1], [2], [3].

During the fuel injection process, the core of the air flow is traveling at supersonic speeds, and the residence time of the fuel-air combination in the combustion chamber is less than the time required for the propellant combination to mix and burn properly. This causes a reduction in performance which drastically affects the performance of the system. Several fuel injection schemes have been proposed to alleviate this problem including transverse injection behind ramps, ramp injection, strut injection, pylon injection [4], [5], [6]. In addition, acoustic cavities coupled with wall injectors have been demonstrated to produce

large recirculating flow zones which somewhat reduce the residence time of the propellant combination and act as flame holders [7].

Unfortunately, all the schemes produce significant drawbacks: transverse jets penetrate deeper into the flow but produce strong bow shocks which cause significant losses in total pressure. Fuel injection schemes involving pylons, ramps and struts must be carefully designed because an increase of the surface area in contact with the combustor air flow increase the amount of drag on the vehicle. The increase in drag on the internal combustor flow could reduce the amount of thrust produced by the engine which is detrimental to overall engine performance. Furthermore, for hypersonic vehicles traveling at Mach 5 or higher, the higher burner entry Mach numbers could produce strong localized heat loads on the protruding injector elements [5].

A mechanism which allows for deeper fuel penetration, reduction in drag, thermal and shock losses while still accelerating the mixing rates and residence time has yet to be demonstrated scientifically. Several papers have proposed minimally intrusive fuel injection penetration and mixing enhancements which are at least theoretically applicable to a wider range of operating conditions. These have included the use of unsteady or pulsed fuel injection [3], [4], [5], [6].

1.2 Physical Descriptions of Jets in Supersonic Crossflows

The flow field of a gaseous fuel jet injected into a supersonic free stream cross flow (JISF) is a rather complex region of shocks, expansion fans and turbulent vortical structures. Introducing an under-expanded jet into a supersonic cross flow causes the injected jet to behave as a blunt body, producing a bow shock upstream of the injection point. Immediately above the injection area, a barrel shock structure is formed, resulting from a Prandtl-Meyer expansion wave, which is recompressed into a Mach disk similar to those produced in jet engine and rocket

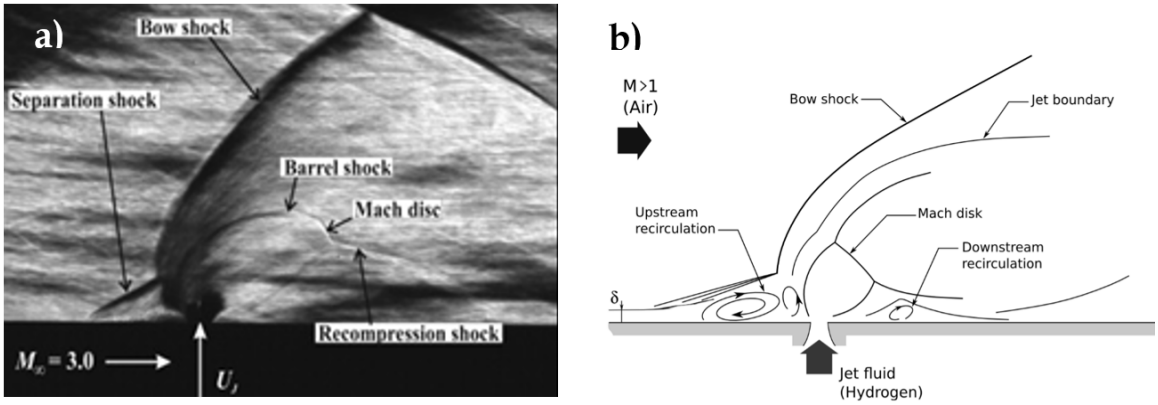


Figure 1: Visual depictions of a JISF: (a) schlieren photograph of a JISF (unknown source), (b) conceptual diagram of primary flow structures of a JISF (reproduced from Gamba *et al.*) [8]**.**

engine exhaust plumes. In cases where the jet pressure is significantly higher than the ambient pressure, the bow shock causes the boundary layer upstream of the injection port to separate, producing a separation shock structure.

Profile views of the jet injection field from Schlieren images such as those in Figure 1a reveal the prominent shock structures associated with a JISF including the separation shock, bow shock, barrel shock near the injector, the Mach disk and the resulting recompression shock immediately downstream of the Mach disk. The separation shocks produce re-circulation regions up-stream of the bow shock, and around it's perifery at the boundary (Figure 1b). As the jet is injected into the crossflow, the fluid structure becomes turbulent, and flow structures which are initially small at the injection site become larger. Large scale eddies are produced which entrain ambient fluid downstream of the injection site, promoting mixing between the jet and the surrounding crossflow.

The interaction field of a JISF is a strongly three-dimensional phenomena. In three-dimensional space, the bow shock actually forms a paraboloid around the jet region. The separated boundary layer and recirculation region around the base of the bow shock causes a reflected shock known as a λ-shock (due to its profile view shape) to form in that region. Inside the bow shock the jet receives momentum from the main flow causing its trajectory to change from vertical to

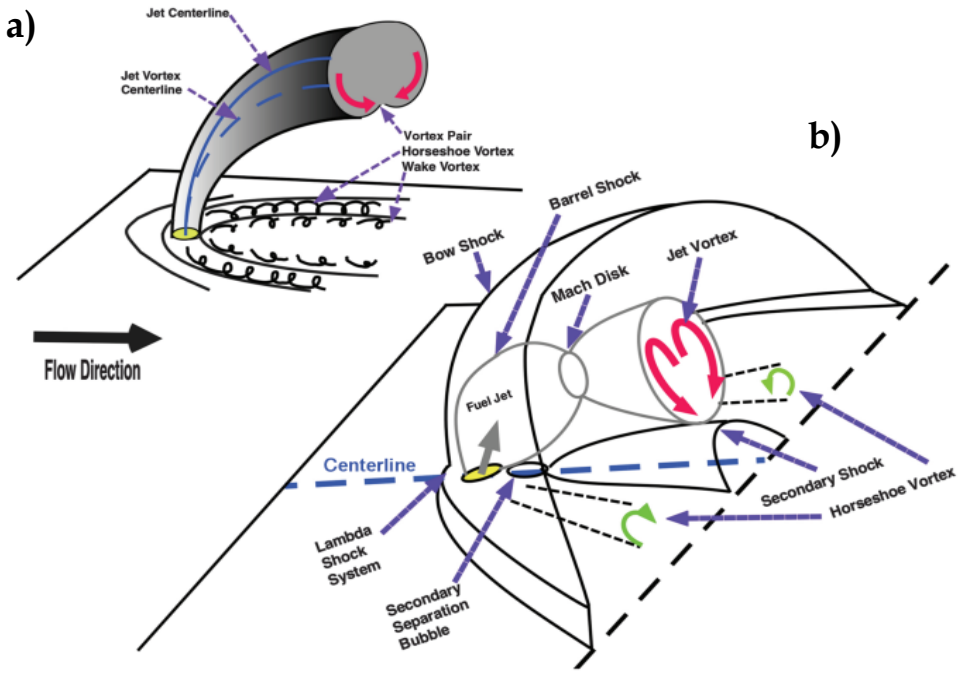


Figure 2: 3D Visualizations of JISF: (a) 3D view of jet plume structure, (b) 3D view of shock structures (reproduced from Lin *et al.*) [9].

eventually horizontal in a parabolic shape. Figure 2 shows a visualization of several 3D jet vortical and shock structures which are produced in a JISF: a horseshoe vortex region around the base of the jet, and a counter-rotating vortex pair (CVP) forms in the jet downstream of the injection site. The CVPs cause the jet flow to mix with the free stream flow.

Many studies from analytical, experimental and computational fluid dynamics (CFD) approaches have focused on several aspects of the JISF flow field, including Mach disk height (which was used in early studies as a measure of penetration), the jet's trajectory, and mixing characteristics the shock/boundary layer interactions and the production of vortices. The vortex production has been associated with mixing of the fuel jet/supersonic free stream flow. A summary of select JISF studies with an emphasis on jet penetration and mixing characteristics of injected jets is presented in the subsequent section.

1.3 Summary of Studies of JISF

In light of the two major challenges to supersonic fuel injection prior to combustion, namely penetration and mixing, many of the early analytical and experimental studies focus on attempting to quantify penetration of jets in supersonic cross-flows and also which fluid characteristics controlled the amount of penetration which occurred. Zukoski and Spaid [10] were among the first researchers to attempt to obtain a fundamental understanding of the physics of the interactions of various phenomena associated with injection of gaseous fluids into supersonic crossflows including developing similarity rules which describe jet fuel penetration [10].

1.3.1 JISF Penetration Studies

Looking at gaseous nitrogen, argon, and helium in free stream Mach numbers of 1.38 and 4.54, Zukoski and Spaid suggested the use of a scaling law which could measure the fuel jet penetration height, *h*, by locating the height of the Mach disk. Improvements were made on jet penetration models by Billig and Schetz [11] and Schetz *et al.* [12] via the introduction of the "effective back pressure" concept with an analogy to the simpler under-expanded jet in quiescent flow studied by Adamson [13] and later by Crist [14].

Effective back pressure (P_{eb}) is an approximation for the static pressure downstream of the jet emanating from the injector. Since it was difficult to determine P_{eb}, Billig and Schetz related P_{eb} to the stagnation pressure behind a normal shock (P_{ta_2}) and the pressure in the separated region ahead of the jet (P_{sep}) for flow condition in which the boundary layer thickness δ is not separated ($\delta/D < 1$) or is separated ($\delta/D > 1$) by the following:

$$P_{eb} = 0.5\left(P_{ta_2}\right) \tag{1-1}$$

when ($\delta/D < 1$) and

$$P_{eb} = 0.5\left(P_{sep}\right) \tag{1-2}$$

when ($\delta/D < 1$). Experimentation was performed by Schetz *et al.* [12] and Orth and Funk [15] to confirm the previous findings. Ashkenaz and Sherman [16] produced a relationship between Mach disk height, h, and effective back pressure P_{eb} in the following relationship:

$$\frac{h}{d_j} = 0.67\left(\frac{P_{tj}}{P_{eb}}\right)^{1/2} \tag{1-3}$$

where P_{tj} is the jet total pressure. This relationship was later shown to produce reasonable results in comparison to experiment [17].

1.3.2 JISF Trajectory Studies

Billig and Schetz developed a theory predicting the trajectory of a JISF using analytical theory based on forces acting on a differential jet element [18]. Orth and Funk verified the theory from Ref. [15] with an experiment which studied gaseous sonic and supersonic H_2 and N_2 injected into supersonic air at Mach 2.72 over a flat plate. Rakes were used downstream of the injection site to measure penetration and via species concentration profiles taken at various axial locations downstream of the injection site. Agreement with theory depended on the definition of penetration (e.g. where the species profile matched the theoretical data) as well as how the jet boundary based on the species profile was defined [12].

Similar studies were performed by Povinelli *et al.* [19] and Billig *et al.* [20] which showed that the species concentration profiles could be traced using a jet similarity relation given by Abramovich [21]. This relationship relates the non-dimensional jet height scaled with jet diameter (y/D) to the downstream distance of the jet (x/D) also normalized with jet diameter in the following relationship:

$$\frac{y}{d_j{}^*} = \left(\frac{q_j}{q}\right)^{0.434}\left(\frac{x}{d_j{}^*}\right)^{0.333} \quad (1\text{-}4)$$

were q represents the jet and crossflow dynamic pressure and $d_j{}^*$is the jet diameter for a sonic injector nozzle. The experimental data was found to correlate well with this expression in the near field of the jet ($x/D \leq 8$) but was highly over predicted the trajectory outside of this region.

To investigate potential improvements in jet far field trajectory prediction, as well as determining which factors most significantly control jet penetration, several studies [20], [19], [22] focused on varying injection Mach numbers, injection pressures and jet orifice geometry to guide their studies. Billig *et al.* [20] found that injecting supersonically did produce up to 15% deeper penetration than sonic injection, but this was limited to injection Mach numbers ($M_j \leq 5^{1/2}$). Also, absolute penetration was weakly effected by injector shape up to free stream Mach numbers of 4 [17]. Povinelli *et al.* [19] and later Papamoschou [22], Gruber [23] and Gamba [24] all showed that jet penetration, especially in the near field, strongly depends on the jet-to-freestream static pressure ratio (p_j/p_o) and the momentum flux ratio, (J), given in both traditional and compressibility dependence forms [23] [24]:

$$J = \frac{\rho_j {U_j}^2}{\rho_0 {U_0}^2} = \frac{\gamma_j p_j {M_j}^2}{\gamma_0 p_0 {M_0}^2} \quad (1\text{-}5)$$

Papamoschou suggested that a JISF has similar penetration characteristics as jets in subsonic crossflows and used a modification of the scaling law from Pratte and Baines [25] where the jet trajectory is scaled by both jet diameter and velocity ratio, r in the following manner:

$$\frac{y}{rd} = 2.63\left(\frac{x}{rd}\right)^{0.333} \quad (1\text{-}6)$$

Papamoschou noted that replacing r by $\sqrt{J}$ produced penetration results for a supersonic crossflow that were nearly identical to those in a subsonic crossflow [22]. Furthermore, it was noted that J has a much more significant effect on penetration, especially in comparison with the jet Mach number (M_j) and the density ratio (ρ_j/ρ_o), which was shown to have little noticeable effect [22].

Sau [26] and later Mahesh [27] noted that in compressible flows jet trajectory and penetration characteristics also depend on the boundary layer thickness to jet diameter ratio (δ/D), as well as jet and crossflow molecular weights (M_{wj} and M_{w0}) [26], [27]. Segal [3] proposed a generic jet-penetration scaling law that includes the effects of molecular weight differences and boundary layer thickness and has the following form:

$$\frac{y}{d_j} = A(J)^B \left(\frac{x}{d_j} + C\right)^E \left(\frac{\delta}{d_j}\right)^F \left(\frac{M_{wj}}{M_{w0}}\right)^G \tag{1-7}$$

where the constants have been suggested based on the crossflow Mach number (written as M_0) by Portz and Segal [25]:

$$\begin{aligned} A &= 1.05M_0 - 0.192 \\ B &= -0.0802M_0 + 0.615 \\ C &= -2.34/M_0 \\ E &= 0.406M_0^{(-0.823)} \\ F &= -0.067M_0 + 0.325 \\ G &= -0.0251 \end{aligned}$$

When relations A through G are used with Eq. (1-8), the scaling law suggested by Segal produced good agreement with experiment, especially in the midfield of the jet (see Ref. [24]).

1.3.3 Studies of JISF Turbulent Flow Structures and Mixing

In a scramjet engine, mixing must occur microscopically, that is on the molecular level at or near stoichiometric properties before combustion takes place [1]. The mixing can be divided into two parts: near field mixing which is related

to initiation of mixing via some stirring process similar to active stirring of coffee with dry powdered creamer, and far field mixing which describes the molecular diffusion of the mixants [1]. Mixing can be quantified in terms of 'scale of segregation' of the particles. Scale of segregation describes the separation distance between particles or how closely packed the molecules in the mixture are. In a microscale-mixture (or fully mixed mixture) the scale of segregation by definition is zero [1].

The aerothermodynamics of supersonic combustion dictate the coupling of turbulent mixing and chemical reactions. Generally before combustion occurs, the molecular mixing process must fully be sustained: there can be no fully efficient combustion without full mixing of constituent mixants. For a hypersonic vehicle designed for operation in the Mach 6-8 flight range, the burner entry Mach number generally is on the scale of Mach 2-3; this and practical size constraints limit the residence time of a propellant mixture to a time range on the order of 10^{-3} seconds. Thus all of the mixing must occur and the available energy extracted in this very small time window [3].

It is therefore important to understand the mechanisms which control and influence mixing, as well as develop a means of accelerating the mixing rates or increasing the residence time of the propellant mixture. Mixing effects are generally 3D turbulent flows which involve large velocity gradients, localized subsonic regions embedded within a largely supersonic flow, shock effects and various diffusive phenomena.

Several studies of compressible mixing layers including Papamoschou and Roshko [28] and Dimotakis [29] showed that the large scale vortical structures (LSV) present between streams develop localized mixing regions. The LSV structures develop to entrain initially unmixed fluid, creating a scenario which promotes mass and momentum transport as well as diffusion of the constituent elements. Papmaschou and Roshko also showed that in a compressible fluid, shear

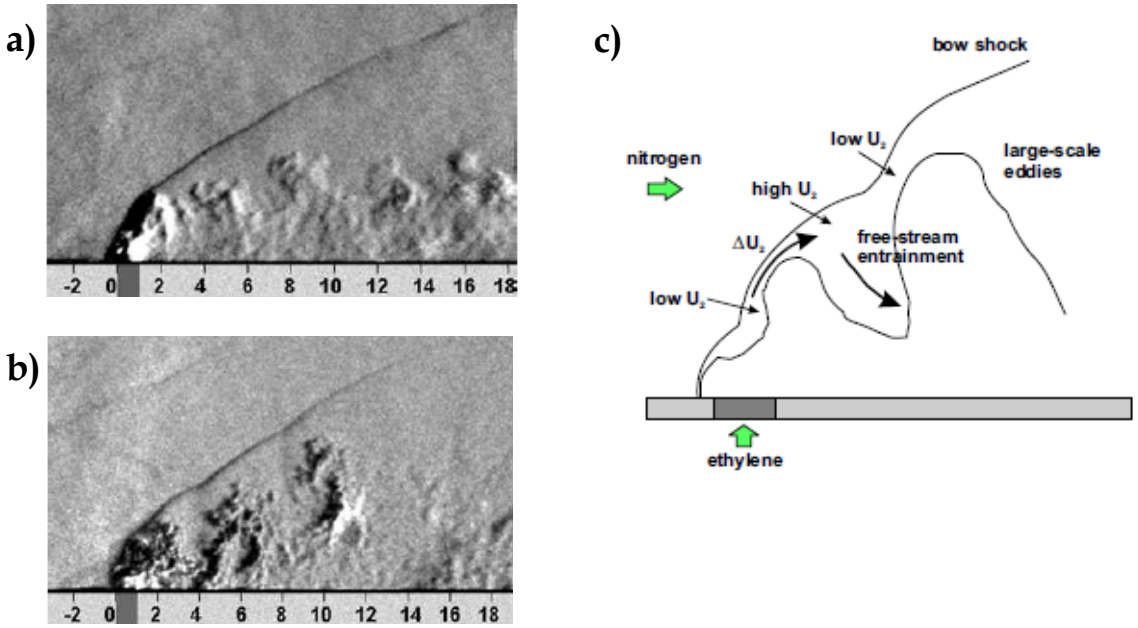


Figure 3: Images of coherent structures in JISF: Schlieren images of hydrogen injection (a) and ethylene injection (b) in a supersonic crossflow of nitrogen. A visual diagram of the high and low shear velocities which cause the formation of LSV structures (c). All images are reproduced from Ben-Yakar *et al.* [17].

thickening is promoted more significantly by velocity gradients than by density gradients.

Ben-Yakar *et al.* [17] showed that in addition to the classical description of JISF which suggests that jet penetration is dominated mostly by J and mixing by the CVP, other phenomena related to the development of LSV structures which develop especially in the immediate vicinity of the injector also influence mixing characteristics of a JISF. In Figure 3a-b, images (a) and (b) reveal that instantaneous schlieren images taken with exposures of approximately 2μsec showed different fluid structure characteristics between hydrogen and ethylene gaseous jets [17].

Each gas had similar behavior in the creation of LSV structures which were produced, stretched, tilted and torn as they moved in the downstream direction. Ben-Yakar *et al.* suggested that the "tilt-stretch-tear" phenomena was the result of velocity gradients between the flow downstream of the bow shock, and the jet

plume. Because of the significant difference in molecular weight between ethylene and hydrogen, the injection characteristics were different between the species. Since both ethylene and hydrogen were injected sonically, the speed of sound of ethylene was lower than hydrogen. As a result, ethylene exhibited larger velocity gradients across the jet-crossflow fluid interface downstream of the normal shock (Figure3c) and thus produced larger coherent jet fluid structures than hydrogen. Ethylene was able to penetrate deeper and dissipated quicker as a result of larger gradient and shear effects. Quicker dissipation of the LSV structures in ethylene was associated with higher mixing rates between ethylene and the free stream nitrogen flow [17].

1.3.4 Mixing Metrics

In addition to jet penetration, jet fuel mixing is an important aspect in understanding how efficiently the fuel delivery process occurs in a scramjet burner. Several metrics exist which describe the efficiency of mixing between the fuel jet and the free stream air. First, it important to quantify how well a given fuel-air ratio ($F = \dot{m}_J/\dot{m}_0$) compares with ideal conditions [1]. The fuel-air ratio is a measure of the ratio of the mass flow rate of the fuel ($\dot{m}_J$) to that of the free stream air ($\dot{m}_0$). Since the ideal fuel-air ratio is the upper limit for complete combustion of all oxidizer present is the stoichiometric fuel-air ratio, it is helpful to introduce the equivalence ratio (ER), that is the ratio of the fuel air ratio to that of the stoichiometric ratio [1]:

$$ER \equiv \frac{F}{F_{st}} \tag{1-8}$$

where for a hydrocarbon fuel of the form:

$$C_xH_y + \left(x + \frac{y}{4}\right)\left(O_2 + \frac{79}{21}N_2\right) \rightarrow xCO_2 + \frac{y}{2}H_2O + \frac{79}{21}\left(x + \frac{y}{4}\right)N_2 \tag{1-9}$$

from this expression, the stoichiometric fuel-air ratio can be expressed as

$$F_{st} = \frac{36x + 3y}{103(4x + y)} \tag{1-10}$$

This form includes the effects of atomic weights (H = 1, C = 12, N = 14 and O = 16) [1]. The variables x and y represent the number of atoms (e.g. for ethylene, C_2H_4, x = 2, y =4 and for hydrogen, H_2, x = 0, y = 2).

In the same way that jet penetration is a global measure of the promotion of fuel-air mixing, the jet mixture fraction distribution helps to specify regions where sufficient mixing occurs. Several different approaches have been suggested to quantify the jet mixture fraction. Liscinsky [30] introduced the "mixing parameter" MP, defined as:

$$MP = \frac{c_{var}}{c_{avg}\left(1 - c_{avg}\right)} \tag{1-11}$$

where the spatial concentration variance c_{var} is defined as:

$$c_{var} = \frac{1}{n}\sum_{i=1}^{n}\left(\overline{c_i} - c_{avg}\right)^2 \tag{1-12}$$

The other variables in Eq. (1-12) are the time-averaged concentration of species at any location ($\overline{c_i}$) and the average mass concentration of a specific species (c_{avg}), defined as:

$$c_{avg} = \frac{\dot{m}_j}{\dot{m}_j + \dot{m}_0} \tag{1-13}$$

The mixing parameter MP varies from 0 to 1, where $U = 0$ describes a fully mixed substance and $MP = 1$ describes complete segregation of the mixants. Eq. (1-11) is a normalized means of calculating how strongly or weakly the constituent substances have been mixed [3].

Kupchenov and Lombov [31] introduce the "mass fraction parameter" MFP, defined as:

$$MFP = \frac{\int_A \rho u (c - \bar{c})^2 dA}{\bar{c}^2 \int_A \rho u dA} \tag{1-14}$$

where $\bar{c}$ is the mass-averaged concentration, c is the concentration, ρ is the density and u the local velocity. The parameter MFP measures full uniformity when $MFP = 1$ and complete lack of injectant when $MFP = 0$ [3].

Several other pertinent formulations to describe fuel-air mixing, including the mixing efficiency parameter, discussed by Segal [3].

$$\eta_m = \frac{\dot{m}_{j,mixed}}{\dot{m}_{j,total}} = \frac{\int_A Y_r \rho u dA}{\int_A Y \rho u dA} \tag{1-15}$$

where $\dot{m}_{j,mixed}$ is the mixed fuel mass flow rate, $\dot{m}_{j,total}$ mass flow rate (mixed and un-mixed), and Y is the fuel mass fraction, and Y_r is the fuel mass fraction mixed in a proportion in which a combustion reaction can occur. A definition for Y_r is described by the following [3]:

$$Y_r = \begin{cases} Y, & Y \leq Y_{stoich} \\ \dfrac{Y(1 - Y)}{(1 - Y_{stoich})}, & Y > Y_{stoich} \end{cases} \tag{1-16}$$

were Y_{stoich} is the stoichiometric fuel mass fraction.

1.4 Mixing Performance Enhancement Studies

1.4.1 Passive Mixing Enhancements

There are significant advantages and draw backs from the two most easily implemented fuel injection strategies namely transverse injection (typically wall mounted) and axial injection [4]. Axial injection has benefits which include minimal momentum loss of the fuel jet (since all of the momentum follows the free stream), adding fuel jet momentum to the main flow, reduction in shock strength

(since the shock is oblique it is somewhat weaker), and as a result better total pressure loss performance [3].

The challenge with axial injection is associated with the physics of the mixing of parallel streams. The mixing zones between the air and fuel streams simply take a relatively long time for complete molecular mixing to occur, thus requiring long combustor lengths and thus adding to the system a substantial weight and thermal requirements [3]. Near field mixing could potentially be incomplete because of the distance required for the mixture to travel. Ultimately, penetration performance forces the jet to stay close to the wall and minimizes near field mixing; this limits the benefits of axial injection as a stand-alone fuel delivery mechanism.

Normal injection has the benefit of significant penetration and mixing especially in the near field ($x/D \leq 10$ in distance units scaled with jet diameter). An additional benefit for normal injection is the presence of the recirculation zones around the periphery of the injected fluid [17], [24]. These local mixing zones somewhat improve the residence time performance and could act as flame holding devices which stabilize combustion.

The draw backs of normal injection are still rather severe. At 90 degrees relative to the wall, the bow shock upstream of the injection region is at its strongest magnitude. Pressure losses can be severe enough to unstart the engine, which could lead to a catastrophic event during a high speed flight [1]. Also, since the jet has to turn toward the free stream, there is jet momentum loss associated with the jet turning mechanism.

In addition to detailed studies of at angled wall injection ($\theta_{inj} < 90^0$)(e.g. Maddelena *et al.* [32]), attempts have been made at enhancing mixing with both passive and active techniques. King *et al.* [33] studied a combination of both

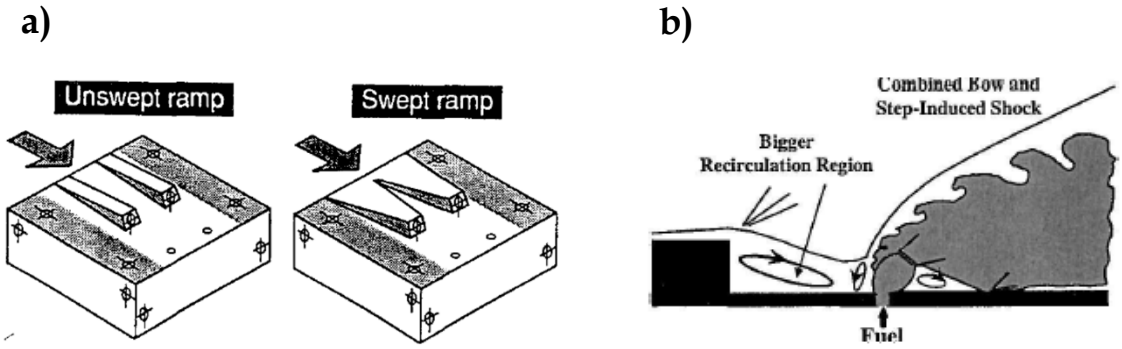


Figure 4: Diagrams of passive mixing enhancement approaches: (a) unswept and swept injector ramps, (b) rear facing step with injector. Images reproduced from Drummond et al. [34] and Ben-Yakar et al [7].

normal and tangential fuel injection with a wall embedded slot injector. It was shown that though spread was improved up to 70% above the tangential injector alone, the ability to find which combination of parameters could produce the set of large eddy structures necessary to enhance mixing was elusive [33].

Drummond *et al.* [34] modeled a pair of parallel injector ramps (with and without sweep) which showed an increase in stream-wise vorticity (Figure 4a). Drummond *et al.* suggested that the increase in stream-wise vorticity implied an improvement of jet-fluid mixing since larger recirculating fluid zones were shown to exist downstream of the parallel injectors. Even with the suggested mixing improvements, the mixing zones were still limited to the near wall combustor location [34]. Karagozian *et al.* [35] published the results of a flight experiment in which a normal injector was placed downstream of a rear-facing step (Figure 4b). A large recirculation zone is produced downstream of the step, which promotes subsonic mixing below a shear layer. Injection based in this region was shown to promote mixing and penetration but only in this zone. Little improvement was produced in the core flow regions [35].

Other improvements to normal injection have included studies of the effects of tandem normal jets [36], [37]. An early study by Cohen *et al.* [36] found that jet penetration was increased when an air jet was placed upstream of the fuel injector.

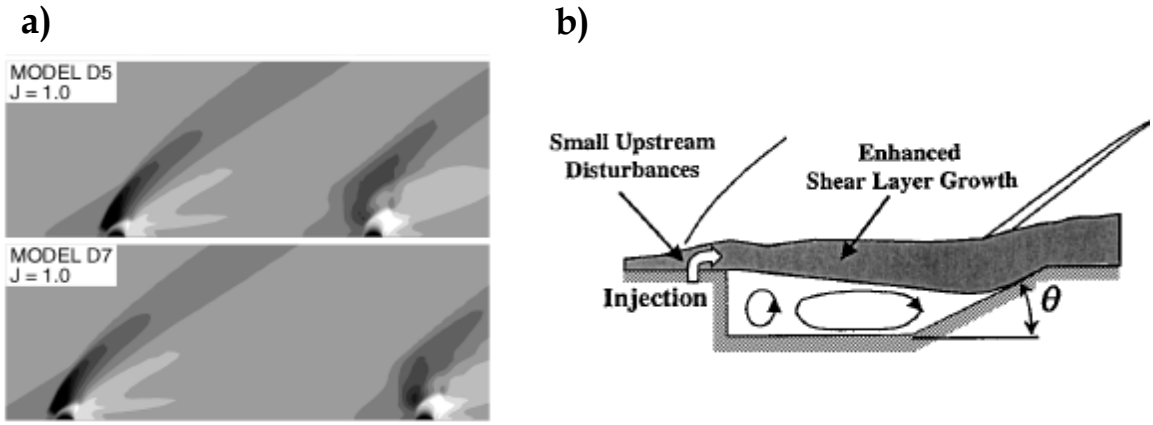


Figure 5: Mixing enhancement techniques: (a) Pressure contours from a CFD simulation of tandem injection with *J = 1* at various injector spacing lengths (D5 and D7), (b) injection with an acoustic cavity diagram. Reproduced from Lee *et al.* [37] and Ben-Yakar *et al.* [7].

This configuration promoted mixing especially in the near field. Lee [37] visited the problem later with a computational model, experimenting with two fuel jets placed at varying distances from each other (Figure 5a). Injector spacing was scaled with jet diameter (e.g. the D5 and D7 cases included injectors spaced 5 and 7 jet diameters from the origin of the simulation domain). The results demonstrated a slightly different flow field than with one injector; this included a secondary strong bow shock which added to the pressure losses even though mixing and penetration showed improvement from this configuration [37].

The cavity-flame holder concept (e.g. Ben-Yakar *et al.* [7], Ebrahimi [38]) has shown wide popularity in the design and experimentation of scramjet combustors. To improve the residence time, Ben-Yakar *et al.* [7] showed that a large cavity could act as a flame holder (when used in tandem with an injector) by a constant re-supply of oxidizer to the injectant. Using an angled rear wall adds the benefit of stabilizing the acoustic oscillations associated with traveling shocks between the cavity and the unsteady free stream flow while still promoting mixing from the thickened shear layer above the cavity. Subsequent numerical, experimental and even a limited number of flight experiments have validated the cavity-flame holder concept for supersonic combustion. Some configurations have even

included tandem injectors with a cavity as well as angled wall injectors placed systematically around the cavity [39], [40], [41].

1.4.2 Active Mixing Enhancements: Unsteady Jets

Active mixing enhancements include devices which are actively controlled to generate instabilities and improved mixing zones in a scramjet combustor [4], [6]. An extensive review of several approaches for active mixing enhancements including helmholz resonators, piezioelectric actuators and acoustic excitation can be found in Ref. [6]. Several early studies have investigated the effects of excitation on jets in incompressible flows [42], [43]. Since then there have been extensive numerical and experimental studies of the physical phenomena of excited jets (e.g. Refs. [44], [27], [45]). The subsequent sections provide a brief summary of research investigations which focused on excitation of jets in subsonic and supersonic crossflows.

1.4.2.1 Sub-Sonic Pulsed/Forced/Excited Studies

Literature describing excitation or forcing of jets in subsonic crossflows can be found as early as the 1970's. Crow and Champagne [45] investigated the effects of jet forcing on the flow structure of turbulent jets. It was suggested that under certain forcing conditions, the jet structure exhibited orderly patterns similar to the vortex shedding phenomena. They found that by applying periodic disturbances at a 'preferred mode', a dimensionless frequency (Strouhal number) of 0.30 that the spreading angle of the jet was maximized. The waves produced as a result of the disturbances had the widest amount of dispersion, and entrainment was also shown to increase. Furthermore, trains of large-scale vortex puff structures were found in the jet; these rings each carried their own momentum with no interaction from neighboring rings at a short distance from the jet exit area [45].

Viets [42] introduced a fluidic oscillator as an alternative to hyper-mixing designs to increase the velocity profile half width and mixing rates of jets. He found that oscillating the jet increased the jet spread rate and velocity profile half angle in comparison with the non-oscillating case. Viets defined the velocity half width as 'that point on the velocity profile where the local velocity is equal to the mean between the centerline value and the co-flowing stream value' [42]. An important historical note can be made on Viets' suggestion that the oscillating fuel injector could be used for fuel injectors in ramjet engines. This is one of the earliest suggestions for the use of pulsed fuel jets for high speed propulsion [42].

Narayanan *et al.* [43] studied oscillating jets which were excited with a flap structure located at the nozzle exit plane. Narayanan *et al.* found that antisymmetric oscillations in plane jets (when operating in the flapping mode) roll up and cause vortices, whose size depend on the amplitude of pulsation In this process, entrainment is significantly increased over the steady case due to enhanced mixing. There also was found a critical Strouhal number ($St = 0.22$) that was associated with amplification of the excited flow [43].

Vermeulen *et al.* [46] used a loud speaker to pulse an air jet in a wind tunnel crossflow. The results of this experiment showed pulsation produced strong changes in the mean velocity profiles, as was indicated by the large variance of ΔU_{rms} (especially in the near field of the jet) in the pulsed case when compared with the steady case. Also, jet spread and penetration were increased as well. Jet penetration was measured based on the furthest extent of the mean velocity profile as measured from the wall. Penetration was improved up to 92% at the location $x/D = 2.86$. Also, the jet mixing length was reduced as a result of pulsation. The strongest improvement (based on jet turbulence and penetration data) showed that the optimal penetration occurred when pulsing at Strouhal number ($St = 0.22$).

Since the early studies of excited jets, extensive experimental works have

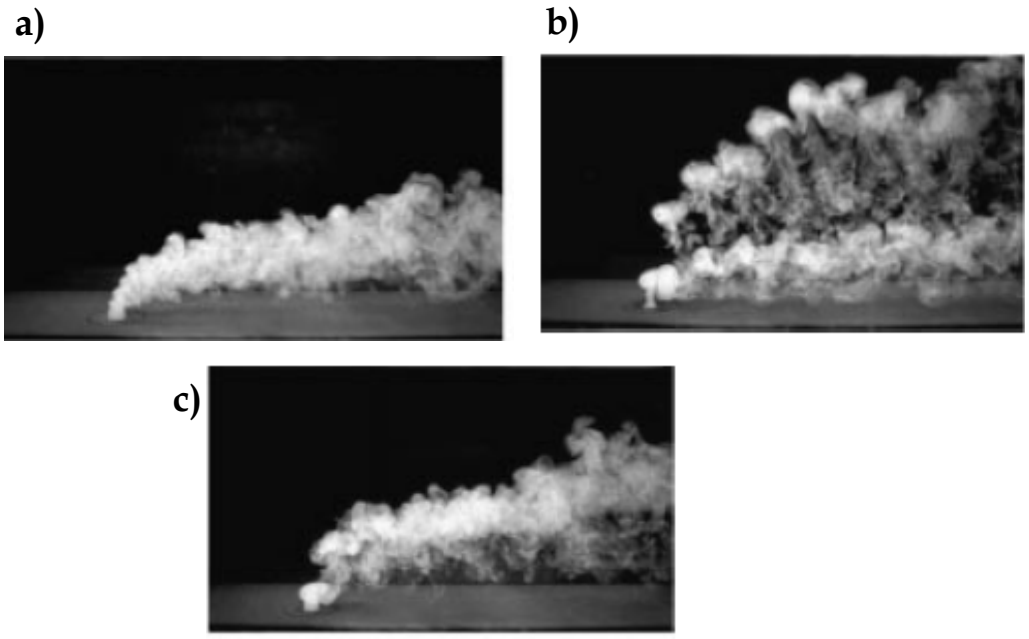


Figure 6: Comparison of "unforced" and "forced" jet in crossflow: (a) jet with no acoustic excitation, (b) jet excited with square waveform at f = 73.5 Hz and duty cycle of 22%, (c) jet excited with sinusoidal waveform at f = 73.5 Hz. Reproduced from [47].

focused on the physical mechanisms which govern the controlling parameters which optimize penetration and mixing. M'Closkey *et al.* [47] and Shapiro *et al.* [48] showed that optimal jet mixing and penetration conditions could be achieved depending primarily on pulsation frequency (f) and duty cycle (α). M'Closkey *et al.* showed for the same jet-to-crossflow velocity ratio ($r = 2.58$), acoustically forced jets improve mixing and penetration of jets in comparison to the baseline unforced case (Figure 6a-c).

Forcing conditions were shown to dictate jet structure and penetration characteristics. First, it was seen that sinusoidal pulsation improved jet penetration and jet spread, the significant impact in improvement favored square pulsation. Also, square excitation at frequency ($f = 73.5\,Hz$) and duty cycle ($\alpha = 22\%$) individual vortex rings formed in the jet after each pulse (Figure 6b). Each vortex rings penetrated deeper than the surrounding jet, producing turbulent streamers of entrained fluid around them. This behavior is only seen when pulsing in

optimal conditions. Other studies have demonstrated similar behavior when pulsing at optimal conditions [49]. However, the conditions for optimized control of jet penetration strongly depends on the pulsation device and flow conditions [50].

1.4.2.2 Pulsed/Forced/Excited Supersonic Crossflow Studies

To date there exists a small handful of published literature on pulsed jets in supersonic crossflows dating back to the early 1990's. Bogdanoff describes pulsing of jets using a Hartmann-Springer tube to create acoustic disturbances at high frequencies in a cavity [4]. Dziuba and Rossmann [51] later used a Powered Resonance Tube (a type of Hartmann-Springer Tube) to pulse an air jet into a supersonic crossflow. Pulsation fluctuations created by the injector were approximately 10% of the jet stagnation pressure. The results suggested that pulsation improved the mixing region downstream of the injector, but did little to significantly improve jet penetration or mixing.

A United States Patent was filed by the General Electric Company in 1992 by Epstein *et al.* [52] which described a fuel injection device designed to 'promote fuel and air mixing' in a scramjet engine. The injection system design included a rotary drive with a matrix array of rotating fuel injectors which to deliver fuel to the air-flow in sequential pulsed manner [52]. The pulsed injectors would periodically produce fuel slugs at each cycle which penetrate deeper and improve the mixing efficiency of the fuel by achieving 'more intimate contact' between the fuel and air. Control parameters would include the pulse frequency, pulse width (for a square pulse wave) and the equivalence ratio (ER). Epstein *et al.* suggested that when operating at stoichiometric conditions ($ER = 1$), a pulsed injector with a square pulse shape and a 50% duty cycle would inject a fuel slug at twice the injection pressure (p_j) and the equivalence ratio ($ER = 2$) during the 'on' phase

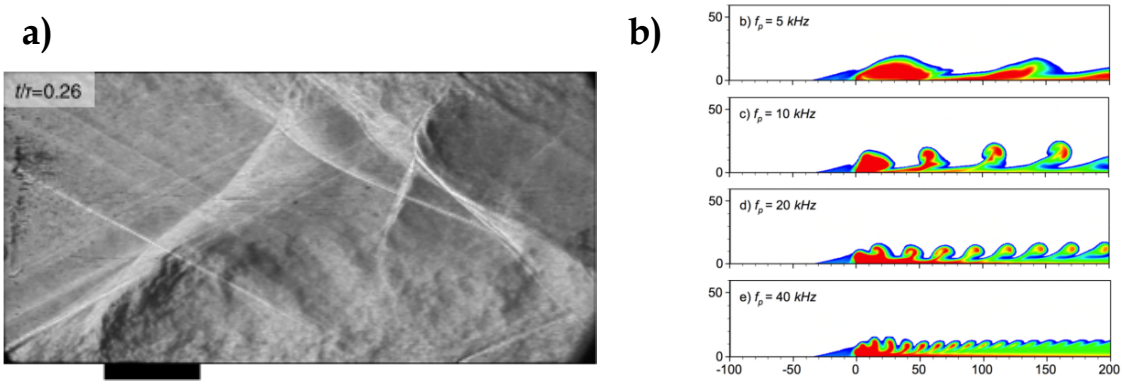


Figure 7: Pulsed injection in supersonic crossflows: (a) schlieren image of pulsed jet at cycle time 0.26T, (b) mass fraction contours of pulsed injection. Reproduced from Cutler *et al.* [53] and Kouchi *et al.* [54].

of the injection period to produce an equivalent amount of mass during a cycle as the steady injection. This would allow a direct comparison to be made between steady and pulsed injection.

Randolph, et al. [55] showed that low frequency pulses (1 Hz) of helium in a Mach 2.5 crossflow increased penetration up to an average of 12% deeper than a steady jet with the same momentum flux value. This study linked the increased penetration to a higher impulse due to temporal acceleration of the forced jet [55]. Vakili and Wu [56], [57] also observed increased penetration as a result of pulsed injection at lower frequencies.

Muruggapan *et al.* [58] and Cutler *et al.* [53] investigated pulsation in higher frequency ranges ($f \geq 10kHz$). Cutler *et al.* used a rotating wheel/plenum system to produce pulsed injection, and observed the effects of unsteadiness on penetration, mixing the bow shock structure (Figure 7a). Muruggapan *et al.* used a high frequency actuator (HFA) with an internal Hartmann-Springer Tube to excite a supersonic jet into a supersonic crossflow. Both studies showed improvement in penetration and mixing of the jet as a result of pulsation.

Recently, new investigations [59], [54] have presented experimental studies which involved frequencies of pulsation in the kHz range. Kouchi *et al.* [54] used both experimentation and 2D numerical to excite jets in crossflow for momentum

flux ratios between 1 and 5, and frequencies in the 0.2-50 kHz range. The results of this study concluded that there is an optimal frequency (between 10 – 20 kHz) which maximizes penetration of the pulsed jet. At higher frequencies the vortex structures which are formed interact with each other, reducing penetration effects and thus resulting in penetration similar to unforced jets (Figure 7b) [54].

1.4.2.3 Definitions and Classification of Unsteady Jet Injection

A generic topical study of unsteady fluid injection into crossflows across a wide variety of flow regimes and conditions will introduce the reader to terminology which includes 'pulsed injection', 'excited jets', 'forced jets', 'fully or partially modulated jets' and 'synthetic jets' [49], [46], [60]. An attempt is made here to classify the types of unsteady injection for clarification. Some of the aforementioned terms are synonymous and will be explained as such while other terms have specific meanings and implications.

First, the *modulation* of a jet refers to the periodic injection of a fluid from an orifice into either an ambient background, or one with crossflow. Jets can be modulated a certain percentage of a cycle; a 100% modulated jet refers to a condition where during some finite portion of an injection period, the jet has a definite 'off time' or a time during the cycle when fluid mass is not being injected from the orifice to a larger reservoir. This is often referred to as a 'fully modulated' jet. A 'partially modulated' jet in contrast refers to a periodic injection cycle where the amplitude during injection varies but is never zero or 'fully off'.

Injection cycles can be sinusoidal [60], square pulse shaped [50], pulsed via a continuous impulse function [55] or from various other wave forms [61]. The terms 'pulsed', 'excited' and 'forced' are often vaguely used in reference to the specific type of waveform which describes the cycle. The terms 'forced' or 'excited' jet generically implies a change in the amplitude of an injected quantity (e.g. jet pressure), whereas 'pulsed' is often used to denote a periodic, harmonic injection

scheme. For the purposes of this study, the term *pulsed injection* will be used to refer to a periodic, harmonic injection scheme in which the net mass flux during a full period is positive ($\dot{m}_{net} > 0$) [62].

A certain type of fuel injection can be contrasted with pulsed injection. Specifically, *synthetic jets* [63], [62] refer to unsteady injection of fluid from an orifice under the constraint of zero net mass flux over a full period ($\dot{m}_{net} = 0$). Lardeau *et al.* [63] describes the synthetic jet as a jet in which a forcing of the jet produces a train of vortex rings which are formed (as a result of forcing) periodically and are ejected through an orifice in such a way that the net mass flux is zero. The period includes a rise time during which mass in injected from an orifice, and a fall time where the mass is sucked back into the orifice in an amount equal to that of the rise time. Thus, the cycle averaged mass flow rate is zero [63].

1.4.2.4 Theoretical and Physical Description of Pulsed Injection

When a column of fluid is forced by a piston, which moves a distance (L) in an orifice of diameter (D) in a time duration (τ) a turbulent vortex structure of circulation strength (Γ) will be injected into the ambient field at the orifice exit area. The circulation strength and shape of the vortex structure will depend on the flow conditions during the pulse. Several studies [64], [65] focused on the pulse conditions which create 'optimized' vortex rings, in the absence of crossflows, using a piston/cylinder configuration. These studies found that the major control parameters to produce a vortex ring (a turbulent vortex structure in which Γ is strongest) included the time history of the piston velocity ($\overline{U}_P$), the stroke ratio (L/D), the jet's Reynolds number (Re_j), and the orifice/nozzle geometry. Gharib [66] likened the sequence of vortex rings leaving the orifice to the roll-up of a half-infinite cylindrical vortex sheet.

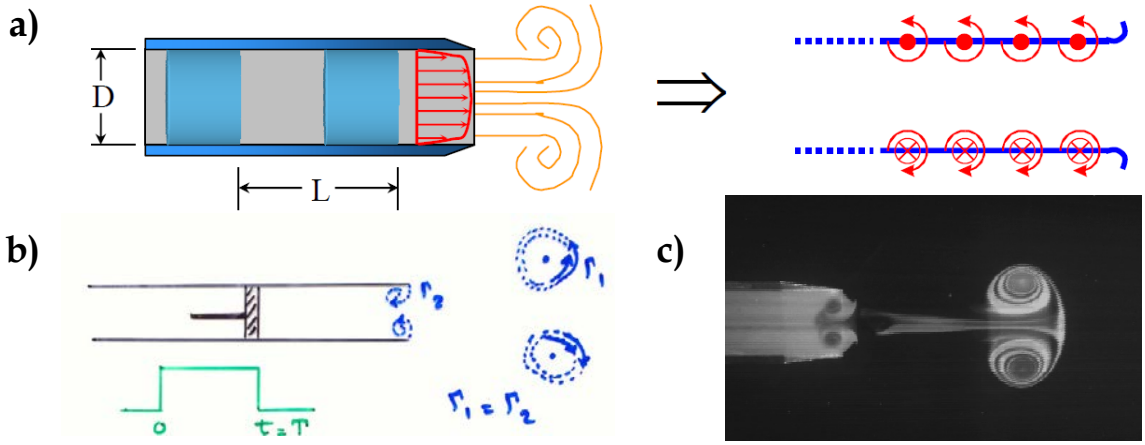


Figure 8: Visualization of formation of vortex ring: (a) piston diagram with half –'infinite' cylindrical vortex sheet roll up description, (b) vortex ring roll up and circulation conservation, (c) schlieren image of a vortex ring leaving an orifice. Reproduced from Gharib [66].

As can be seen in Figure 8a-b, the circulation produced at the wall due to the velocity gradient is balanced, that is Γ_1 (at the wall) is equal to Γ_2 in the vortex ring when the piston moves a distance L in a time τ in a full cycle of period T. Study of the optimization characteristics of vortex rings answer the question of the maximum vortex circulation strength Γ in an infinite pulse time τ.

From the results of several experiments [67], [68], it has been shown that the limit to the most optimal vortex ring can be related to a relationship for the stroke ratio; these studies have shown that vortex ring optimization occurs when L/D is around 4. The stroke ratio is defined as:

$$\frac{L}{D} = \frac{1}{DA}\left[\int_0^{\tau}\int_A^0 u(t)_j \, dAdt\right] \tag{1-17}$$

where $u(t)_j$ is the orifice or nozzle exit area averaged jet velocity. When the stroke ratio reaches a critical value ($L/D = 4$) it is commonly known as the *vortex formation number* or simply the *formation number* [66]. Gharib *et al.* [64] suggested that the energy supplied to a mass of fluid leaving an orifice from a source during a pulse stroke dictates the structural shape of the fluid.

A principle known as Kelvin-Benjamin Variation principle, states that when

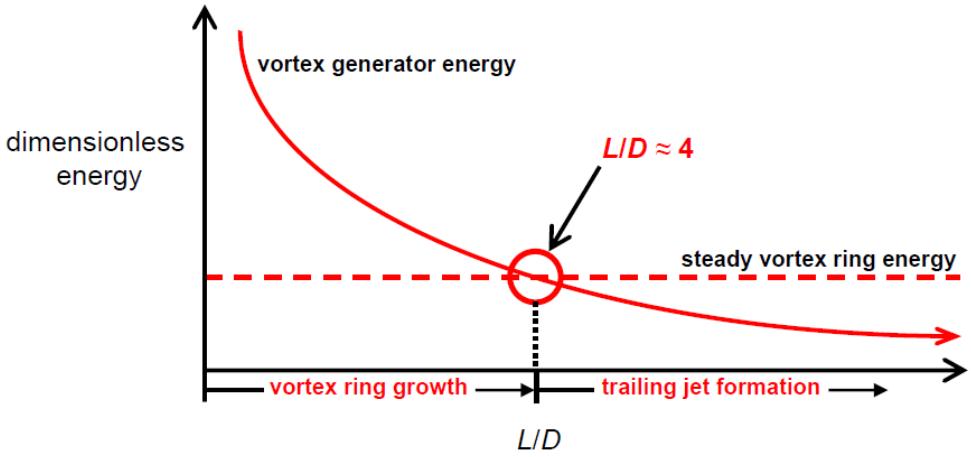


Figure 9: Diagram of stroke ratio (*L/D*) as a function of dimensionless energy. Reproduced from Gharib [66].

the energy supplied by a pulse source "….falls below that of a steadily translating vortex ring", a phenomena known as *vortex ring pinch off* occurs [66]. The stroke ratio L/D dictates whether the structure is a vortex ring, a vortex ring with trailing fluid, or an incoherent turbulent mass. For a vortex ring to form the energy supplied by the vortex generator (E_{VG}) must exceed the energy in the vortex ring itself (E_{VR}). A proportionality relationship between the non-dimensional energy of a fluid pulse (α_{ND}) and L/D is given by the following relationships:

$$\frac{E/\rho}{\sqrt{\left(I_P/\rho\right)\Gamma^3}} \equiv \alpha_{ND} \propto \frac{L}{D} \tag{1-18}$$

where I_P, the vortex ring total impulse is defined as:

$$I_P = I_P(\tau) \equiv \int_0^\tau \int_A \rho {u_j}^2(r,\tau)\, dA d\tau \tag{1-19}$$

or a measure of the average thrust during the pulse. The plot in Figure 9 shows a graphical relationship between dimensionless energy and the stroke ratio. It can be seen that the vortex generator energy decays as it crosses the steady vortex ring energy constant at the formation number.

It is evident that distinct regions of vortex formation occur, centered on the formation number. A weaker vortex ring forms when is ($L/D < 4$), a vortex ring forms with the maximum circulation at the formation number ($L/D \approx 4$), when, and either a vortex ring with trailing fluid or an irregular vortical structure (turbulent puff) when ($L/D >> 4$). The trailing fluid occurs when there is more energy delivered to a ring then there is needed for entrainment of the surrounding fluid. An excess amount of 'generated energy' leads to instabilities which fully compromise the structure of the vortex ring altogether.

Similar observations have been made in incompressible pulsed jets in the presence of a crossflow. Sau [65] used a Direct Numerical Simulation (DNS) model to explore the behavior of pulsed jet control on vortex structures in the presence of a crossflow. The DNS model showed good agreement with Gharib's experiments for pulsed jets with no crossflow, demonstrating the same formation characteristics and vortex ring behavior as in the experiments [69].

Using the same model but applied to cases with crossflows, several additional control parameters are important. To simulate piston motion in the injector, Sau [69] modeled a square waveform at the nozzle exit to specify the pulsed inflow conditions. Important variables include the pulse frequency, the mean jet velocity $\bar{U}_j$ (the exit velocity averaged over the nozzle exit area in time period T) and the nozzle exit diameter D. From this a non-dimensional frequency, yields the Strouhal number:

$$St = \frac{fD}{\bar{U}_j} \tag{1-20}$$

In the presence of a crossflow, the ring velocity ratio (r_{ring}) is also important. This is defined as:

$$r_{ring} = \frac{\Delta U_j}{U_\infty} \tag{1-21}$$

where ΔU_j is the peak-to-peak jet velocity, and U_∞ is the crossflow or free stream velocity. Sau related the stroke ratio (L/D) to the other parameters (for a square pulse wave) in the following manner. The stroke length for each cycle is related to other pulsing parameters by the following:

$$L = \Delta U_j \tau = \Delta U_j \alpha T \tag{1-22}$$

where α is the duty cycle, or the percentage of the cycle which the pulse is 'on', thus $\tau = \alpha T = \alpha f^{-1}$. Since for a fully modulated (100% modulation) pulsed jet, Sau defines the mean velocity $\overline{U_J}$ as:

$$\overline{U_J} = \left(\frac{1}{T}\right)\int_0^T u_j(t)dt = \Delta U_j \alpha \tag{1-23}$$

then it follows that the stroke ratio, duty cycle and Strouhal number can be related for fully and partially modulated jets respectively:

$$\frac{L}{D} = \frac{1}{St} \tag{1-24}$$

and

$$\frac{L}{D} = \frac{(\Delta U_j)\alpha}{\overline{U_J}} \times \left(\frac{1}{St}\right) \tag{1-25}$$

From these relations, it is shown that one can control vortex ring production properties consistently without regard to jet mean velocity or modulation properties. For instance, Sau showed that since the vortex ring parameters L/D and r_{ring} depend on the 'deviation of velocity about the mean velocity', one could observe the changes of stroke ratio and ring velocity depending on the choice of dependent variable [65].

Sau and Mahesh [69] showed that crossflow properties strongly influence the trajectory and structure of a pulsed jet. When the mean jet velocity ratio (r =

$\overline{U_J}/U_\infty$) is greater than 2 ($r > 2$) for stroke ratios of $L/D < 4$ the vortex ring tilts upstream towards the direction of the crossflow. However, for $L/D >> 4$, the vortex ring tilts downstream, away from the direction of the crossflow. When the mean jet velocity is $r < 2$ a distinct structural phenomena is present. Instead of the production of vortex rings, the pulsed jet produces structures known as 'hairpin' vortices. Hairpin vortices are produced when the upstream boundary layer cancels out part of the circulation near the upstream edge of the injector, which is necessary to produce the vorticity and roll-up phenomena which causes the full vortex ring to form. Instead of a full vortex ring, the hairpin shaped structures produce a combination of 'legs' and 'roller regions'. For $r < 2$ and $L/D >> 4$, a series of hairpin vortices are shed instead of one per pulse. This is due to the presence of an abundance of vortex generator energy during each stroke.

Also, instead of the presence of a counter rotating vortex pair (CVP) that is seen in steady jets, the hairpin vortices entrain fluid near the 'leg portion' of the structure, These follow the same rotational sense as the CVP found in flows of higher r. In both cases, ($r < 2$) and ($r > 2$) the rotational flow field carried with the vortex structure creates low pressure regions in the vortex core, producing strong mixing and entrainment regions.

These processes also induce a velocity and a momentum, associated with the Bio-Savart law which is a primary description of the increased penetration performance of pulsed jets. Several studies have suggested that the production of vortex rings induces a velocity (governed by the Bio-Savart law) which acts to increase the momentum of the individual vortex ring, allowing it to penetrate deeper into the cross flow [70], [71]. When distinct vortex rings are formed, penetration is optimal; when vortex rings are weaker and trail fluid or are diffuse in structure, penetration is significantly reduced.

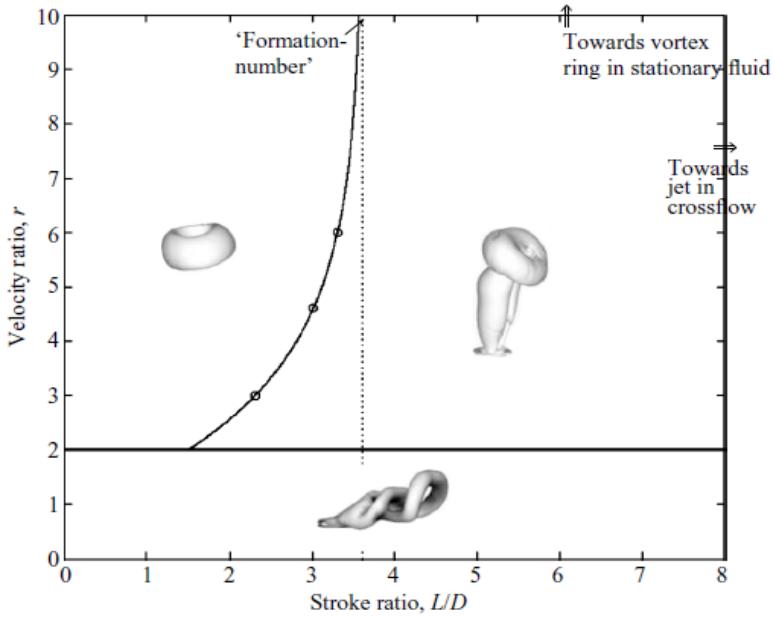


Figure 10: Pulsed jet regime map of distinct vortical structures as functions of velocity ratio, r and stroke ratio, L/D. Reproduced from Sau and Mahesh [70].

From the work of Sau and Mahesh, it can be seen in Figure 10 that three regimes of vortex structure exist for combinations of stroke ratio and velocity ratio: distinct vortex rings (for $L/D \leq 4$ and $r > 2$), vortex rings or puffs with trailing fluid (for $L/D >> 4$ and $r > 2$) and 'hairpin vortices' for all L/D values for which $r < 2$ [65]. Other studies have focused on how the momentum flux ratio, duty cycle and pulse shape affect the penetration of incompressible pulsed jets in cross flows. It has been shown that smaller duty cycles with square waves penetrate deeper than sinusoidal or saw-tooth waves at the same duty cycle or at larger duty cycles [48].

1.4.2.5 Pulsed Injection Trajectory and Mixing Studies

Several authors have produced modifications to the scaling laws which account for the effects of pulsation [49], [50], [72]. Eroglu *et al.* used Pratte and Baines' trajectory law for steady injection [25] (scaled with the product of mean jet velocity and jet diameter(rD)) but modified it for the effects of pulsation for an

improved jet velocity ratio r based on a mean jet velocity integrated over a pulse cycle [49]. Eroglu *et al.* suggested that to compare the penetration of a pulsed jet to steady jet, a pulse-specific velocity ratio (r') should be used. This expression is given for incompressible flows by:

$$r' = \left(\frac{J_A}{\rho {U_\infty}^2 A_j}\right)^{1/2} = 1.41r \tag{1-26}$$

where

$$J_A = \frac{1}{T}\int_0^T \rho\, {u_j}^2(t) A_j dt \tag{1-27}$$

describes the jet momentum. The following expression includes the effect of pulsation via the pulse-specific velocity ratio (where the jet velocity only accounts for the magnitude of a square pulse during the 'on' portion of the cycle.

$$\frac{y}{r'd} = 2.63\left(\frac{x}{r'd}\right)^{0.28} \tag{1-28}$$

It was suggested that even with the above expression, other mechanisms such as vortex ring spacing and interaction play a significant role in the increased penetration of a pulsed jet.

Eq. (1-28) does not include a direct means of measuring jet penetration based on pulsation frequency or stroke ratio. Johari [50] introduced pulsed jet scaling law based on Glezer and Coles' [73] study of the motion of vortex rings and turbulent 'puff' structures. If it is assumed that the trajectory of pulsed jets consists of non-interacting vortex rings or puffs in which no bending or tilting occurs, the trajectory can be described by the following expression:

$$y = \mathrm{k}\left(\frac{Ix}{\rho U_\infty}\right)^{1/4} \tag{1-29}$$

where the nozzle jet impulse, I is:

$$I = \int_0^\tau \int_A \rho {u_j}^2(t)\, dA dt = \rho {\overline{U}_j}^2 \frac{\pi}{4} d^2 \tau P \tag{1-30}$$

and P is a parameter which accounts for the non-uniform jet inflow velocity profile during a pulse stroke. The parameter $P = 1$ for a square pulse, and varies from 1.05 – 1.5 for other jet profile time histories.

Accounting for these expressions and substitution into this expression leads to a form of the trajectory in terms of the stroke ratio and *average jet velocity during the 'on time' of the pulse* $r_p = \bar{U}_j / U_\infty$:

$$\frac{y}{d} = \mathrm{k}\left(r_P \frac{L}{d}\right)^{1/4} \left(\frac{x}{d}\right)^{1/4} \tag{1-31}$$

where k represents a proportionality constant, which is valued as high as 13 for vortex rings and as low as and 3 for turbulent puffs. Eq. (1-31) is true pulsed injection in an incompressible flow. Pasmurti *et al.* [72] modified Eq. (1-31) to account for compressibility effects. Since in a compressible flow, the momentum flux ratio is proportional to an effective velocity ratio:

$$r_{\mathrm{eff}} = \sqrt{J} = \sqrt{\frac{\rho_j {U_j}^2}{\rho_0 {U_0}^2}} \tag{1-32}$$

substitution into Eq. (1-31) leads to the compressible form:

$$\frac{y}{d} = \mathrm{k}\left(\sqrt{\frac{\rho_j {U_j}^2}{\rho_0 {U_0}^2}} \frac{L}{d}\right)^{1/4} \left(\frac{x}{d}\right)^{1/4} \tag{1-33}$$

Johari introduced a scaling law for evaluating the passive scalar mixing of a pulsed jet in crossflow using the decay of mass concentration [50]. For full vortex rings (or turbulent vortex puffs) mixing occurs towards the edge of the vortical structure while the core remains relatively unmixed. Johari suggested that the volume of a vortex puff (V_p) scales with the cube of the vortex puff diameter (δ_p),

which can be expressed as $V_p \sim {\delta_p}^3$. It has been suggested that puff diameter (δ_p) is related on the puff penetration height (y), in the following expression [50]:

$$\delta_p \approx 0.24(y) \tag{1-34}$$

Thus, a vortex puff volume can be expressed as:

$$V = \left[\left(r_P \frac{L}{d}\right)^{1/4} \left(\frac{x}{d}\right)^{1/4}\right]^3 \tag{1-35}$$

Johari further suggested that within a turbulent puff, the mean concentration decay C is proportional to the volume of mass injected during each pulse. Thus, the following expression represents the mean mass concentration of a pulsed jet in crossflow (where each pulse consists of evenly spaced turbulent puffs)

$$C(x) \sim {r_P}^{-1/3} \left(\frac{L}{d}\right)^{1/4} \left(\frac{x}{d}\right)^{-1/4} \tag{1-36}$$

Pasmurti *et al.* used this expression to measure mixing of pulsed jets in compressible, subsonic crossflows replacing r_P with Eq. (1-32) and found reasonable agreement between Eq. (1-36) and their LES results (see Ref. [72]). These results suggest that Eq. (1-36) can be used to estimate mixing of a pulsed jet in a compressible crossflow via measurment of the mean concetration decay, assuming the turbulent puff structures are evenly spaced after each pulse cycle.

1.4.2.6 Injection Approach to Forced Jets

Several approaches to pulsed injection have been discussed in literature, depending on the point of emphasis. Several authors have shown that the choice of pulse waveform influences the optimization of penetration. Shapiro *et al.* showed that a fully modulated square pulse waveform increased penetration over a sinusoidal one [48]. Several sources have shown that sinusoidal wave forms still improve the penetration characteristics of pulsed jets. Binder *et al.* numerically

investigated the experiment performed by Vermeleun *et al.* [46] study which employed a shifted sinusoidal pulsed jet wave [60]. The expression of the pulsed wave form from Binder *et al.* can be written in general for a given flow jet flow property φ in the following form:

$$\varphi_j(t) = \varphi_j + \varphi_j \sin(2\pi f t) \tag{1-37}$$

This form is important if one is interested in delivering the same cycle averaged value of a given flow property $\varphi_j(t)$ to compare with an unforced equivalent flow property. For direct comparison between a continuous flow property φ_j and the instantaneous periodic property $\varphi_j(t)$ one must introduce a cycle averaged value, $\varphi_{j_{cycle}}$, where the cycle averaged flow property (injected from a nozzle) is defined as:

$$\varphi_{j_{cycle}} = \frac{1}{TA_j}\int_0^T \int_{A_j} \varphi_j(A_j, t)\, dA_j dt \tag{1-38}$$

where A_j represents the nozzle orifice exit area. It is also helpful to define 'peak valued' variables to study the effects of 'unsteadiness' in comparison to those of continuous distribution. For example, Randolph *et al.* studied low frequency pulsed injection (1 Hz) in a supersonic crossflow but pulsed the jet at an injection pressure which peaked at the continuous pressure value [55]. Thus for the injection generic flow property $\varphi_j(t)$, the maximum value attained during the cycle is represented as φ_{j_p}. The cycle averaged value of $\varphi_j(t)$ when comparing peak pulsed values to the continuous equivalent will be less in proportion to the difference between φ_{j_p} and $\varphi_j(t)$.

1.5 Problem Description and Primary Motivation

In light of the improvements which have been made to enhance the mixing and penetration of fuel into supersonic combustors, certain challenges still remain

which have yet to be investigated and implemented in a design. Though mixing enhancements including angled wall injectors and cavities have been shown to improve jet penetration and mixing in supersonic crossflows (e.g. [32], [7], [38]) it is of interest to further investigate additional performance enhancements.

Many of the techniques which improve penetration do so at the cost of far field mixing (most normal injection modes) as well as substantial losses in total pressure and wall pressures. Techniques which improve mixing (especially axial and wall mounted angled injection, cavity-flame holders) do so at the detriment to penetration. It is desirable to develop a 3D model which resolves salient flow features produced by pulsating jets into the crossflow in addition to demonstrating the feasibility of applying this technique to fuel delivery in high speed engines.

The motivations for this research investigation are to investigate a means of improvement of fuel injection into a scramjet engine. The hypothesis presented at present (based on the works of Bogdanoff [4], Epstein et al. [52], Seiner et al. [6] and Kouchi et al. [59], [54]) is that *pulsation of the fuel jet in the appropriate range of frequencies produces increased jet penetration and axial mass concentration decay associated with increased fuel-air mixing rates at the same time averaged jet injection pressure in comparison to steady injection*. It is also hypothesized that the time averaged jet total pressure losses are less severe in pulsed injection in comparison to steady injection.

1.6 Primary Investigations

1.6.1 Thesis Statement and General Description of Study

As far as is known, there are only a handful of experiments and even fewer numerical models of pulsed gaseous jets injected into supersonic crossflows. The experimental studies focus on some penetration characteristics with limited description of mixing; there is little focus on the ability to control penetration via

observation of wave form, species, or frequency characteristics of the jets [58], [56], [54]. The 2D unsteady Reynolds Averaged Navier-Stokes (URANS) models of PJISF from Kouchi *et al.* [54] are admittedly limited in their ability to fully resolve turbulent flow structures related to jet penetration and mixing in the kilohertz pulsation range.

Generic, qualitative penetration data does exist from previous similar studies, validated by a few experiments [59]. ***Therefore, the primary objective of this study is to observe the qualitative and quantitative behavior and flow characteristics of a kilohertz range pulsed gaseous jet injection of hydrogen into a supersonic crossflow as recorded in a 3D large eddy simulation (LES) model.*** Furthermore, it is planned to demonstrate the hypothesized increased penetration, and mixing characteristics of pulsed injection qualitatively and quantitatively, thus matching the overall behavior discussed in the extensive subsonic literature as well as characteristics produced in the limited supersonic studies.

Phenomena associated with high frequency pulsed injection have been observed in the current body of work associated with 3D shock/mixing/fluid structure interactions. These phenomena ***which have never been discussed in other PJISF*** studies are presented in this study. The subsequent sections further discuss the approach taken to further the state of knowledge of pulsed gaseous injection into supersonic crossflows in the absence of heating and combustion characteristics.

1.6.2 Proposed Research Objectives and Focus

The primary objective of this study is to investigate numerically in 3D space the hypothesis that a pulsed sonic gaseous jet when excited at the appropriate frequency, pulse width and peak pressure can improve the fuel jet penetration and mixing performance, while reducing total pressure loss characteristics when compared with a continuous JISF. The study will focus on the behavior of cold

flow injection (no combustion effects will be considered). Currently, only single injector systems will be considered for investigation (i.e. effects of multiple injectors will not be considered).

To both directly observe the instantaneous inertial effects of pulsation and also to isolate the effects of unsteadiness, pulsation conditions will include injection at cycle averaged mass flow rates (matched with the instantaneous mass flow rate of continuous injection) and pulsed conditions which match only the cycle averaged pulsed injection pressure to the steady injection pressure. Several research questions have been raised [52], [55], [54] which have yet to be answered when considering PJISF approaches. Specific answers to these questions and several others are attempted here.

Furthermore, the study will attempt to answer the following specific research questions:

- Does pulsation of the jet improve the jet penetration and mixing characteristics of a PJISF over a continuous JISF?
- Does the unsteady bow shock as a result of pulsation improve performance total pressure recovery inside the pulsed jet?
- Does the high frequency unsteadiness allow for improved jet penetration prior to the development of a strong Mach disk?
- What are the effects of shock waves on pulsed injection? Are the fluid structure effects reported by Ben-Yakar *et al.* [17] (for steady injection) and Sau and Mahesh [69] observed in PJISF?

1.6.3 Research Approach and Specific Contributions

The numerical approach presented in this study is a wall-modeled Large Eddy Simulation (WMLES) which resolves the large scale turbulent structures present in the flow. Numerical approaches (Computational Fluid Dynamics) and some limited analytical descriptions will be used in this study in the absence of an

experimental apparatus. The machining of the UTSI Mach 2.3 Wind Tunnel and pulsation mechanism (both designed partially by the author) were unable to be completed in time for this study (as was planned in the dissertation proposal). Therefore, significant demonstration of the validation and verification of the numerical models is imperative. The approach taken to accomplish this is as follows. First 2D models were developed to produce a quick estimation of the performance of pulsed injection over a wide range of frequencies. These studies included investigations on various grid densities to isolate the effects of grid generation on the results. The 2D models results were qualitatively compared to results established in literature.

To investigate the 3D structures of PJISF, 3D models were produced to further investigate pulsed jet behavior. To validate and verify the 3D results, grid independence and model independence studies were done. Specifically, for grid independence two structured grids (10M and 17.8M cell grids) were constructed. A steady injection baseline case included both grid sizes to observe the ability of the grids to resolve important flow features (e.g. vortical structures associated with mixing and shocks). The results from the 17.8M cell steady injection case were compared with 1D compressible flow theory calculations to see how close the model predicts the appropriate flow properties (e.g. temperature, pressure and velocity).

These frequencies ranges chosen in this study (8 – 48 kHz) in the 2D model and 16 kHz for the 3D model are based on the results of Kouchi *et al.* which suggested *that peak jet penetration performance of high frequency sinusoidal pulsed injection occurred in the frequency range of 10 to 20 kHz*. The 2D and 3D simulations were done in the Computational Engineering and Research Group (CEAR) at UTSI. Qualitative visual data (including time averaged and instantaneous data) was collected from the numerical solutions to understand both the time-evolution of fluid structures during pulsation and also the mechanisms which cause

increased penetration. Quantitative data was collected (e.g. mass concentration profiles) to measure the penetration trajectories and mass concentration decay rates of the pulsed and steady injection approaches. The compressible pulsed jet trajectory from Pasmurti *et al.* was used to compare the results of the current pulsation penetration against an established scaling law in terms of stroke ratio and cycle averaged momentum flux ratio. Thus it was expected that the CFD models can be validated with analytical expressions a priori to experiment which should follow in subsequent studies.

Specific research contributions to the generic study both of scramjet fuel injection approaches, and to the specific JISF phenomena include:

- A wall-modeled Large Eddy Simulation (LES) model of a PJISF which resolves large scale eddy structures (for pulsation schemes of cycle averaged mass flow rates).
- Demonstration of improvement (total pressure loss, mixing and penetration) of pulsed injection in a supersonic crossflow compared to steady injection
- Demonstration and description of the time-evolution of vortical structures associated with PJISF as they related to improved fuel delivery performance
- A comparison of pulsed jet data with the empirical penetration trajectory and mass concentration decay based on the works of Pasmurti *et al.*, which describe both near and far field jet penetration and mixing up to ($x/D \leq 30$)
- Comparison of pulsed jet structure with the pulsed jet structures mentioned in the pulse jet regime map from Sau and Mahesh for $r < 2$ and $L/D >> 4$.

2 Theoretical Foundations and Numerical Methodology

2.1 General Equations

2.1.1 Instantaneous Conservation Laws

The following relations (instantaneous, fully viscous, compressible Navier-Stokes equations) can be used to fully describe the flow field of a compressible, non-reacting, single phase gas mixture without external body forces or external heating (written in the notation of Ref. [74]):

$$\frac{\partial \rho}{\partial t} + \nabla \cdot (\rho \mathbf{u}) = 0 \tag{2-1}$$

$$\frac{\partial \rho \mathbf{u}}{\partial t} + \nabla \cdot \left(\rho \mathbf{u}\mathbf{u} + p\bar{\boldsymbol{\delta}} - \bar{\boldsymbol{\tau}}\right) = 0 \tag{2-2}$$

$$\frac{\partial E}{\partial t} + \nabla \cdot \left[E\mathbf{u} + \left(p\bar{\boldsymbol{\delta}} - \bar{\boldsymbol{\tau}}\right) \cdot \mathbf{u} - \kappa \nabla T\right] = 0 \tag{2-3}$$

$$\frac{\partial \rho Y_\kappa}{\partial t} + \nabla \cdot (\rho \mathbf{u} Y_\kappa) - \nabla(\rho D_\kappa \nabla Y_\kappa) = 0 \tag{2-4}$$

where ρ is the fluid mixture density, $\mathbf{u}$ represents the velocity vector, p the local pressure, $\bar{\boldsymbol{\delta}}$ represents a unit tensor, $\bar{\boldsymbol{\tau}}$ shear stress tensor, E the total energy, κ the thermal conductivity coefficient, T the local temperature, Y_κ species mass fraction and D_κ is the species diffusion coefficient.

The definition of the shear stress tensor in a Newtonian fluid, $\bar{\boldsymbol{\tau}}$ is defined by the following expression:

$$\bar{\boldsymbol{\tau}} = \mu(2\bar{\boldsymbol{S}}) + (\lambda - \frac{2}{3}\mu)(\nabla \cdot \boldsymbol{u})\bar{\boldsymbol{\delta}} = 0 \tag{2-5}$$

Here, μ and λ represents the bulk molecular dynamic viscosity and bulk viscosity of the mixture, and $\bar{\boldsymbol{S}}$ is the strain rate tensor, defined as:

$$\bar{\boldsymbol{S}} = \frac{1}{2}(\nabla \boldsymbol{u} + (\nabla \boldsymbol{u})^{\boldsymbol{T}}) = 0 \tag{2-6}$$

2.1.2 Equations of State

To describe a perfect gas mixture, the following expressions are used [74]:

$$p = \frac{\rho R T}{\mathrm{M}_w} \tag{2-7}$$

$$E = \frac{p}{\gamma - 1} + \frac{1}{2}\rho \boldsymbol{u} \cdot \boldsymbol{u} \tag{2-8}$$

where R is the ideal gas constant, and both $\mathrm{M_w}$ and γ represent the mixture molecular weight and specific heat ratio respectively.

2.1.3 Physical Description of Turbulence

The instantaneous flow field present in supersonic jet/crossflow interactions is highly unsteady and includes fluctuations of fluid properties associated with mixing and vortex roll up. Since the current study uses turbulence models to describe pulsed injection (Reynolds' Averaged Navier-Stokes (RANS) and Large Eddy Simulations (LES)), a background and physical description of turbulence is appropriate here. *Turbulence modeling* attempts to quantitatively describe the characteristics of fluid behavior in which certain physical phenomena are present, including random perturbations of fluid properties (e.g. velocity or pressure), local regions of vortex roll up (or eddies), as well as the mechanism which describe how kinetic energy is transmitted or diffused from larger to smaller scales of motion.

Gibson [75] states that turbulence "occurs when the vortex forces per unit mass $\boldsymbol{u} \times \boldsymbol{\zeta}$ exceed the viscous forces $\nabla \cdot (\boldsymbol{\tau}/\rho)$ per unit mass". In other words, the instabilities present in the flow become significant enough to impede the ability of viscous effects to dampen them. The ratio of inertial forces to viscous forces is characterized by the Reynolds Number [75]:

$$Re = \frac{\rho U D}{\mu} \tag{2-9}$$

where U is the characteristic velocity and D is the length scale of a jet, scaled with jet orifice diameter. In stationary jets and jets in crossflows turbulence first appears near the jet orifice exit, several jet diameters downstream of the orifice exit plane. Viscous eddies form at shear layer interface regions (regions where velocity gradients are present). These eddies form vortex sheets which grow thicker as they travel downstream of the orifice [76]. The shear layer grows by viscous diffusion, until the Reynolds number reaches a critical value, after which the jet is fully turbulent. This value, known as the *critical Reynolds number* (Re_δ) is on the order of the shear layer thickness (δ_s) where ($\delta_s \propto D$). Typically, free jets are fully turbulent when $Re \geq 10^4$ [77].

Eddy size is proportional to the Kolmogorov length (L_κ), time (T_κ) and velocity (V_κ) scales and can be estimated by the following relationships [75]:

$$L_\kappa = \left(\frac{\nu^3}{\varepsilon}\right)^{\frac{1}{4}} \tag{2-10}$$

$$T_\kappa = \left(\frac{\nu}{\varepsilon}\right)^{\frac{1}{2}} \tag{2-11}$$

$$V_\kappa = (\nu\varepsilon)^{\frac{1}{4}} \tag{2-12}$$

where ε is the eddy viscosity dissipation rate of the shear layer, ν is the kinematic viscosity, and the κ subscript denotes a Kolmogorov scale property.

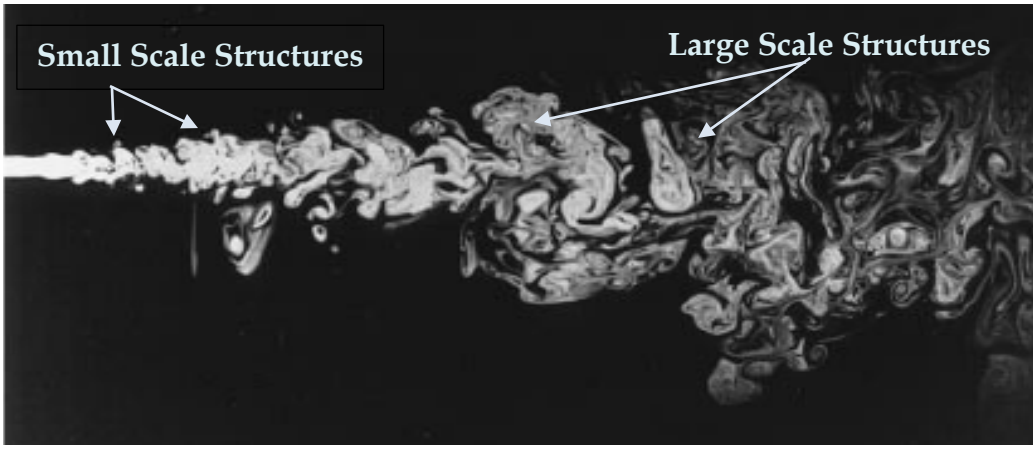


Figure 11: Large and small scale structures in a round turbulent jet. Reproduced from Dimotakis [77].

Turbulent behavior can be described as possessing an energy cascade process in which turbulent kinetic energy is passed from large scales to small scales [76]. Dissipation occurs when the turbulent kinetic energy passing to the smaller scales is converted into thermal energy through molecular viscosity. The tendency of the smallest eddies is that at this scale the energy is fully converted to heat via viscous dissipation. The small scale eddy motion occurs in a really short time, thus the motion of the small scale eddies can be thought of as being entirely independent of the large scale motion, and of the mean flow (Figure 11). Hence the smallest scale eddies receive energy from the large scales at the same rate at which they dissipate kinetic energy [76].

This was essentially the hypothesis of Kolmogorov [78] that at the smallest scales motion is only related to the rate at which energy is supplied by larger eddies (quantified by the dissipation, ε) and the kinematic viscosity of the fluid, ν. Eq. (2-10), (2-11) and (2-12) describe relationships between the eddy dissipation and kinematic viscosity for the Kolmogorov length, time and velocity scales. Another scale which is useful for relating energy absorption and dissipation is known as the Taylor micro-scale. The Taylor micro-scale is the scale at which turbulent mixing is said to occur. The following equation is an expression which

relates the Taylor micro-scale to the energy dissipation, turbulent kinetic energy and kinematic viscosity: [79]

$$\lambda_t \sim \sqrt{10\nu \frac{k}{\varepsilon}} \tag{2-13}$$

The Taylor micro-scale describes the region where viscous effects become significant in the mixing process, and is located somewhere between the largest and smallest 'sizes' in the Kolmogorov scale. Thus, for high Reynold's number flows the following expression is true:

$$\eta \ll \lambda_t \ll L_{\text{к}} \tag{2-14}$$

where η represents the smallest length scale of turbulence. Furthermore, the Kolmogorov length and time scales and the Taylor length scale can be related to the Reynolds number (making it simpler to estimate them) by the following relations:

$$\frac{L}{\eta} = Re^{\frac{3}{4}} \tag{2-15}$$

$$\frac{T}{t} = Re^{\frac{1}{2}} \tag{2-16}$$

$$\frac{\lambda_t}{\eta} = D\sqrt{10}Re^{\frac{1}{4}} \tag{2-17}$$

The process of energy transmission and dissipation across the turbulence scales can be thought of as an energy spectrum. The cascade of turbulent energy has a direction, increasing in magnitude inversely in proportion to the size scale. The energy spectrum $E(\omega)$ can be described by the following relationship:

$$E(\omega) \propto \omega^{-\frac{5}{3}} \tag{2-18}$$

where ω represents the wave number of fluctuating turbulence. Thus the kinetic energy is hand also independent and is handed down from large eddies to

progressively smaller and smaller eddies in what is known as the energy cascade. The fluctuating properties contain energy across a wide range of frequencies, with the higher frequencies being the most energetic eddies. Large eddies have behavior that is anisotropic and independent of viscosity, but strongly dependent on the large velocity and length scales [76].

Small eddies depend only on the rate of dissipation of turbulent energy and the kinematic viscosity of the particular fluid. The spectral energy only depends on the problem through the rate of energy dissipation and is not linked to other flow properties. The diffusive action of shear tents to smear out directionality at smallest scales. At high mean flow Reynold's numbers the smallest eddies in a turbulent flow are isotropic or non-directional [76].

2.2 Theory of Turbulence Modeling

2.2.1 Mathematical Description of Turbulent Flows

In Sec. 2.1.3, turbulence was described as a flow characteristic which comprises of random fluctuations of flow properties. Mathematically, at any instant in time flow properties experiencing turbulent effects can be thought of as having a mean or time independent component and a fluctuating component. For a general flow property $\varphi(t)$, the mean and fluctuating components can be expressed as the sum of the mean component Φ and the fluctuating component $\varphi'(t)$:

$$\varphi(t) = \Phi + \varphi'(t) \tag{2-19}$$

where the mean component Φ is defined as:

$$\Phi = \frac{1}{\Delta t}\int_{0}^{\Delta t} \varphi(t)dt \tag{2-20}$$

It is often helpful to describe the 'time averaged' behavior of a certain fluctuating behavior to observe the effect of turbulence on the flow over a given period of time. Thus, the time averaged behavior is defined as:

$$\overline{\varphi'} = \frac{1}{\Delta t}\int_0^{\Delta t} \varphi'(t)dt \tag{2-21}$$

Integrating the square of the fluctuating flow property over time produces an expression for the variance of the flow property, defined as:

$$\overline{(\varphi')^2} = \frac{1}{\Delta t}\int_0^{\Delta t} (\varphi')^2 dt \tag{2-22}$$

A common way to describe the fluctuations specifically of velocity components of a flow (i.e. u', $v'$and w') is to express the variance as the root means square (or RMS) of the flow property. This is given by the expression:

$$\varphi_{RMS} = \sqrt{\overline{(\varphi')^2}} = \left[\frac{1}{\Delta t}\int_0^{\Delta t} (\varphi')^2 dt\right]^{1/2} \tag{2-23}$$

Expressing velocity components in terms of the RMS produce an easy to measure metric for the characteristics of turbulence in a given flow. Expressing the fluctuating x, y and z-velocity components as $\overline{(u')^2}$, $\overline{(v')^2}$ and $\overline{(w')^2}$ allow for a means to relate these components to the time-averaged Navier-Stokes equations, the associated momentum fluxes produced by turbulent eddies, and the subsequent normal stresses which result in these fluctuations [76].

Another useful definition related to the RMS values of the velocity components is the turbulent kinetic energy, expressed as half the sum of the RMS values of all the velocity components. Thus in a flow with x, y and z-velocity components, the turbulent kinetic energy *per unit mass* is expressed as:

$$k = \frac{1}{2}\left(\overline{(u')^2} + \overline{(v')^2} + \overline{(w')^2}\right) \tag{2-24}$$

Eq. (2-24) is a direct measure of the energy due to the random fluctuations of eddies formed in the turbulent flow in a per unit mass form. One more useful term for describing turbulence is the turbulence intensity (T_i). The expression for turbulence intensity

$$T_i = \frac{\left(\frac{2}{3}k\right)^{1/2}}{U_{ref}} \tag{2-25}$$

describes the ratio of the kinetic energy produced in the flow by the fluctuating velocity components to those of the mean or large scale reference velocity, U_{ref} which is generally taken as the average velocity in the flow. Turbulence intensity is a measure of 'how turbulent' the flow is relative to the average values of the flow [75].

2.2.2 Turbulent Modeling Description

The conservation laws and equations of state (Eq. (2-1) - (2-6)) represent the most generic form of the equations necessary to describe an instantaneous, viscous, compressible, non-reacting, single phase, mixture in which body forces and external heating are absent. In numerical modeling it is necessary to specify turbulent characteristics of the flow, as well as the scale of interest in the problem at hand. A model which is generic and accounts for both turbulence characteristics and also all length and time scales of interest (the entire Kolmogorov scale) is known as a Direct Numerical Simulation (DNS) [76], [80].

These simulations are designed to directly calculate the entire energy spectrum in a given fluid problem. Due to the complexity of turbulent problems, and computational limitations, DNS problems are limited to a set, fixed number of cases, generally limited to computational power and memory. Several authors

have suggested that the number of grid points required to resolve the finest levels of detail with DNS scales with the fourth power of Reynolds number [80], [79].

For problems involving supersonic flows this would suggest constructing a simulation domain with 10-100 billion grid points which is impractical with current computational technology [81]. To model turbulent flows in which the global averaged effects are described, time averaging reformulations of the Navier-Stokes equations have been introduced [82]. These are based on the averaging techniques of Reynold's decomposition and are known as Reynold's Averaged Navier-Stokes Equations (RANS) equations [76]. For globally stable flows and industry standard problems, RANS descriptions are adequate for modeling turbulence on a macroscopic time scale, where time dependent effects are minimal.

RANS formulations are appropriate for problems in which only time-averaged information of the flow properties is important. When investigating strongly time dependent fluid phenomena (e.g. mixing, shear layer growth or vortex rollup) other approaches are necessary [81]. In the interest of limited computational resources, a type of model which can selectively resolve small scales accurately, while still saving on computational cost are necessary. Scale Resolving Simulations (SRS) are the type of turbulence models which bridge the gap between DNS and RANS models. Two types of SRS models which bridge the DNS/RANS gap are Large Eddy Simulations (LES) and Detached Eddy Simulations (DES) [81].

Large Eddy Simulations are simulation techniques which compute the large scale flow structures while modeling the smallest scales [80]. It is surmised that the largest flow structures are influenced directly by choice of boundary condition, but the smallest scales can be assumed to be nearly isotropic and are more appropriate for modeling [80]. Since the smallest scales can be modeled, LES time grid size and time step requirements are significantly reduced in comparison to

DNS. LES uses spatial filtering which separates the flow into large scale eddies which are calculated directly (resolved scale) and small scale eddies (sub-grid scale or SGS) which are modeled (usually employing a RANS model) is used to calculate flow properties [76]. Strict resolution requirements for LES models particularly in wall-bounded flows limit the practicality of LES. Hybrid LES/RANS models knows as Detached Eddy Simulations (DES) have been proposed which allow for switching between LES and DES based on the provided grid resolution [81]. For the purposes of this study, a brief description of the formulation of RANS, LES and DES will be presented, followed by the specific aspects of the application. The discussion is in the subsequent sections.

2.2.3 Favre Averaged and Filtered Governing Equations

2.2.3.1 Filtering Operations

To fully describe compressible turbulent flows it is necessary to employ a description similar to the Reynolds Time Averaging that also accounts for effects of compressibility. A filter based Reynolds averaging operation called Farve-Averaged filtering is often introduced in LES to decompose the flow properties in such a form that the largest scales are resolved but the smallest scales are modeled. The formulation of the filtered conservation and state equations is not closed without the introduction of a new set of equations which describe the scales below the filter size (sub-grid scale) flow properties. This will be discussed in further detail in the subsequent sections. Filtering involves the decomposition of a flow variable into resolved (filtered) and unresolved (unfiltered) components often described as 'sub-grid scale' or SGS components because these properties are modeled and not calculated directly since they fall under a scale less than the decided grid length (often denoted by Δ) [81].

2.2.3.2 Favre Averaging Operations

In LES compressible flows, many authors employ the use of a change of variable which averages the filtered variable based on a 'density weighted average' [83]. For the generic flow variable φ after filtering can be related to the 'averaged density' $\bar{\rho}$ by the following expression:

$$\bar{\rho}\tilde{\varphi} = \overline{\rho\varphi} \tag{2-26}$$

where variables involving the Reynolds operator denoted with the overbar ($\bar{\cdot}$) represent the filtered component associated with the filter size Δ. From the previous expression, any flow variable can be expressed as in terms of a density averaged filtered (or resolved) component and an un-filtered or un-resolved component. The following expression is often used to describe the decomposition of scalar or vector φ into a low frequency component ($\tilde{\varphi}$) and a high frequency component (φ''):

$$\varphi = \tilde{\varphi} + \varphi'' \tag{2-27}$$

where the tilde operator ($\tilde{\cdot}$) is a linear one and is not commutative spatially or temporally with differential operation. Garner *et al.* [83] describes the following relationships for density averaged differential operation:

$$\widetilde{\nabla \cdot \varphi} \neq \nabla \cdot \tilde{\varphi}, \quad \widetilde{\frac{\partial \varphi}{\partial t}} \neq \frac{\partial \tilde{\varphi}}{\partial t} \tag{2-28}$$

Also, the following stipulations are true regarding the use of the Reynolds operator:

$$\overline{\rho\varphi''} = 0, \qquad \bar{\varphi} - \tilde{\varphi} = \varphi'' = -\frac{\overline{\rho'\varphi''}}{\bar{\rho}} = -\frac{\overline{\rho'\varphi''}}{\bar{\rho}} \tag{2-29}$$

This expression leads to analogy with Favre time averaging. An example of the benefit of these relationships is the avoidance of an extra un-resolved term which appears in the momentum conservation law after Favre time averaging by

transforming the term $\overline{\rho \boldsymbol{u}}$ to $\bar{\rho}\tilde{\boldsymbol{u}}$. A more complete description of this transformation can be found in Garnier *et al.* [83], Vremen *et al.* [84] or Pope [79].

The subsequent expressions describe the Farve-Averaged filtered instantaneous, viscous, compressible, single phase gas mixture conservation laws and state equations. The following formulation of the conservation laws and state equations are presented, based on the works of Refs. [83], [84] written in a vector notation consistent with Ref. [74]:

$$\frac{\partial \bar{\rho}}{\partial t} + \nabla \cdot (\bar{\rho}\tilde{\mathbf{u}}) = 0 \tag{2-30}$$

$$\frac{\partial \bar{\rho}\tilde{\mathbf{u}}}{\partial t} + \nabla \cdot (\bar{\rho}\tilde{\mathbf{u}}\tilde{\mathbf{u}} + \bar{p}\boldsymbol{\delta} - \bar{\boldsymbol{\tau}} + \boldsymbol{\tau}^{\boldsymbol{sgs}}) = 0 \tag{2-31}$$

$$\frac{\partial \tilde{E}}{\partial t} + \nabla \cdot [\tilde{E}\tilde{\mathbf{u}} + (\bar{p}\boldsymbol{\delta} - \bar{\boldsymbol{\tau}}) \cdot \tilde{\mathbf{u}} - \tilde{\kappa}\nabla\tilde{T} + \boldsymbol{H}^{sgs} + \bar{q}^{sgs} + \boldsymbol{\sigma}^{\boldsymbol{sgs}}] = 0 \tag{2-32}$$

$$\frac{\partial \bar{\rho}\tilde{Y}_{\kappa}}{\partial t} + \nabla \cdot \left(\bar{\rho}\tilde{\mathbf{u}}\tilde{Y}_{\kappa}\right) - \nabla\left(\bar{\rho}\tilde{D}_{\kappa}\nabla\tilde{Y}_{\kappa}\right) + \nabla \cdot Y^{sgs} + \nabla \cdot \theta^{sgs} = 0 \tag{2-33}$$

$$\bar{P} = \bar{\rho}(\tilde{R}\tilde{T} + T^{sgs}) \tag{2-34}$$

$$\tilde{E} = \frac{\tilde{p}}{\gamma - 1} + \frac{1}{2}\bar{\rho}\tilde{\mathbf{u}} \cdot \tilde{\mathbf{u}} + k^{sgs} \tag{2-35}$$

where new terms for sub-grid scale flow conditions marked with the $(\cdot^{sgs})$ superscript describe the unresolved or sub-grid scale expressions for the turbulence properties in these equations. A definition for the filtered shear stress tensor, $\bar{\boldsymbol{\tau}}$ is expressed in the following manner:

$$\bar{\boldsymbol{\tau}} = \tilde{\mu}(2\bar{\boldsymbol{S}}) - \frac{2}{3}\tilde{\mu}(\nabla \cdot \tilde{\boldsymbol{u}})\boldsymbol{\delta} = 0 \tag{2-36}$$

where

$$\bar{\boldsymbol{S}} = \frac{1}{2}(\nabla\tilde{\boldsymbol{u}} + (\nabla\tilde{\boldsymbol{u}})^{\boldsymbol{T}}) = 0 \tag{2-37}$$

Eq. ((2-30)-(2-38)) are open and cannot be solved in the current form without introducing additional equations for all the SGS terms. At this juncture the

description of closure and the choice of SGS model is appropriate to describe how these equations are to be solved.

2.2.4 Closure Description

Application of the Reynolds time average operation to the Navier-Stokes equation or analogously, the application of the Reynold's filter operations to the same set of equations produce additional terms that account for turbulent effects [80]. For instance, the momentum equation takes the following form when the time averaged operation is applied:

$$\frac{\partial \rho \mathbf{u}}{\partial \mathrm{t}} + \nabla \cdot \left(\rho \mathbf{u}\mathbf{u} + p\bar{\boldsymbol{\delta}} - \bar{\boldsymbol{\tau}} - \overline{\boldsymbol{\rho u' u'}} \right) = 0 \tag{2-38}$$

The extra term $\overline{\boldsymbol{\rho u' u'}}$ in Eq. (2-38) is known as the *Reynolds stress*. The entire goal of closure is to introduce relations which can somewhat accurately predict the behavior of turbulence, by making assumptions about the Reynolds stress terms or the SGS terms. There have been several attempts to model turbulent stresses and fully close the Reynolds averaged and filtered general equations [79].

In 1877, French physicist and mathematician Joseph Boussinesq introduced a concept known as eddy viscosity which relates the Reynolds stress to the mean rate of deformation associated with strain in a fluid similar to the linear stress-strain relationship based on molecular viscosity [76]. Expressed in indicial notation, an equation which describes this relationship is of the following form:

$$\tau_{ij} = -\overline{u_i' u_j'} = \mu_t \left(\frac{\partial u_i}{\partial u_j} + \frac{\partial u_j}{\partial u_i} \right) - \frac{2}{3} \rho k \delta_{ij} \tag{2-39}$$

where k represents the turbulent kinetic energy defined by Eq. (2-24) and μ_t is the *turbulent eddy viscosity* coefficient. Note the similarity in form between stress equation written here and the one written in Sec. 2.1. In addition to this specification for the stress-strain relationship it is imperative to define the turbulent viscosity and a length scale to describe the turbulence.

The class of models which attempt to close the general equations via turbulent eddy viscosity are called linear eddy viscosity models (EVM). Other classes of RANS models exist such as the non-linear eddy viscosity models (NEVM) and Reynolds Stresss Models (RSM) but are not pertinent to this study and will be excluded for brevity. Within the group of eddy viscosity models are a sub-set of models known as the 'n-equation models', named for the number of equations used to solve for the turbulent eddy viscosity coefficient. These include the *algebraic (or zero-equation)* model, the *one-equation models* and the *two-equation models*. One of the most widely used EVM is known as Menter's SST model (a two-equation model which solves Eq. (2-38) for turbulent kinetic energy (k) and specific dissipation or turbulent frequency (ω)). This model will be discussed briefly since it has been used in this study.

Algebraic or zero-equation models are so named due to the fact that no additional equations and solutions are introduced for closure. Thus the value for μ_t is calculated directly from flow variables. Algebraic models are simpler to use but fail to account for turbulent effects such as convection and turbulent diffusion. Zero-equation models were introduced by Ludwig Prandtl in the 1920's, where they make use of the mixing length concept, relating it to turbulent eddy viscosity in the following relation:

$$\mu_t = \rho l^2 \left|\frac{dU}{dy}\right| \tag{2-40}$$

where l is the mixing length, associated with the average length a fluid eddy travels prior to momentum exchange and subsequent mixing with other fluid particles.

Given the limitations of algebraic models, developmental work has improved turbulence models to include an additional equation which directly calculates turbulent kinetic energy and relates it to the turbulent eddy viscosity. These are the one equation models, which are based on original works from Kolmogorov

and Prandtl but have been modified by Spallart, Baldwin and others [82]. Based on the suggestion by Prandtl in the 1920's and later by Kolmogorov in 1940, a form to evaluate the turbulent eddy viscosity based on turbulent kinetic energy is:

$$\mu_t = C_k \rho l (k)^{1/2} \tag{2-41}$$

where C_k is a constant which must be specified. The turbulent kinetic energy equation can be expressed in the formulation mentioned in Tannehill *et al.* by the following expression [82]:

$$\rho \frac{Dk}{Dt} = \frac{\partial}{\partial x_j}\left[\left(\frac{\mu + \mu_t}{Pr_k}\right)\frac{\partial k}{\partial x_j}\right] + \left(2\mu_T S_{ij} - \frac{2}{3}\rho k \delta_{ij}\right)\frac{\partial u_i}{\partial x_j} - C_D \frac{\rho k^{3/2}}{l} \tag{2-42}$$

where the rates of k increase, diffusion, generation and dissipation are expressed from left to right.

The one-equation and two-equation models both make use of the hypothesis developed by Bossinesq, which linearly relates shear stress to the rate of deformation. However, the one-equation models are incomplete, as they can only be used to predict scalar turbulent transport phenomena [80]. Also, the accuracy of the one equation models are limited; these models have difficulty handling problems in which there's an imbalance of turbulent production and dissipation.

In general, some flows necessitate the tracking of convective and diffusive phenomena. Examples of such problems are shear layers and separated flows present situations in which convection and diffusion produce significant changes in turbulence generation and destruction and require a more complex model than the mixing length model. A second partial differential equation is therefore necessary to track the effects of dissipation and turbulence length scale effects, thus completing the set of general equations [82].

An expression of the turbulent eddy viscosity in terms of eddy dissipation rate is thus introduced in the form [80]:

$$\varepsilon = \nu_T \overline{\frac{\partial u_i' u_i'}{\partial x_k x_k}} \tag{2-43}$$

where ν_T is the turbulent kinematic eddy viscosity. This allows a relationship between turbulent eddy viscosity and to both the length scale and turbulent kinetic energy by the following:

$$\varepsilon \propto \frac{k^{3/2}}{l} \tag{2-44}$$

thus

$$\mu_t = \rho C_\mu \frac{(k)^2}{\varepsilon} \tag{2-45}$$

where C_μ is a constant which must be specified.

The class of two-equation models which use the aforementioned formulation for turbulent eddy viscosity are called k- ε models. Several authors [82], [76], [85] have proposed modifications to the formulation which use a 'turbulent frequency' or ω as the variable to describe the turbulent length scale, also introducing a second transport equation dependent on ω. This new length scale is related to turbulent kinetic energy and turbulent eddy viscosity by the following:

$$l = \frac{\sqrt{k}}{\omega} \tag{2-46}$$

thus

$$\mu_T = \rho \frac{k}{\omega} \tag{2-47}$$

Two equation models which use this formulation are known as k- ω models. Several improvements can be made from the use of the k- ω models, including mitigation of in accuracies in k- ε in the near-wall region of boundary layer flows, especially those with adverse pressure gradients [76]. Using the k- ω seems to improve the accuracy in such cases, while still providing numerical stability and simplicity over the k- ε model.

2.2.5 Menter's SST Model

Menter [85] developed a hybrid model which maximizes benefits of both the k-ω and k-ε models. Menter found that though the k-ω formulation produced better performance for near-wall problems, was also is very sensitive to inlet free stream turbulent specifications, failed to accurately predict both the asymptotic behavior of turbulence near the wall in wall bounded flows, and turbulent kinetic energy and turbulent eddy dissipation distributions when compared to DNS solutions [85].

A widely used linear eddy viscosity models which alleviated the problems involving inlet turbulent conditions and turbulence near the wall in wall bounded flows is the Menter Shear Stress Transport model (colloquially referred to as the Menter SST model). The following formulation represent the full closure of the general conservation laws based on Menter [85].

$$\frac{D\rho k}{Dt} = \tau_{ij}\frac{\partial u_i}{\partial x_j} - \beta^*\rho\omega k + \frac{\partial}{\partial x_j}\left[(\mu + \sigma_T\mu_T)\frac{\partial k}{\partial x_j}\right] \tag{2-48}$$

$$\frac{D\rho\omega}{Dt} = \frac{\gamma}{\nu_T}\tau_{ij}\frac{\partial u_i}{\partial x_j} - \beta^*\rho\omega^2 + \frac{\partial}{\partial x_j}\left[(\mu + \sigma_\omega\mu_T)\frac{\partial \omega}{\partial x_j}\right] + 2(1 - F_1)\rho\sigma_{\omega 2}\frac{1}{\omega}\frac{\partial k}{\partial x_j}\frac{\partial \omega}{\partial x_j} \tag{2-49}$$

Closure and auxiliary constants include:

$$F_1 = tanh\left[\left(max\left(\frac{2}{\beta^*}, \frac{500\nu}{y^2\omega}\right)\right)^2\right] \tag{2-50}$$

$$F_2 = tanh\left[\left(max\left(\frac{2}{\beta^*}, \frac{500\nu}{y^2\omega}\right), \frac{4\sigma_{\omega 2}k}{CD_{k\omega}y^2}\right)^2\right] \tag{2-51}$$

$$CD_{k\omega} = max\left(2\rho\sigma_{\omega 2}\frac{1}{\omega}\frac{\partial k}{\partial x_i}\frac{\partial \omega}{\partial x_i}, 10^{-10}\right) \quad (2\text{-}52)$$

$$\phi = \phi_1 F_1 + \phi_2(1 - F_2) \quad (2\text{-}53)$$

$$\sigma_{k1} = 0.85, \quad \sigma_{\omega 1} = 0.5, \quad \beta_1 = 0.0750, \quad a_1 = 0.31 \quad (2\text{-}54)$$

$$\beta^* = 0.09, \quad \kappa = 0.41, \quad \gamma_1 = \frac{\beta_1}{\beta^*} - \sigma_{\omega 1}\frac{\kappa}{\sqrt{\beta^*}} \quad (2\text{-}55)$$

2.2.6 Large Eddy Simulations: Sub-Grid Scale Modeling

To summarize the description of LES in Sec. 2.2.2, Large Eddy Simulations use filtering to allow for the resolution of the largest turbulent eddies, while modeling the flow features below a specified filter width (Δ) usually taken as a grid spacing dimension. In Modeling Turbulence with CFD, Wilcox states that the "fundamental problem of Large Eddy Simulations is the formulation of an appropriate sub-grid scale model which closes the general equations by representation of the sub-grid scale stresses" [80].

To fully close the filtered conservation and state equations (Eq. (2-30)-(2-37)), specifications are necessary for the sub-grid scale terms. Several techniques have been proposed and employed, ranging from eddy viscosity and gradient-diffusion models such as Smagorinsky's 1963 model , through more recent second order and non-linear models such as the model proposed by Deardorff in 1977 and by Brahmin *et al.* in 1983 [82]. Modifications to earlier models have included the works of Shur *et al.* [86] and Piomelli [87]. Smagorinsky [88] proposed an approximation for the sub-grid scale stresses which assumes that the sub-grid stress has gradient diffusion behavior similar to molecular viscosity, and thus represented the unresolved stress in the following formulation [80], [88]:

$$\tau_{ij} = -2\mu_{sgs}\bar{S}_{ij} + \frac{1}{3}\tau_{ii}\delta_{ij} \quad (2\text{-}56)$$

where

$$\bar{S}_{ij} = \frac{1}{2}\left(\frac{\partial \overline{u_i}}{\partial u_j} + \frac{\partial \overline{u_j}}{\partial u_i}\right) \tag{2-57}$$

To define the unresolved or sub-grid turbulent viscosity, μ_{sgs}, the Smagorinsky SGS model make use of the Prandtl mixing length concept (similar to algebraic RANS models) by hypothesizing that a length scale and velocity scale are necessary to describe μ_{sgs}. An obvious choice for the length scale is the filter length (or equivalently, the grid spacing) Δ, since it essentially the upper limit of the largest un-resolved eddies. The velocity scale is represented by the product of the length scale Δ and the mean strain rate, $|\bar{S}_{ij}|$, and thus μ_{sgs} is defined as:

$$\mu_{sgs} = \rho(C_s\Delta)^2 \left|\bar{S}_{ij}\right| = \rho(C_s\Delta)^2\sqrt{2\bar{S}_{ij}\bar{S}_{ij}} \tag{2-58}$$

where C_s is the Smagorisnky coefficient. The Smagorinsky coefficient is not a universal value but can vary from problem to problem. In 1970, Lilly [89] suggested that C_s= 0.1 was the most appropriate value for most cases. The combination with Lilly's model is a popular LES SGS closure model known as the Smagorinsk*y*-Lilly model [80]

A notable characteristic of LES models are the high sensitivity to Reynold's number. The resolution requirements particularly for wall bounded flows are staggering. Menter [81] presents a table (see Table 1) for describing the grid point requirements for channel flow of domain half height (h) when using a wall-

Table 1. Reynolds Number Based Grid Requirements

Parameter	Case 1	Case 2	Case 3	Case 4
$\boldsymbol{Re_\tau}$	500	10^3	10^4	10^5
$\boldsymbol{N_T}$	5.0x10^5	1.8x10^6	1.8x10^8	1.8x10^{10}

resolved LES model: where the total number of grid points (N_T) scales with Reynolds number (Re_τ) (based on the friction velocity u_τ). Note that in Table 1, the order of magnitude for grid points N_T is almost doubled for a given Re_τ. This suggests highly demanding computational resources even for relatively simple flow problems. Here the definitions of N_T and Re_τ are as follows:

$$N_T = N_x N_y N_z \tag{2-59}$$

and

$$Re_\tau = \frac{u_\tau h}{\nu}, \qquad N_x = \frac{8h}{\Delta x} = \frac{8Re_\tau}{\Delta x}, \qquad N_z = \frac{3h}{\Delta z} = \frac{3Re_\tau}{\Delta z} \tag{2-60}$$

Menter reports that the classical requirements for a channel flow with LES based on grid point and wall units in the x, y and z direction are the following expressions:

$$\Delta x^+ = 40, \ \Delta z^+ = 20, \ N_y = 60 - 80 \tag{2-61}$$

These are defined as:

$$\Delta x^+ = \frac{u_\tau \Delta x}{\nu}, \qquad \Delta z^+ = \frac{u_\tau \Delta z}{\nu} \tag{2-62}$$

where the wall friction velocity is defined in terms of wall shear stress τ_w, and average fluid density ρ [81]:

$$u_\tau = \sqrt{\frac{\tau_w}{\rho}} \tag{2-63}$$

An algebraic wall-modelled Large Eddy Simulation formulation (WMLES) was proposed by Shur *et al.* in 2008 to relax the resolution requirements for LES [86]. The *WMLES-Omega* model combines the mixing length approach of Smagorinsky (with modifications) and a damping approach suggested by Piomelli [87]to formulate the following closure relationship for the SGS turbulent kinematic viscosity, ν_T based on the filter length Δ [87]:

$$\nu_T = \min[(\kappa d_w)^2, (C_s\Delta)^2]\left[1 - e^{\left(-\frac{y^+}{25}\right)^3}\right]\text{abs}\left|\bar{S}_{ij} - \Omega\right| \tag{2-64}$$

where d_w is the wall distance, $\bar{S}_{ij}$ the strain rate, y^+ the non-dimensional wall distance in the wall normal direction, and constants $\kappa = 0.41$ and $C_s = 0.2$. The filtered grid spacing Δ has the following description to account for an-isotropic behavior in the wall regions:

$$\Delta = \min(\max(C_w \cdot d_w;\ C_w \cdot h_{max}, h_{wn}); h_{max}) \tag{2-65}$$

In this formulation, the Smagorinsky constant near the wall is $C_w = 0.15$, h_{max} is the largest distance in a hexahedral grid cell, and h_{wn} is the wall-normal spacing distance [81], [80].

The modification of the WMLES-Omega model from the original WMLES formulation is the additional term ($\text{abs}\left|\bar{S}_{ij} - \Omega\right|$), where Ω represents the vorticity magnitude in the flow. This modification accounts for the improper calculation of eddy viscosity in flows with constant shear in the original formulation of WMLES with the simple $\bar{S}_{ij}$ term. The modification allows for improvements of modeling the eddy viscosity in cases where there is constant shear (zero eddy viscosity) or flows with separation [81].

The most obvious benefit from the WMLES formulation is the improvement of the grid requirements. Menter reports that for a wall bounded channel flow of half height h or equivalently of boundary layer thickness δ the required grid resolution in terms of δ is [81]:

$$N_x \approx \frac{\delta}{\Delta x} \approx 10,\ N_y = 30 - 40, N_z \approx \frac{\delta}{\Delta z} \approx 20 \tag{2-66}$$

The implication of Eq. (2-66) is that for a boundary layer flow of height δ, one needs approximately 6000 – 8000 cells to cover about one boundary layer volume $\delta \times \delta \times \delta$.

The ANSYS FLUENT R15 Theory Guide shows a comparison of grid sizes and CPU effort between the LES and WMLES approaches. These results can be seen in Table 2:

Table 2. Grid Resolution Comparison between LES and WMLES

Parameter	Case 1	Case 2	Case 3	Case 4
Re_τ	500	10^3	10^4	10^5
N_T	$5.0x10^5$	$5.0x10^5$	$5.0x10^5$	$5.0x10^5$
Ratio LES/ WMLES	1	4	$4.0x10^2$	$4.0x10^4$
Ratio CPU effort LES/WMLES (CFL = 0.3)	1	10^1	10^4	10^7

In Table 2, it can be seen that the required number of grid points can drastically be reduced using a WMLES formulation. It is clear that at higher Re_τvalues, the requirements reduce the grid spacing by several orders of magnitude, saving computational time and complexity. Limitations of LES even with the WMLES formulation include the large number of cells required for minimal resolution, and limitations on the required time step size. Alternative approaches to LES include hybrid LES/RANS models [86].

2.2.7 Detached Eddy Simulation Models

To alleviate the strict grid requirements and limitations of LES models, Detached Eddy Simulations (DES) methods were introduced by Philipe Spalart and several others (e.g. Spalart *et al.* [90], Strelets [91]). Spalart *et al.* proposed that a hybrid RANS/LES model be introduced which resolves the largest eddy structures but switches to a RANS formulation near regions in the computational domain (e.g. near walls or in boundary layer flows) which are not easily resolved on a courser grid [90].

It was found that the DES formulation could be implemented more simply both in its relatively low grid cost (in comparison to LES) and also in that it could be built into an already existing RANS turbulence model. The switching criterion between RANS and LES as is described in DES is defined by the following:

$$C_{DES}\Delta_{max} > L_t \rightarrow RANS; \tag{2-67}$$

$$C_{DES}\Delta_{max} \leq L_t \rightarrow LES; \tag{2-68}$$

where

$$\Delta_{max} = \max(\Delta_x \Delta_y \Delta_z) \tag{2-69}$$

thus Δ_{max} describes the local maximum edge length in the x, y and z directions of a given cell.

An example of a DES formulation based on the k-ω turbulence model is of the following form [81].

$$\frac{\partial(\rho k)}{\partial t} + \frac{\partial\left(\rho \bar{U}_j k\right)}{\partial x_j} = P_k - \rho \frac{k^{3/2}}{\min(L_t, C_{DES}\Delta_{max})} + \frac{\partial}{\partial x_j}\left(\left(\mu + \frac{\mu_t}{\sigma_k}\right)\frac{\partial k}{\partial x_j}\right) \tag{2-70}$$

$$L_t = \frac{k^{3/4}}{\varepsilon} = \frac{\sqrt{k}}{\beta^* \omega} \tag{2-71}$$

In this formulation the DES limiter can switch between LES mode and RANS mode based on the relationship $\Delta_{max} \leq L_t$. Menter describes the design emphasis as a model which is intended 'to run in RANS mode for attached flow regions, and switch to LES mode in detached regions away from the wall'. This of course is where the title of the model is derived.

A modification of the DES model has recently been used to improve the implementation of DES. An undesirable effect known as Grid-Induced Separation

(GIS) was discussed by Menter and Kunz [92] which result from inaccurate delimitation, the effect of which can cause boundary layers to separate at arbitrary locations based on changes in grid density [81]. The Delayed DES (DDES) also implemented by Spalart *et al.* [93] obviated this problem, employing a shielding function which is included in the following expression for the dissipation term in the turbulent kinetic energy equation (*k*):

$$E_{DES} = \rho \frac{k^{3/2}}{L_t, \min(L_t, C_{DES}\Delta)} = \rho \frac{k^{3/2}}{L_t} max\left(1; \frac{L_t}{C_{DES}\Delta}\right) \quad (2\text{-}72)$$

$$E_{DDES} = \rho \frac{k^{3/2}}{L_t} max\left(1; \frac{L_t}{C_{DES}\Delta}(1 - F_{DDES})\right) \quad (2\text{-}73)$$

where the shielding function F_{DDES} is equal to 1 inside the wall boundary layer and 0 away from wall regions in the flow.

2.3 Numerical Methodology and Approach

This study employs the use of the ANSYS commercial computational tool using both Design Modeler for the construction of a numerical grid and FLUENT R15 for the CFD solver. A brief discussion of the model discretization, solver schemes, solver algorithms used specifically in this study are presented in the subsequent discussion.

2.3.1 Control Volume Approach and Cell-Flux Discretization

ANSYS FLUENT employs a control volume technique to solve the set of conservation equations, state equations and transport equations for the entire computational domain. Thus the solution of the flow field for the problem of interest involves solving the general unsteady control volume integral equation

for a scalar quantity, represented by ϕ over a generic control volume V of the following form:

$$\int_V \frac{\partial \rho \phi}{\partial t} dV + \oint \rho \phi \vec{v} \cdot d\vec{A} = \oint \Gamma_\phi \nabla \phi \cdot d\vec{A} + \int_V S_\phi dV \qquad (2\text{-}74)$$

where

ρ = density
$\vec{v}$ = velocity vector
$\vec{A}$ = surface area vector
Γ_ϕ = diffusion coefficient for ϕ
$\nabla\phi$ = gradient of ϕ
S_ϕ = source of ϕ per unit volume

During the solution process, the conservation equation is discretized and applied to each cell volume in the computational domain. The fluid property ϕ is calculated at all of the cells across the domain. The discretized equation on a given cell yields the following expression:

$$\frac{\partial \rho \phi}{\partial t} dV + \sum_i^N \rho_i \phi_i \vec{v}_i \cdot \vec{A}_i = \sum_i^N \Gamma_\phi \nabla \phi_i \cdot \vec{A}_i S_\phi V \qquad (2\text{-}75)$$

where

N = number of faces of the cell
ϕ_i = value of ϕ, convected through the *i*th face
$\rho_i \phi_i \vec{v}_i \cdot \vec{A}_i$ = mass flux through the *i*th face
$\vec{A}_i$ = area of the *i*th face
$\nabla\phi_i$ = gradient of ϕ at the *i*th face
V = cell volume

Further description is due in the subsequent section for the term $\frac{\partial \rho \phi}{\partial t} dV$ which is introduced in the description for temporal discretization. The FLUENT Theory Guide [94] explains that these equations which ANSYS FLUENT solves are general for all types of cells including both 2D and 3D geometries, as well as unstructured meshes and polyhedral cells [94].

2.3.2 Spatial and Temporal Discretization

ANSYS FLUENT includes a second-order upwind scheme which uses a multidimensional linear reconstruction approach to compute quantities at the cell faces via a Taylor series expansion of the solution based on a cell-centered description [94], [95]. The following equation describes how a face value $\phi_{i,2}$ is computed in FLUENT when second-order upwinding is selected [94]:

$$\phi_{i,2} = \phi + \nabla\phi \cdot \vec{r} \tag{2-76}$$

where $\phi_{i,2}$ represents the quantity at the ith face being calculated, and ϕ and $\nabla\phi$ are the quantity and its gradient (already known) in the cell-centered description upwind of the calculated quantity. The displacement vector, $\vec{r}$ is the distance from the face centroid to the upstream (upwind) cell centroid. In this formulation, the gradient $\nabla\phi$ is calculated via the gradient formulation (see Sec. 2.3.3) and has limits to prevent the introduction of new maxima or minima [94].

Temporal discretization also includes the process of integrating the discretized equations only in time over a time step of size Δt. The discretized time formulation describing the change in time of the generic variable ϕ is described in the following manner:

$$\frac{\partial\phi}{\partial t} = F(\phi) \tag{2-77}$$

with $F(\phi)$describing a generic temporal function of ϕ. A formulaic description of the second-order discretization used in this study is explained by the following:

$$\frac{3\phi^{n+1} - 4\phi^{n} + \phi^{n-1}}{2\Delta t} = F(\phi) \tag{2-78}$$

where

ϕ = calculated quantity
$n+1$ = value at time t + Δt
n = value at time t
$n-1$ = value at time t − Δt

2.3.3 Derivative and Gradient Evaluation

An Implicit time integration is used to evaluate $F(\phi)$. This means that at each time step Δt the implicit equation is integrated iteratively before marching forward in time to the next iteration cycle. The formulaic representation of the implicit discretization is the following equation:

$$\phi^{n+1} = \phi^n + \Delta t F(\phi^{n+1}) \tag{2-79}$$

In the previous expression, implicit integration is represented by the relationship between ϕ^{n+1} in given cell, and both ϕ^{n+1} and $F(\phi^{n+1})$ in neighboring cells. The key advantage to using the fully implicit time integration scheme is the unconditional stability in relation to the time step size [94]. As a result, larger time step sizes can be used in implicit schemes, which result in quicker solutions but often with less resolution in comparison with explicit time integration approaches [82].

In grid discretization, several different approaches exist to construct scalar values for cell faces. Also, there exists a balance between convection and diffusion across cell faces which must be evaluated. The gradient $\nabla\phi$ and its scalar ϕ must be discretized along with convective and diffusive terms in the conservation equations. The *discretized* Green-Gauss theorem is employed to compute gradients of scalar at a cell center by the following discrete expression based on the approach proposed by Holmes and Connel [96] and Rauch *et al.* [97]:

$$(\nabla\phi)_0 = \frac{1}{V}\sum_{i}^{N} \bar{\phi}_i \vec{A}_i \tag{2-80}$$

where the subscript '0' represents the location of the center of a cell. Thus ϕ is summed over all *N* faces of the cell. One approach to evaluate the Green-Gauss theorem for all cells is known as the *Green-Gauss Node-Based Gradient Evaluation*, employed in this study. The Green-Gauss Node-Based Gradient Evaluation is an

approach in which the arithmetic average of all node values on face $\bar{\phi}_i$ is calculated in the following manner:

$$\bar{\phi}_i = \frac{1}{N_i}\sum_{n}^{N_n} \bar{\phi}_n \tag{2-81}$$

where the subscript n represents a specific node, and N_n represent the number of nodes on a given face. Several studies have shown that the Green-Gauss Node-Based Gradient Evaluation approach is more accurate than the cell—based gradient approach especially on unstructured grids, but is still more computationally expensive. It was chosen in this study due to its suggested improved accuracy [94].

2.3.4 Density Based Coupled Solver

ANSYS FLUENT has two types of solvers applicable to various types of fluid flow problems including the Pressure Based Coupled Solver (PBCS) and the Density Based Coupled Solver (DBSC). Since the Density Based Coupled solver simultaneously solves the conservation laws (mass, momentum, energy and species) it is more appropriate for problems in which there exists a strong coupling between the density, energy, momentum and species, such as high speed compressible problems involving shock interactions and multiple species [94]. Thus the DBSC model was chosen over the PBSC for the current study.

The governing equations are solved as formulated by the FLUENT Theory Guide in the DBCS in the following form for an arbitrary fluid volume V through a differential surface $d\boldsymbol{A}$ (written in vector form):

$$\frac{\partial}{\partial t}\int_V \boldsymbol{W}\, dV + \oint |\boldsymbol{F} - \boldsymbol{G}| \cdot dA = \int_V \boldsymbol{H}\, dV \tag{2-82}$$

where vectors $\boldsymbol{W}$, $\boldsymbol{F}$, and $\boldsymbol{G}$ represent a collection of variables describing mass, momentum, energy and species, defined as:

$$\boldsymbol{W} = \begin{Bmatrix} \rho \\ \rho u \\ \rho v \\ \rho w \\ \rho e \end{Bmatrix}, \boldsymbol{F} = \begin{Bmatrix} \rho \mathbf{v} \\ \rho \mathbf{v} u + p\hat{\mathbf{i}} \\ \rho \mathbf{v} v + p\hat{\mathbf{j}} \\ \rho \mathbf{v} w + p\hat{\mathbf{k}} \\ \rho \mathbf{v} E + p\mathbf{v} \end{Bmatrix}, \boldsymbol{G} = \begin{Bmatrix} 0 \\ \bar{\tau}_{xi} \\ \bar{\tau}_{yi} \\ \bar{\tau}_{zi} \\ \bar{\tau}_{ij} v_j + \mathbf{q} \end{Bmatrix} \tag{2-83}$$

The vector $\boldsymbol{H}$ represents source terms which include energy sources and body forces. The variables ρ, $\mathbf{v}$, p and e represent the density, velocity, pressure and total energy per unit mass, $\bar{\tau}$ the stress tensor and $\mathbf{q}$ the heat flux [94]. Total enthalpy, H is related to total energy E in the following form:

$$E = H - p/\rho \tag{2-84}$$

where

$$H = h + |\mathbf{v}|^2/2 \tag{2-85}$$

2.3.5 Roe Flu*x*-Difference Splitting Scheme for Convective Fluxes

ANSYS FLUENT offers the Roe Flu*x*-Difference Splitting Scheme to treat the fluxes across cell boundaries. An extensive description of the Roe Flu*x*-Difference Splitting Scheme can be found in [98]. In FLUENT the flux vector **F** is treated as a vector which contains information which is propagates through the domain at the acoustic speed (the speed of sound) and direction which can be described by the eigenvalues of the system. The flux vector **F** is split into parts, each of which contains characteristic information and these parts are subsequently differenced (according to their eigenvalues) such that the following expression for the individual fluxes at each face is obtained:

$$\boldsymbol{F} = \frac{1}{2}(\boldsymbol{F_r} + \boldsymbol{F_l}) - \frac{1}{2}\Gamma|\hat{\mathrm{A}}|\delta\boldsymbol{Q} \tag{2-86}$$

In Eq. (2-86), δQ represents the spatial difference ($\boldsymbol{Q_r} - \boldsymbol{Q_l}$) between solution vectors on the "right" ($\boldsymbol{Q_r}$) and "left" ($\boldsymbol{Q_l}$) sides of the face [94]. Fluxes $\boldsymbol{F_r} =$

$\boldsymbol{F}(\boldsymbol{Q_r})$ and $\boldsymbol{F_l} = \boldsymbol{F}(\boldsymbol{Q_l})$ are calculated from the solution vectors $\boldsymbol{Q_r}$ and $\boldsymbol{Q_l}$**.** The right hand side of Eq. (2-86) include the matrix $\left|\widehat{\mathrm{A}}\right|$ defined as:

$$\left|\widehat{\mathrm{A}}\right| = M|\Lambda|M^{-1} \tag{2-87}$$

Here, Λ is an eigenvalue matrix, A is the inviscid flux Jacobian $\partial \mathrm{F}/\partial Q$ and M is the modal matrix which diagonalizes $\Gamma^{-1}A$ [94]. The FLUENT Theory Guide suggests that in the current formulation, Eq. (2-86) can be viewed as a "second order central difference plus an added matrix dissipation." [94]. The matrix dissipation term on the right hand side of Eq. (2-86) is responsible for upwinding of pressure and flux velocity as well as convicted variables in supersonic flows [94].

2.3.6 Implicit Time Stepping (Dual-Time formulation)

For transient problems, the implicit-time stepping (or dual-time formulation) can be used for the density-based explicit and implicit formulation. Here, it has been used for the DBCS using an implicit discretization formulation. The general form of the dual-time formulation used by ANSYS FLUENT includes a "low Mach number time-derivative unsteady preconditioner to provide accurate results" for "pure convective problems" such as those dealing with simulations of unsteady turbulent flows. The general formulation is as follows:

$$\frac{\partial}{\partial t}\int_V \boldsymbol{W}\, dV + \Gamma\frac{\partial}{\partial \tau}\int_V \boldsymbol{Q}\, dV + \oint |\boldsymbol{F} - \boldsymbol{G}| \cdot dA = \int_V \boldsymbol{H}\, dV \tag{2-88}$$

where real time is denoted by t and the pseudo-time τ_p (for the iteration counter per time step). The time-dependency term (first term) is discretized implicitly in either a first or second-order accurate, rearward differenced in time approach. The formulation of the "semi-discrete" equation is as follows:

$$\left[\frac{\Gamma}{\Delta\tau_p}+\frac{\epsilon_0}{\Delta t}\frac{\partial \boldsymbol{W}}{\partial \boldsymbol{Q}}\right]\Delta\boldsymbol{Q}^{k+1}+\frac{1}{V}\oint|\boldsymbol{F}-\boldsymbol{G}|\cdot dA$$
$$=\boldsymbol{H}-\frac{1}{\Delta t}(\epsilon_0\boldsymbol{W}^k-\epsilon_1\boldsymbol{W}^n+\epsilon_2\boldsymbol{W}^{n-1}) \quad (2\text{-}89)$$

Here, $\epsilon_0=\epsilon_1=1/2$ and $\epsilon_2=0$ produce first order accurate results and $\epsilon_0=3/2$, $\epsilon_1=2$ and $\epsilon_2=1/2$ produce second order results. The variable k is the 'inner iteration counter' and n represents the current (real) time step.

The FLUENT Theory Guide explains that the pseudo-time-derivative is forced towards zero at each physical time level via a series of inner iterations (per time step) using an implicit marching scheme during which the time dependent vectors $\boldsymbol{W}^n$ and $\boldsymbol{W}^{n-1}$ are fixed values and $\boldsymbol{W}^k$is calculated from $\boldsymbol{Q}^k$. Thus, as the pseudo time becomes large ($\tau_p\rightarrow\infty$), $\mathbf{W}(\boldsymbol{Q}^k)$ produces the solution at the next physical time step $\boldsymbol{W}^{n+1}$**.** An important note, is that the desired temporal accuracy is denoted simply by selecting an appropriate Δt, whereas the pseudo-time step τ_p is dictated by the CFL condition of the time-marching scheme [94].

2.3.7 Algebraic Multi-Grid formulation

ANSYS FLUENT uses a multigrid scheme to accelerate the convergence of a solver and therefore reduce the required CPU time for a given solution. The method used in FLUENT includes computation of corrections on a series of course grid prior to producing a final solution [94]. Multigrid approaches allow for the solution to be performed locally on courser grids, based on the assumption that the most course grid should have the smallest amount of error; if the error reduction takes place on the smallest grid, finer grids should have limited effects as the calculation spreads to a larger grid.

The ANSYS FLUENT theory guide describes the basic concept of multigrid in the following manner:

"Consider the set of discretized linear (or linearized) equations given by

$$A\phi_e + b = 0 \tag{2-90}$$

where ϕ_e is the exact solution. Before convergence, there will be a defect d associated with the approximate solution ϕ:

$$A\phi + b = d \tag{2-91}$$

we seek a correction ψ to ϕ such that the exact solution is given by

$$\phi_e = \phi + \psi \tag{2-92}$$

Substituting Eq. (2-92) into Eq. (2-90) gives

$$A(\phi + \psi) + b = 0 \tag{2-93}$$

$$A\psi + (A\phi + b) = 0 \tag{2-94}$$

Now using the Eq. (2-91) and Eq. (2-94) we obtain

$$A\psi + d = 0 \tag{2-95}$$

which is an equation for the correction in terms of the original fine level operator A and the defect d. Assuming the local (high-frequency) errors have been sufficiently damped by the relaxation scheme on the fine level, the correction ψ will be smooth and therefore more effectively solved on the next coarser level." [94]

ANSYS FLUENT has several multigrid cycle options available. the 'F' cycle is used here (a combination of the V and W cycles, see Ref. [94]). The flow process of the F cycle is as follows:

pre sweep → restrict → W cycle → Vcycle → prolongate → post sweep

Performance wise, the F cycle works better than the V cycle and is equivalent to the W cycle. The F cycle is the default AMG cycle for coupled equation sets and also for the scalar energy equation [94].

An AMG smoother known as the Incomplete Lower Upper (ILU) is used, based on the ILU decomposition technique. Thus, any iteration method can be represented as:

$$M(x^{k+1} - x^k) = b - Ax^k \tag{2-96}$$

where the matrix M is an approximation of an original matrix of the form:

$$Ax = b \tag{2-97}$$

Thus, matrix M should be approximately close to A and M^{-1} should have a low operation count. M is then described in the following manner (as an incomplete "lower upper" factorization of the matrix A):

$$M = LU = (D + L_A)D^{-1}(D + U_A) \tag{2-98}$$

Here, L_A and U_A represent the lower and upper tridiagonal elements of matrix A. The matrix D (a diagonal matrix) is calculated in such a way that it satisfies the following condition for the diagonal (D_M) of M (in an element-indexed form):

$$d_{ii} = a_{ii} - \sum_{j<1} \left(\frac{a_{ij} a_{ij}}{d_{jj}} \right) \tag{2-99}$$

Thus, the new solution x^{k+1} is calculated in two symmetric recursive sweeps. The diagonal elements d_{ii} in ILU decomposition are found during the construction of level and stored in memory. The ILU smoother is considered more expensive than the Gauss-Seidel approach, but has improved overall smoothing properties, especially for systems in which block-coupling are solved for in AMG [94].

3 Preliminary Investigation: 2D Pulsed Injection

3.1 Generic Problem Description

From the results of the literature review in Chapter 1 it was suggested that pulsed injection was a promising, minimally intrusive approach to improve the fuel injection performance in scramjet engines. The limited number of existing PJISF studies have focused mostly on experimentation (e.g. Refs. [51], [53]). Kouchi *et al.* studied PJISF in the frequency range between 5 and 40 kHz but used a 2D URANS model which was limited in flow resolution capabilities [54]. To address these limitations this study seeks to extend numerical investigations of pulsed fuel injection into supersonic crossflows to include 3D scale-resolving simulations (SRS).

To narrow the scope of this study, the simulations are limited to cold-flow jet/crossflow interactions (no combustion or heat addition) for consistency with other PJISF studies (e.g. Refs. [53], [51], [58], [54]). Also both Kouchi *et al.* and Pasmurti *et al.* showed that penetration of pulsed jets in compressible crossflows are most strongly influenced by the pulsation frequency (f) (governed by the stroke ratio) and momentum flux ratio J (governed by effective velocity based on cycle averaged injection velocity) [54], [72]. Thus, appropriately chosen simulation boundary conditions dictated by J and f for the study presented here are important to consider. To further limit the scope of this study, the simulations

presented here focus on high frequency ($f > 1kHz$) and low momentum flux ratio ($J \leq 1$) pulsed gaseous hydrogen jets in an air crossflow.

Justification for the choices of frequency range and momentum flux ratio presented in this study are as follows. Limited computational resources impose constraints on the choice of simulation domain size and grid density. Furthermore, many early extensive experiments [99], [100], [101] and numerical models [102], [103] investigating JISF have included hydrogen/air jet injection at ($J \leq 1$) with implications on scramjet combustor design. For instance, You *et al.* [102] and used a DES model to study a low momentum flux ratio JISF ($J = 0.35$) based on the injection characteristics of the HyShot II scramjet engine which was successfully flow in 2002 [104].

Experimental results presented in Refs. [53], [59] and [58] suggest that in supersonic crossflows, penetration and mixing improvement by jet pulsation is most effective for frequency ranges ($f > 1kHz$). Since the numerical simulations of Kouchi *et al.* focused on 5-50 kHz, this study focuses frequencies within this generic range (8-48 kHz). Select frequencies investigated are 8, 16, 24, 32 and 48 to quickly cover the approximate range investigated in Ref. [54].

The approach presented in this study is as follows. A baseline steady JISF case ($J \approx 1$) is simulated to compare the effects of pulsation against. The injection boundary conditions were chosen such that the cycle averaged injection total pressure ($P_{tj_{cycle}}$) and momentum flux ratio (J_{cycle}) are the same as the steady case injection P_{tj} and J:

$$P_{tj_{cycle}} = P_{tj}, \quad J_{cycle} = J \tag{3-1}$$

For consistency with Kouchi *et al.*, a sinusoidal pulsation function was used for all of the pulsed injection cases. The choice of the wave form to describe sinusoidal pulsation was based on the numerical simulation of Binder *et al.* [60]. The instantaneous pulsed injection total pressure $P_{tj}(t)$ of the PJISF cases all use a

shifted sinusoidal pulsing function based on the wave form in introduced in the numerical simulations of Bender *et al.* :

$$P_{tj}(t) = P_{tj} + P_{tA}\sin(2\pi f t) \tag{3-2}$$

where P_{tA} is the amplitude of pulsation about the mean injection total pressure P_{tA}. P_{tA} is the approximately the same injection total pressure used in the steady case. The instantaneous total pressure ($P_{tj}(t)$) and momentum flux ratio $J(t)$ will vary by their amplitudes during a pulsation cycle. However, since in a shifted sine wave, integration over the period gives the average value of pulsation (see Eq. (1-38)), Eq. (3-1) holds true.

The jet penetration trajectory for JISF is generally constructed from specie concentration profile samples taken at various domain locations (x/D). For consistency with Ref. [54] for all simulations in this study jet penetration at a given x/D is defined as 10% of the maximum value of scalar concentration as measured from the highest location y/D from the wall. Scalar concentration uses the mean mass fraction ($\bar{Y}_{max}$) to measure penetration

Limited computational resources also drive the focus of the frequency range investigations. As a result, the study is initiated with a preliminary more general 2D investigation followed by the primary 3D investigation. The goal of the 2D study is not compare 2D and 3D results, but to serve as a tool to guide the investigation of the effects of frequency on penetration for further focus on the selection of a specific frequency further investigate in the 3D simulation. The remainder of this Chapter 3 focuses on the preliminary 2D studies. The goal of the preliminary 2D study is twofold. First, to qualitatively observe the effects of pulsation on penetration in the range ($8 < f < 48\ kHz$) and second, to down select a frequency in or near the optimal range suggested by Kouchi *et al.* and use that as a focal point for the primary investigation.

3.2 2D Investigations

3.2.1 Problem Setup & Boundary/Initial Conditions

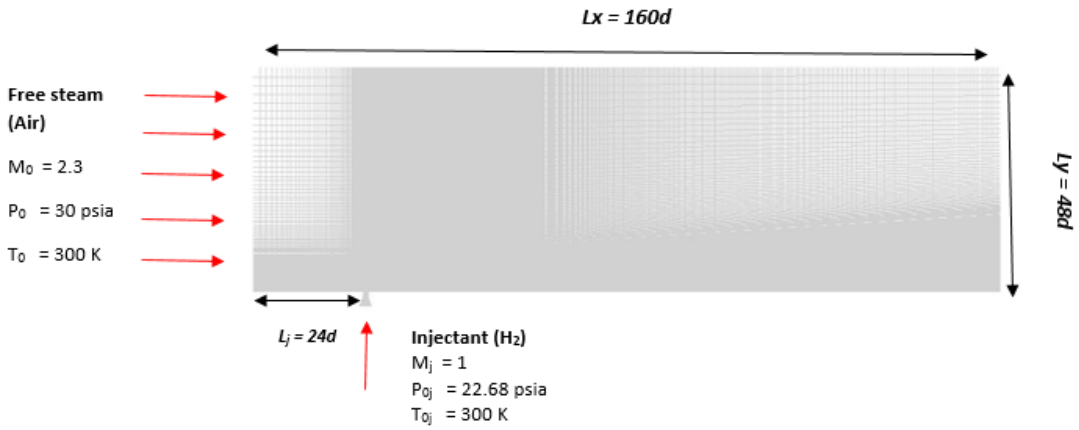


Figure 12: Computational domain and general flow conditions for 2D simulation cases.

Figure 12 shows a generic visual description of the computational domain used in the 2D steady and pulsed injection cases. A 'block' structured 2D grid was constructed to perform the simulations. The domain has the following dimensions: $Lx = 160D$ and $Ly = 48D$ where D is the jet nozzle exit diameter ($D = 0.125$"). The domain length allows for the observation of pulsation features far downstream of the injection location, as well as observation of shocks structures far above the injector surface. The injector was placed 24D units from the leading edge of the computational domain. It was anticipated that transient turbulent effects and boundary layer separation/reflection shocks would occur during injection. Previous simulations showed that the chosen domain length would not affect the outcome of the results [105].

The free stream conditions (Mach number, total pressure etc.) are based on the UTSI Mach 2.3 High Speed Supersonic Wind Tunnel Facility in anticipation of comparing the numerical results of this investigation with future experimentation.

Table 3: Flow Conditions for 2D Simulations

Flow Property	(units)	Free Stream (Air)	Injectant (H_2)
Mach Number	-	2.3	1
Local Pressure	**(psia)**	2.4	12
Total Pressure	**(psia)**	30	22.68
Total Temperature	**(°R)**	540	540

Table 3 shows the flow conditions for the simulations. The injection parameters are dictated primarily by the momentum flux ratio J. From Eq. (1-5) it can be seen in the compressible form that J strongly on injection local pressure P_j.

Since limited penetration benefit exists for supersonic injection [20], injection pressure calculated for sonic injection of hydrogen ($\gamma_{H_2} = 1.41, P_{tj}/P_j = 1.898$) This dictates the total pressure of the injectant. The injectant conditions were calculated based on the values of injection static pressure which produces a momentum flux ratio close to ($J \approx 1$). The actual value of J was re-calculated and found to be $J = 0.95$. Since cold-flow injection was assumed, the flow conditions and numerical model does not account for combustion or heating effects.

The pulsed injection cases apply Eq. (3-2) to the injector inlet. The ratio of the pulsation amplitude to the mean pressure is ($P_{tA}/P_{tj} \approx 1$) so that the instantaneous momentum flux ratio $J(t)$ varies from approximately 0 to 2 with the cycle averaged value approaching unity ($J_{cycle} \approx 1$). The value of J_{cycle} is based on solving Eq. (3-2) using the cycle averaged injection local pressure $P_{j_{cycle}}$.

A grid study was done to verify that the 2D simulation results were independent of grid density. The grid densities, a course grid (65,000 cells), medium grid (120,000 cells) and fine grid (450,000 cells) was constructed using ANSYS Design Modeler. The choice of cell count for the grids was based similar

Table 4: Simulation Test Matrix for 2D simulation cases

Case	Jet Condition	Grid Size	Frequency
Baseline	Steady	120k	-
1	Pulsed	120k	8kHz
2	Pulsed	65k	16kHz
3	Pulsed	120k	16kHz
4	Pulsed	450k	16kHz
5	Pulsed	120k	24kHz
6	Pulsed	120k	32kHz
7	Pulsed	120k	48kHz

2D studies of scramjet flow paths and JISF/PJISF including Koichi *et al.*, Karl *et al.* [106] and Huang *et al.* [107]. Huang *et al.* simulated a hydrogen/air JISF on a 2D baseline grid of 115,000 cells, with grid independence demonstrated on a course grid (57,400 cells) and a fine grid (171,000) cells [107]. The 2D grids in this study are constructed identically; all three concentrate grid points near the injector walls with a cell biases of 15 and 10 on cells near the injector and boundary layer respectively. The smallest cell size for the medium grid is ($\Delta y = 10^{-2''}$) which corresponds to a dimensionless wall unit of $y^+ = 30$.

Table 4 reveals the set of simulations performed on the 2D grid. Both steady injection and pulsed injection cases are shown including the cases 3 – 5 which represent the grid study (course, medium and fine grids pulsed at 16 kHz). The pulsed cases all used the shifted sinusoidal pulsing function shown in Eq. (3-2). The frequency in Eq. (3-2) was set in the user defined function (UDF) to the values of 8, 16, 24, 32 and 48 for the case of interest. Pulsation injection amplitude ratios and cycle averaged momentum flux ratios are set to the same values for all frequencies investigated: ($P_{tA}/P_{tj} \approx 1$) and ($J_{cycle} \approx 1$).

3.2.2 Numerical Methodology and Procedure

The finite volume commercial solver ANSYS FLUENT R15 was used for all of the 2D simulations. The computational domain was constructed in AutoCAD 2014 and subsequently imported and meshed in ANSYS Design Modeler and ANSYS Mesh. This procedure was done for the course, medium and fine grid sizes.

The two dimensional Navier-Stokes equations (x, y-momentum, energy) and species equations are solved using a Density Based Coupled Solver (DBCS). Turbulence is simulated using the transient Delayed Eddy Simulation (DES) setting, with the sub-grid scale turbulence modelled using the Menter SST k-ω formulation. A Roe-type scheme is used to calculate the flux across the cells in the domain.

The model uses second order implicit upwinding in space and order first order implicit time discretization. Initially second order explicit time discretization was used; this was found to produce the same qualitative results as first order but was numerically unstable. For stability, all cases presented here are first order implicit in time. A node based gradient reconstruction approach was used for higher order spatial accuracy.

Boundary conditions include a pressure inlet for injection, a no-slip wall condition for the wall (lower boundary surface including the injector walls), pressure-far-field for the domain left and top faces and a non-reflecting pressure outlet condition for the far right face. This condition simply extrapolates the flow from the interior onto the back wall surface. ANSYS FLUENT has boundary condition settings which include pressure inlet and mass flow inlet. The ANSYS FLUENT R15 Theory Guide recommends the pressure inlet setting for compressible flow problems [94]. This setting is used for steady and pulsed cases. Constant values (e.g. P_{tj}) are entered directly for the steady injection case. For the simulations of pulsed injection, a user-defined function (UDF) program was

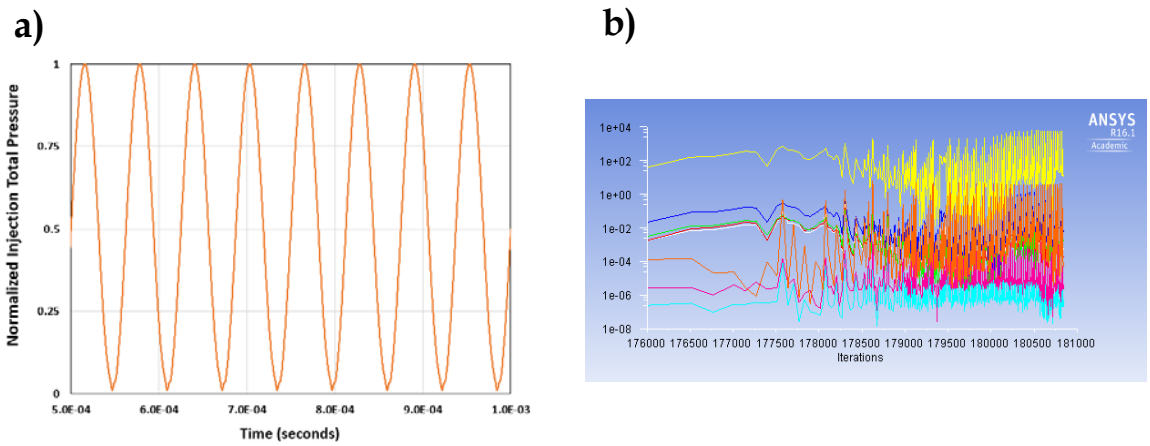


Figure 13: 2D Simulation data: (a) instantaneous pulsed injection total pressure from time 0.1 to 1 *ms*, (b) plot of the residuals for 2D pulsed injection simulation between 170,000 and 180,000 iterations. Both plots are from the medium grid (*f* = 16 kHz) case.

written and imported into FLUENT to model the sinusoidal variation of total pressure over time going into the injector inlet using Eq. (3-2). A sample of the injection total pressure output (normalized by the peak total pressure (P_{tj_P}) can be seen in in Figure 13a. Initially, the simulations were run without jet injection from the wall. This allowed the boundary layer to develop along the wall prior to injection. Once the mass flow rate became stable and the simulations reached convergence the transient models were initiated.

All transient simulations used an implicit Courant number of 5 (default in FLUENT). Time steps of $0.1\mu s$ seconds were used. During each time step, 20-25 iterations were required to reach convergence. Convergence was defined when all residuals reached an error of approximately 1e-4 (Figure 13b). Each simulation was run for *at least* 1 *ms*, allowing the injected flow to leave the domain prior to the sampling of time averaged statistics. This allowed for 175 flow through times to pass prior to time sampling. Here, flow through time is defined as the jet diameter ($D = 0.125$") divided by the crossflow velocity ($U_c = 556\ m/s$). The runs were run additional time steps for averaging. Averaging was done over 5000 time steps (1 *ms*) for all cases.

3.2.3 Grid Independence Study (16 kHz Forced Case)

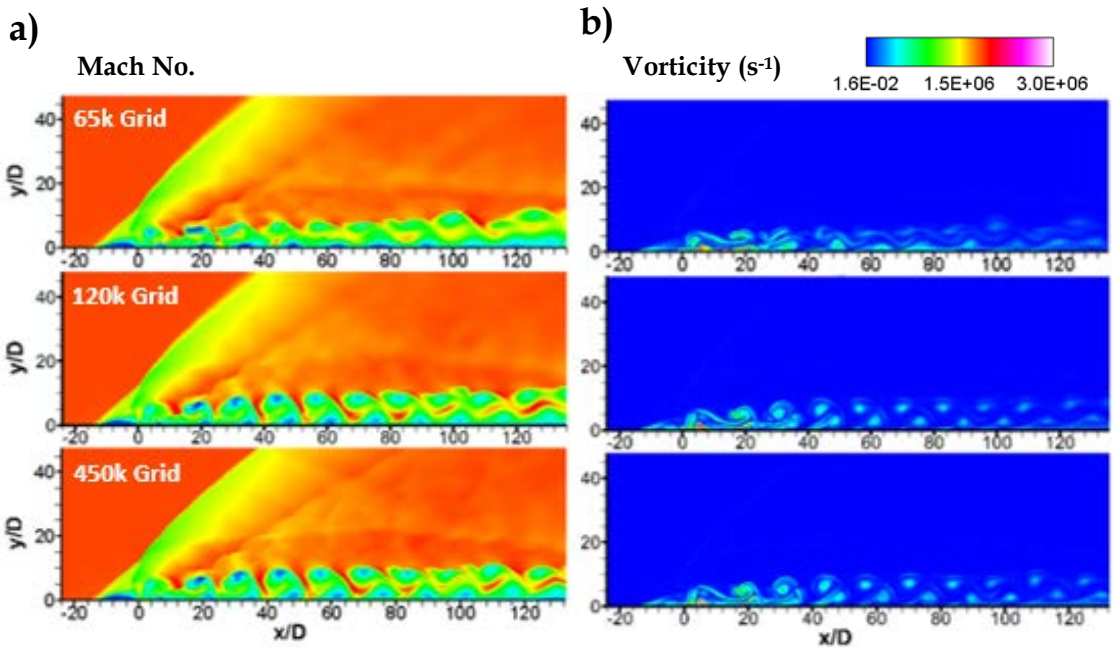


Figure 14: Results of grid independence study (*t = 1 ms*, *f = 16 kHz*): (a) Mach number contours and (b) vorticity contours are from the course (65k), medium (120k) and fine (450k) grids.

Figure 14 shows results from the grid independence study (Cases 2-4, pulsed at a frequency of 16 kHz) which reveal contours of Mach number and vorticity at the same instant in time after initiation of injector flow (approximately 1 *ms*). The cases shown in Figure 14 were run under identical flow conditions (including free stream and pulsed injection waveform boundary conditions) on the course (65,000), medium (120,000) and fine (450,000 cells) grids. Exactly 16 full pulsation cycles have passed at the instant in time displayed in Figure 14 (1 cycle at 16 kHz is 62.5 μsec); the initial stroke and starting vortex has fully been forced out of the domain. The Mach number contours in Figure 14a reveal that pulsation of the jet in a supersonic crossflow also creates a bow shock upstream of the injection location similar to steady jet injection. However, after each pulse stroke, an eddy-like large scale structure (generically referred to as a fluid slug in literature [65], [54]) is emitted into the crossflow. As a result of subsequent pulse strokes, the

primary bow shock exhibits wave-like disturbances which travel along the length of the bow shock. Each fluid slug also carries its own disturbance which expands radially as the slug itself is pushed downstream by the crossflow. Also, as each fluid slug is convected downstream of the injector, a cresting and vortex roll-up phenomena is visible. Figure 14b shows after each pulse, concentrated regions of vorticity are present in the fluid slugs. The course grid exhibits smearing of the vortical structures especially in the jet far field ($x/D > 20$), but the medium and fine grids show that the vorticity concentration regions retain some of their resolution.

Figure 15 shows plots of time averaged mass concentration profiles ($\bar{Y}_{H_2}$) sampled for all three grid densities at locations (x/D) of 0, 10, and 20. From the data in Figure 15 all the grids produced generally the same shapes. At the injector location ($x/D = 0$) the profiles are nearly identical, with the course grid slightly over predicting the penetration (defined in Sec. 3.1) of hydrogen mass fraction $\bar{Y}_{H_2}$.

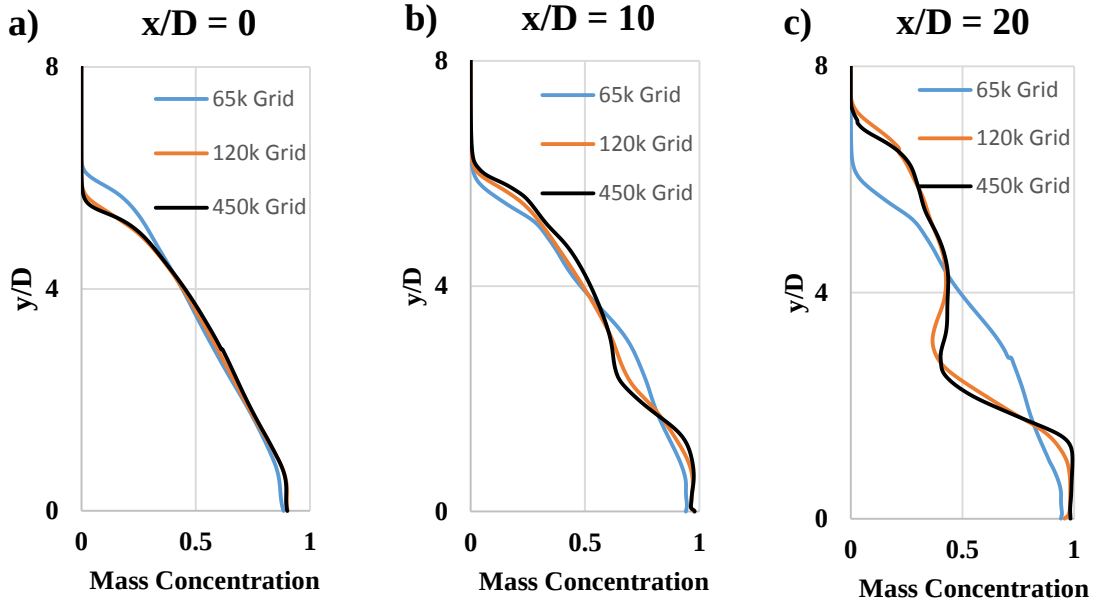


Figure 15: Comparison of time averaged mass concentration profiles for the course, medium and fine grids. Mean mass concentration of hydrogen is sampled at domain locations (a) *x/D = 0*, (b) *x/D = 10* and (c) *x/D = 20*.

In the near field ($x/D < 20$) the profiles collapse onto each other and produce the same generic shape. The medium and fine grids reveal a saddle point between the lower and higher species max values. This is not shown in the course grid at that location. The far field grids ($x/D \geq 20$) reveal a growth in the saddle region on the medium and fine grids. At ($x/D = 20$) the saddle region suggest that the time averaged distribution of pulsed injectant is both concentrated mass near the wall and is also spread vertically in the form of large scale vortical structures which roll up and entrain cross stream fluid as the individual fluid slugs are convected downstream of the injector. This can be seen in the Mach number and vorticity contours in Figure 14a-b. Since the medium and finest grids showed reasonable agreement, the remainder of the cases were run on the medium grid.

3.3 2D Simulation Results

3.3.1 Pulsed Injection Characteristics at Various Frequencies

The following section includes simulation results comparing jet penetration characteristics between the steady injection, and sinusoidal pulsed injection at frequencies of 8, 16, 32 and 48 kHz. Justification of this range of frequencies can be found in Sec. 3.1. Cases 1, 3 and 4 – 7 (see Table 4) were simulated on the medium grid (120,000 cells). The same free stream conditions were used for all cases (see Table 3) and constant injection boundary conditions were used for the steady injection case (Case 1). A UDF program was used as a boundary condition for the pulsed injection cases (Case 2 and 4-7). The UDF program applies the sinusoidal pulse function (Eq. (3-2)) to the pressure inlet boundary to inject the proper frequency for the appropriate case.

Figure 16 shows contours of Mach number (left) and mass concentration (right) all imaged at the same time step after jet flow injection ($t = 1.344\ ms$). This equates to approximately 22 pulsed cycles. The simulations presented in Figure 16

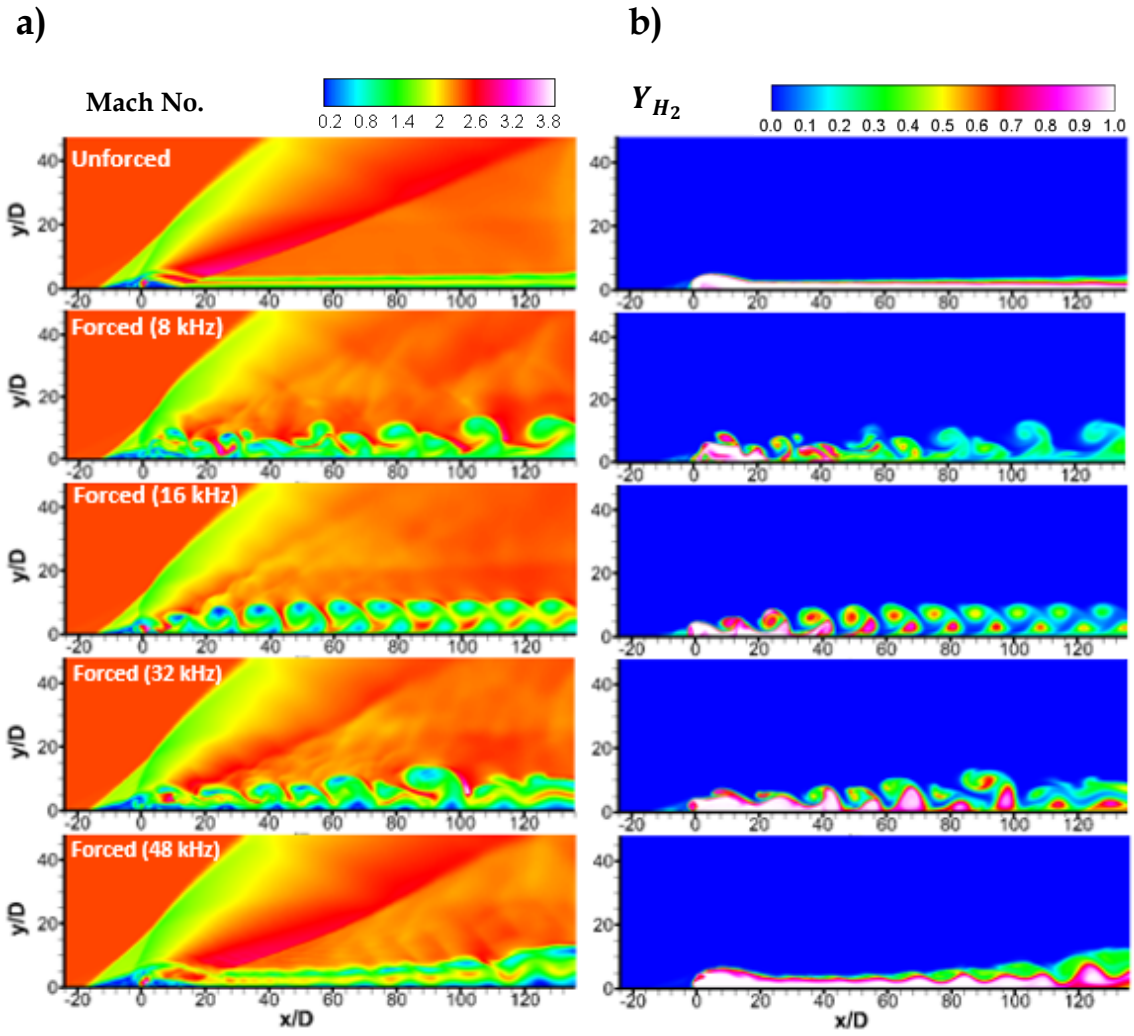


Figure 16: Comparison of steady and pulsed injection flow fields at frequencies (*f* = 8, 16, 32 and 48 kHz): (a) Mach number contours and (b) mass concentration contours. All images are displayed at the same instant in time (*t* = *1.344 ms*).

suggest that sinusoidal pulsation both improves jet penetration in comparison to steady injection and also that the choice of excitation frequency drastically affects both the jet penetration characteristics and structural characteristics downstream of the injection cite. It can be seen in Figure 16a-b that the steady jet trajectory stays near the wall, which is characteristic of low momentum flux jets. Pulsation at 8 kHz, produces large fluid slugs, which exhibit irregular turbulent vortical structures which roll up periodically. In the near field ($x/D < 20$) consecutive pulses produce chaotic and somewhat scrambled vortical structures.

Penetration is deepest in the near field at 8 kHz, but the chaotic phenomena impedes with the penetration downstream. Increasing the pulsed frequency to 16 kHz reduces the spacing of each vortex eddy, but also changes the structure of each fluid slug from irregular to crest-like. The penetration is somewhat similar in the near field but improves in the far field ($x/D > 20$). In the far field, at 16 kHz the eddy roll up of each fluid slug improve the mass concentration of injectant. The mass concentration contour in Figure 16b show a sequence of rotating vortex pairs, one with weaker concentration of injectant which penetrated deeper followed by a stronger mass concertation which remains near the wall.

When the frequency is further increased to 32 kHz, the spacing between each fluid slug is reduced even further. Subsequent fluid slugs begin to interact with each other. Increasing the frequency of pulsation produces more fluid slugs; due to the vortex roll up of a given slug, fluid is entrained away from the new, rising slug which impedes the amount of mass and momentum associated with penetration is reduced.

When the frequency is increased to 48 kHz, the near field shows behavior somewhat similar to steady injection. Each stroke produces a fluid slug in such rapid succession that vortex roll up which induces velocity and momentum is impeded by the presence of the next pulse structure. Eventually, the successive fluid slugs coalesce along the wall producing steady jet behavior.

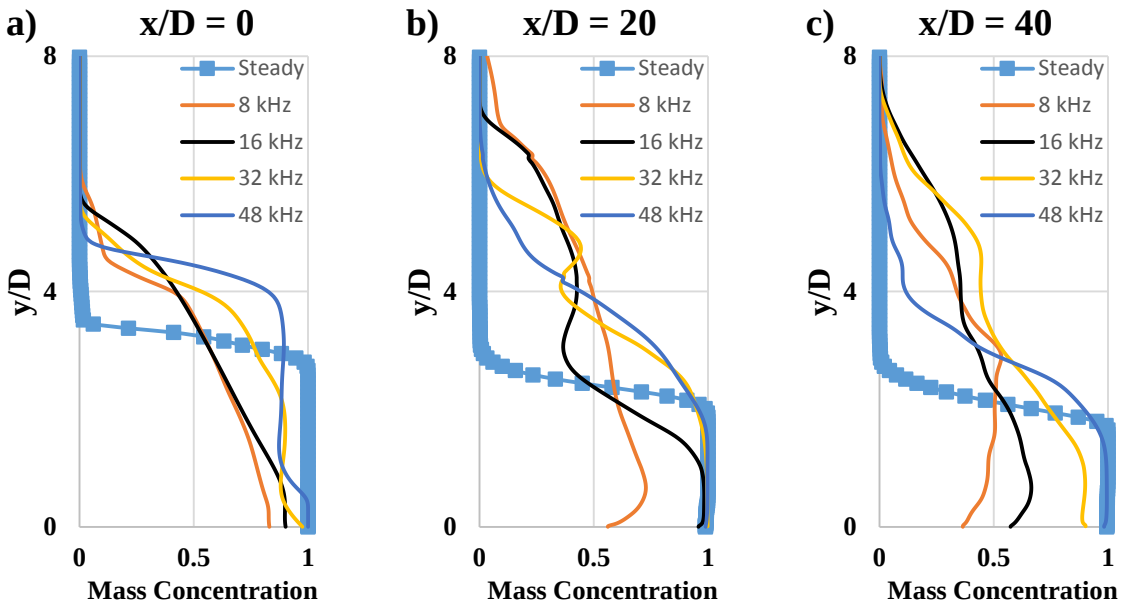


Figure 17: Time averaged mass concentration profiles of hydrogen for steady and pulsed jets (*f* = 8, 16, 32 and 48 kHz): (a) location *x/D = 0*, (b) location *x/D = 20* and (c) location *x/D = 40*.

Figure 17 shows line-rake profiles of time averaged mass concentration ($\bar{Y}_{H_2}$) at locations (x/D) of 0, 20, and 40. Higher values of mass concentration in the direction height direction (y/D) indicate increased jet penetration. The mass concentration profiles in Figure 17a show that pulsation at all frequencies improve the mass concentration height as measured from the wall ($y/D = 0$) in comparison to the steady jet. Pulsation at 8 and 16 kHz show the most improvement at ($x/D = 0$). This trend is consistent with the visual evidence from Figure 16b which shows that the largest eddies associated with pulsation are produced in the near field at 8 and 16 kHz, suggesting the impact of the pulsation frequency vortex formation and penetration. At ($x/D = 20$) pulsation at 8 and 16 kHz improves penetration substantially over steady injection and pulsation at the higher frequencies (Figure 19b). Penetration improvement weakened when pulsing at 8 kHz in the far field ($x/D = 0$) (Figure 17c). Interestingly, the penetration at 16 kHz is consistently strong in comparison to steady injection and pulsation at the other frequencies even at ($x/D = 40$). The spacing between each pulse at 16 kHz allows

the fluid slug to entrain more fluid and grow without the impedance of subsequent structures. The results seen in Figure 16 and Figure 17 suggest that pulsation at 16 kHz most consistently improves penetration in the near field and far field when compared to the higher and lower frequencies investigated.

3.3.2 Time Evolution Characteristics of Pulsed Injection

Figure 18 shows the behavior of the flow field immediately surrounding the nozzle injector over a single pulse cycle after 22 pulsation cycle have been run. Here the start of a pulse cycle is defined as when the injector total pressure is at a minimum, the peak pressure is the highest value of total pressure and so forth. The plots in Figure 18 show the variation of injection pressure through a full stroke, with the arrows indicating the part of the cycle currently being viewed in the contour plots (Figure 18a-e). Each diagram shows the pulsed jet associated with different times within a given cycle. The time of the cycle is denoted by fraction of a cycle (t/T). The cycle fraction (t/T) varies from ($t/T = 0$) at the start of a pulse stroke to ($t/T = 1$).

When $t/T = 0$, at any time after the first injection cycle there is fluid mass from the previous stroke still being convected downstream. At a quarter stroke of the cycle ($t/T = 0.25$) a slug of fluid is beginning to emerge from the nozzle exit plane. The fluid in the jet at the nozzle exit is choked and thus remains sonic (Figure 18b). However, since the jet is under-expanded, the jet becomes supersonic beyond the injector exit area; a small barrel shock-let begins to form and is pushed downstream of the nozzle exit. Also, the weakened bow shock from the previous pulse is pushed downstream of the injector exit plane. At half stroke ($t/T = 0.5$) the bow shock has fully emerged and penetrates to a height deeper than it would during a steady injection of the same cycle averaged injectant pressure. The reflection shock, boundary layer separation region and a recirculation zone is

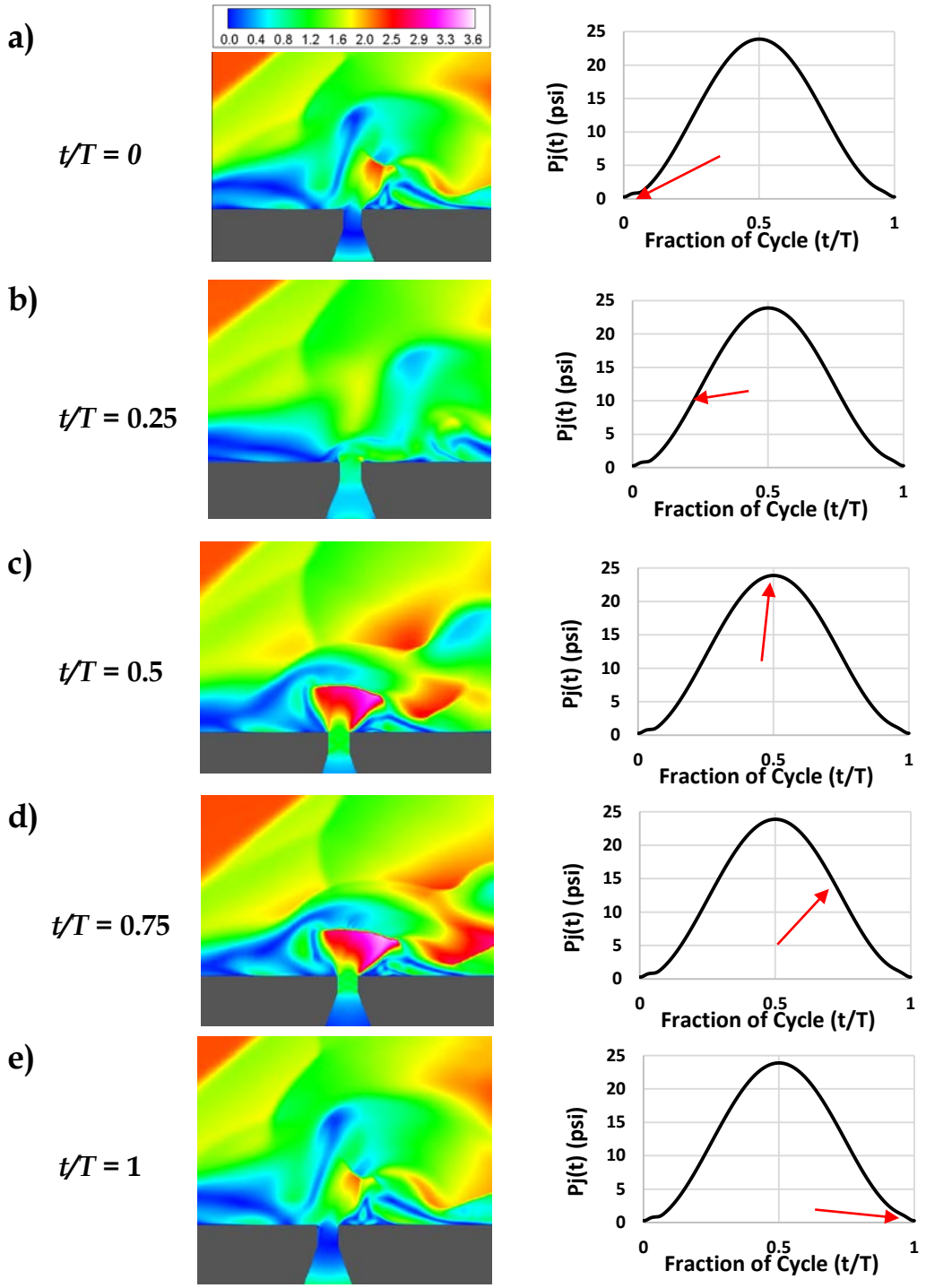


Figure 18: Time evolution of pulsed fuel jet in supersonic crossflow at 16 kHz: (a) prior to injection of current cycle (*t/T* =0), (b) at a quarter of a cycle (*t/T* = 0.25), (b) peak injection pressure (*t/T* = 0.5), at three quarters of a cycle (*t/T* = 0.75) and at the start of a new cycle (*t/T* = 1). Contours are of Mach number.

fully formed upstream of the injector. The flow has somewhat similar physical behavior at this instant in time to an unforced injection, except that the penetration is deeper.

At three-quarters of a stroke $(t/T = 0.75)$ the Mach disk/barrel shock becomes weaker and begins to dissolve. The fluid which was forced through the nozzle for the first three quarters of the stroke begins to roll up into a large scale turbulent mass with concentrated vorticity. It becomes larger as it is convected downstream of the injection site. By the full stroke, $(t/T = 1)$ the flow field resembles that condition at the beginning of a stroke.

Figure 19c shows mass concentration contours of the pulsed jet evolution over a full cycle. The emerging jet produces a roll up region immediately upstream of the windward facing side of the slug. This roll up region becomes larger as the jet is convected downstream, due to more fluid being entrained. As the roll-up region grows, increased vorticity (see Figure 14b) induces an up-wards velocity which forces the slug upwards into the flow, while the crossflow pushes it downstream.

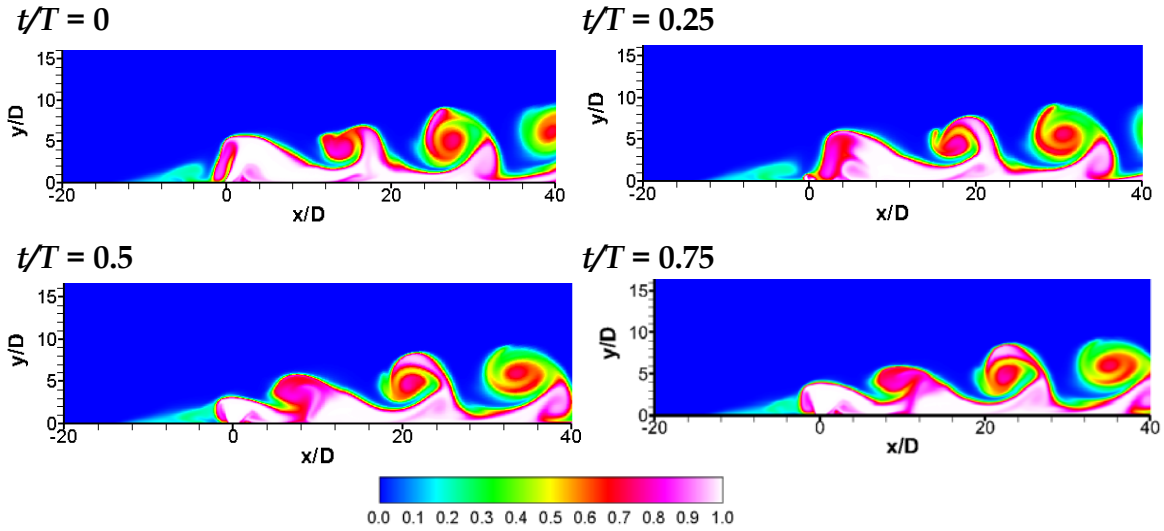


Figure 19: Mass concentration contours showing the large scale eddy rollup of the pulsed jet over one cycle (*f* = 16 kHz) at times (t/T = 0, 0.25, 0.5 and *0.75*).

High mixing regions are concentrated near the center of each vortex eddy. Fluid from the next vortex is pulled into the growing vortex core. Thus mixing and penetration of the pulsed jet is improved over the steady jet.

3.4 2-D Simulation Results Summary

At the start of this chapter the stated goal of producing 2D simulations of pulsed fuel injection into supersonic crossflows which investigate the effect of pulse frequency on penetration behavior was articulated. It was shown that sinusoidal pulses in which the cycle averaged injection pressure matched the steady injection pressure (and by implication, the cycle averaged momentum flux ratio and mass flow rates) improve the overall penetration and mixing characteristics at all frequencies chosen.

The 2D models reveal the frequency range which maximizes penetration over the widest range of get regions when observed statistically over time. Since the 16 kHz cases showed the most promise it was decided to study the specific pulsation conditions of 16 kHz in the 3D models. It is well known that gaseous injection into a supersonic crossflow is a highly three dimensional phenomena. Furthermore, the lack of extensive literature on detailed turbulent descriptions and predictions of pulsed injection into supersonic crossflows dictate the need for a detailed 3D model. However, due to limitations on computational resources a select set of flow conditions can be studied in the desired detail. The next chapters (4, 5 and 6) explain the models, methods and results of 3D simulations of pulsed injection into a supersonic crossflow.

4 Primary Investigations (3D Studies)

4.1 Primary Investigation Overview

The stated goal of this study as was stated in Sec. 3.1 was to address the limitations in available experimental and numerical research studies of pulsed injection into supersonic crossflows. Numerical research investigations are limited to 2D URANS models but none have investigated PJISF using scale-resolving (SRS) models. Lack of access to experimental facilities further guided the focus of this study to investigate PJISF using numerical techniques (2D and 3D models CFD models). Further specification of the scope included a focus on low momentum flux ratio injection ($J \leq 1$) and pulsation frequency ranges ($8 < f < 48$ kHz).

Justification of the choice of injection and flow conditions (including injection pressures and pulsation wave form) are discussed in Sec. 3.1 but are supported in literature (see Ref. [102], [39], [54], [60]). The generic approach taken in this study is based on a comparison between a steady JISF and pulsed jet in which the steady jet momentum flux ratio and total pressure (P_{tj}, J) is equivalent to a pulse cycle averaged momentum flux ratio and total pressure ($P_{tj_{cycle}}, J_{cycle}$) for a means of direct comparison of the effects of pulsation on jet penetration. Computational resource limitations guided the direction of this study to focus on exploring the range of frequencies in 2D simulations to down select a specific pulsation frequency on which to focus the 3D simulation.

Chapter 3 focused on the investigation of sinusoidal pulsation (in 2D) at 8, 16, 32 and 48 kHz to span the range of frequencies investigated by Kouchi *et al*. Mass concentration profile samples of $\bar{Y}_{H_2}$ were taken at dimensionless locations $x/D = 0, 20$ and 40 which showed that pulsation at 16 kHz improved penetration (highest mass concentration height, y/D as measured from the wall) both in the near field and far field in comparison to steady injection among the frequencies sampled. A grid study demonstrated independence of mass concentration profiles for the medium and fine grids.

The specific scientific contribution of this study is a 3D investigation of pulsed injection into supersonic crossflow using an SRS modeling approach. Several studies have employed SRS techniques to JISF (e.g. [102], [108], [109]) but as far as is known, none have applied an SRS method to study PJISF injection. Thus, a comparison of the effects of jet penetration, mixing and total pressure loss performance between a steady jet and a sinusoidal pulsed jet ($f = 16\ kHz$) using a wall-modelled Large Eddy Simulation (WMLES) is presented in this study. The flow conditions, grid construction, numerical approaches used in this study are discussed Sec. 4.2

Two computational grids (10 and 17.8 million cells) are constructed to establish the independence of grid density on results. Justification of the model choice and grid specifications is discussed in subsequent sections. The remainder of Chapter 4 focuses on the baseline case (steady injection, $J \approx 1$) and includes a validation of the grid against 1D compressible flow theory and Mach disk/separation shock theory as well as verification of grid independence between the 10 and 17.8M grids. This study does not focus extensively modeling effects (e.g. comparison of model turbulence effects or choice of SRS model) but primarily serves as a means of investigating steady JISF and PJISF performance at similar forcing conditions.

4.2 Problem Set up and physical model

4.2.1 Computational Domain and Case Setup

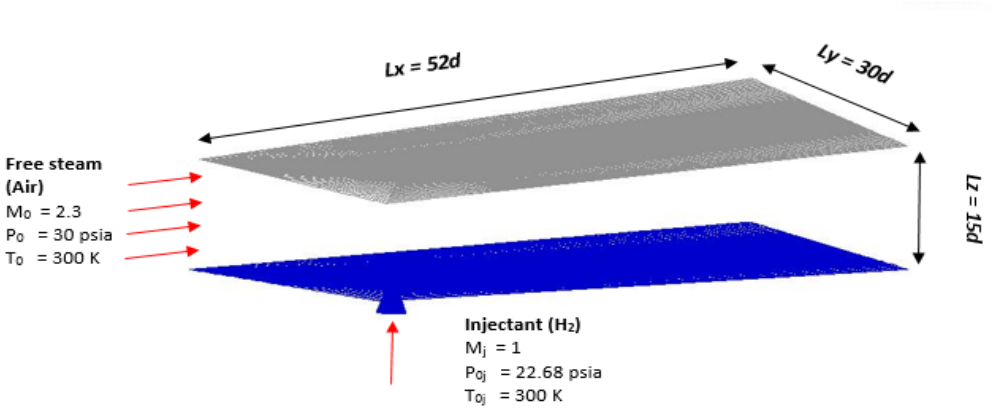


Figure 20: Computational domain and flow conditions for the 3D numerical investigations.

Figure 20 reveals the computational domain used in the subsequent investigations. The same domain is used both for the steady injection (baseline) and pulsed cases. The domain size has length units (Lx, Ly, and Lz) of 52D x 15D x 30D in the length, wall normal and lateral directions. The domain is scaled with the injector nozzle exit diameter ($D = 0.125$"). The center of the nozzle inlet is placed exactly 12D units from the domain edge. Previous experience [105] and similar studies in literature (e.g. Kawai and Lele [74] and Watanabe *et al.* [109]) showed that in similar JISF models, placing the injector between 5D and 18D from the domain entrance obviates turbulent fluctuations and physical reflections of those fluctuations near the domain boundaries. Thus these effects (if present) will not affect the behavior of the region of interest.

The placement of the injector length also allows for a domain length of 40D to allow observation of the far field ($x/D > 20$) especially for the pulsed injection case. From the results of the preliminary 2D investigation it is suggested that sinusoidal pulsation at 16 kHz allows for nearly four full pulsation cycles (4 fluid

slugs) to become injected through the nozzle inlet before the first slug passes reaches the domain exit plane and leaves the computational domain at $x/D = 52$.

The simulations presented in the 3D investigation use identical cross flow and injection conditions as the 2D steady and pulsed cases (Case 1 and Case 3) seen in Table 3. Table 5 shows a recap of the crossflow conditions and the steady injection conditions used in the baseline case. These conditions are also used in Eq. (1-5) it can be seen that the penetration of a JISF is strongly dependent on the momentum flux ratio, J thus the flow properties (e.g. local pressure) were chosen such that the calculated momentum flux ratio would be close to unity. Justification for this approach can be found in Chapter 3. Table 6 reveals the characteristics of the primary investigation pulsed injection case. The details, and results of the cases will be discussed in subsequent sections. To model pulsed injection Eq. (3-2) was used to simulate sinusoidal injection, for $J_{cycle} \approx 1$, as was done in the 2D cases.

Table 5: Flow Conditions for Baseline Case (*Steady Injection, J ~ 1*)

Flow Property	(units)	Free Stream (Air)	Injectant (H_2)
Mach Number	-	2.3	1
Local Pressure	**(psia)**	2.4	12
Total Pressure	**(psia)**	30	22.68
Total Temperature	**(°R)**	540	540

Table 6: Pulsation Characteristics (*Sinusoidal Injection, 16kHz, J_{cycle} ~1*)

Property	Value
Pulse Pressure Amplitude (psi)	22.68
Local Pulsed Pressure (psi)	22.72
Pulsation Frequency (kHz)	16
Strouhal Number	0.0534
Effective Velocity Ratio (r_{eff})	0.97
Peak Jet Velocity (m/s)	1528
Mean Jet Velocity (m/s)	951

4.2.2 Grid Generation

The computational domain geometry was developed using AutoCAD 2015 to create the domain, and subsequently meshed using ANSYS Mesh. A combined 'Y-type' structured outer grid with a 'C-type' inner grid was constructed, which allows for concentration of grid points near the jet periphery, but was stretched near the extents of the domain in the absence of flow features of interest. The computational domain displayed in Figure 21 shows the block-structured computational grid with hexahedral elements used in this study. Primary focus was given to attempting to balance limited computational resources with meeting LES grid resolution requirements. Several constraints were considered in the construction of the computational domain used in this study. Limited computational resources placed strong limitations on the grid density of the computational domain.

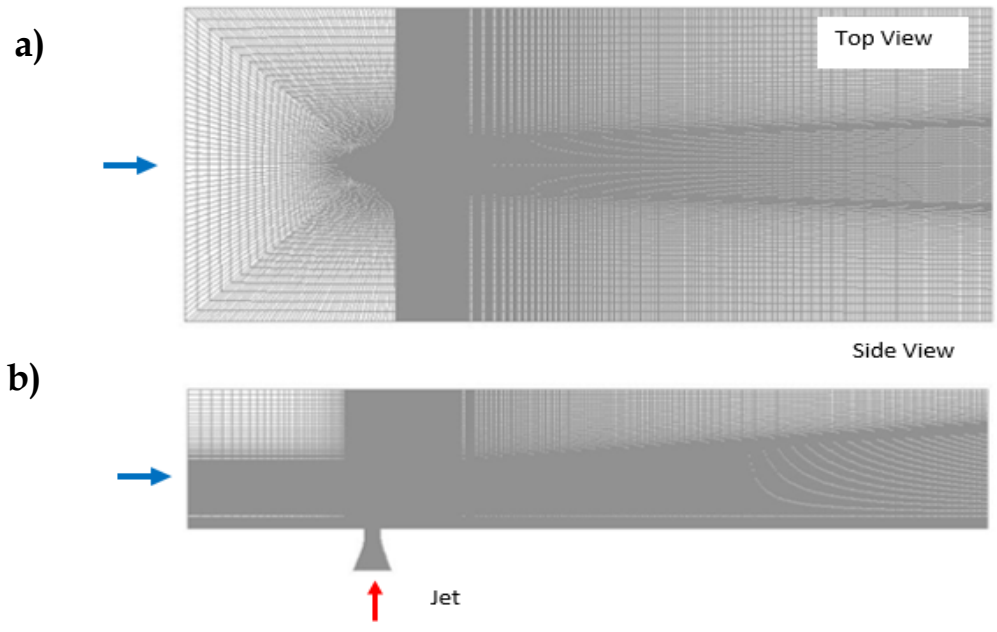


Figure 21: Top view (a) and side view (b) of the block structured computational domain used in this study. Arrows indicate the crossflow direction (blue) and jet injection location (red).

Since resolution of the large scale vortical structures associated with jet pulsation was a primary driver for this study, care was taken in considering grid concentration. Furthermore, it has been shown that hexahedral elements are found to have better flow resolution than tetrahedral elements for the same number of elements [110].

An estimation of the resolution requirements can be made for a given grid based on scaling laws related to the flow Reynolds number (see Eq. (2-15) - (2-17) in Sec. 2.1.3). Table 7 shows a listing of scaling law estimation which are based on the calculated flow Reynolds number ($Re_D = 18{,}400$) using the jet nozzle diameter ($D = 0.125$") a length scale. Kolmogorov scale resolution requires elements which are not practically solved with LES and URANS numerical methods. Instead, grid requirements were based on resolution of the Taylor length scale (especially in areas near the injector) since this is the region where the viscous turbulent effects become most dominant.

Two grids were constructed in this study to demonstrate grid independence: a "small" grid (10 million cells) and a "large" grid (17.8 million cells). The increase in size between the "small" and "large" grids approximately 1.8. The largest grid was designed so that the smallest cell size (Δ) was on the size order of the Taylor

Table 7: Grid Resolution Estimates (Re_D = 18,400, D = 0.125")

Parameter	Value
Kolmogorov Scale (η)	7.912e-5 inches (2.0e-6 m)
Taylor Scale Length Scale (λ_t)	2.87 e-3 inches (7.3e-5 m)
Large Eddy Turnover Time (T_c)	5.7e-6 seconds
Taylor to Kolmogorov Ratio (λ_t/ η)	36.329
Smallest Grid Cell (17.8 M Grid) (Δ)	2.91e-3 inches (7.4e-6 m)
Grid Cell/Taylor Scale Ratio (Δ /λ_t)	1.0139

Scale by concentrating many of the grid points near the injector wall.

Figure 21a shows how the grid points are concentrated closer to the bottom half of the domain (< 8D from the wall) but grow to follow the jet's spread as it is convected downwind of the nozzle. Since this grid is used for pulsed and steady injection, it was anticipated that the pulsed jet would penetrate somewhat deeper than the continuous jet. Thus, the dense region is approximately twice as large as is needed for the steady jet. Several simulations produced preliminary results which suggest the location of the deepest jet penetration.

. Near the nozzle injector, an 'O-type' grid was chosen to allow for easy transition between the curvilinear and rectangular block shapes. Figure 21a shows how the grid cells are stretched from the center (densest region of the grid) to the edges, with primary emphasis placed on the flow region near the nozzle, the region immediately downstream of the injector and the grid regions of the jet and jet far-field regions.

Figure 22 reveals the grid concentrations near the nozzle injection region. The grid spacing is densest in this area of the domain for the sole purpose of resolving the turbulent eddies in the Taylor micro-scale region of the flow. It is thought that in this region, significant vortex production and roll-up phenomena would be the most difficult to result. Thus many grid points were chosen in this region.

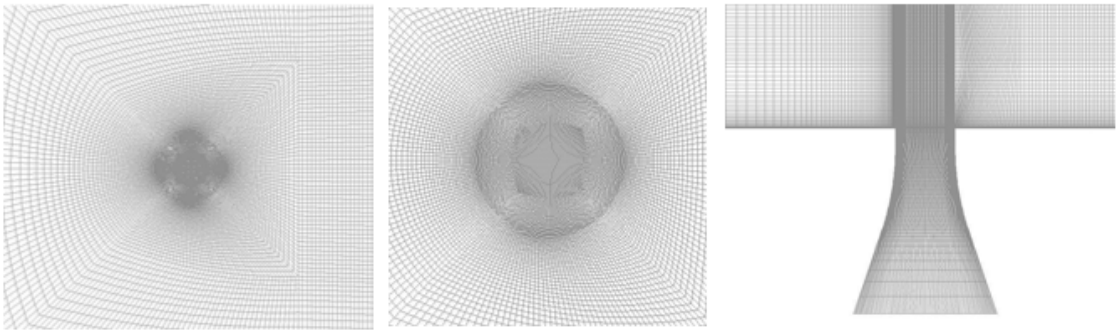


Figure 22: An 'O' type block structured grid with high grid density near the injector nozzle.

4.2.3 Inflow and Boundary Layer Resolution Conditions

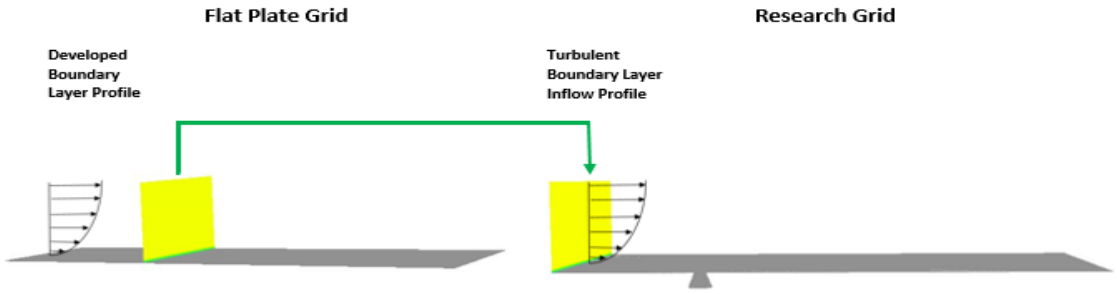


Figure 23: Visualization of the application of a RANS turbulent inflow boundary condition.

In a scramjet engine employing a wall mounted fuel injection system, the flow coming over the injector exit region is highly turbulent. Thus it was necessary to use a turbulent inflow condition for the free stream flow ahead of the injection site. To reduce the grid requirements, the turbulent inflow was simulated in a separate computational domain with a flat plate configuration and identical free-stream properties as that of the research grid. The resulting turbulent boundary layer profile was imported into the research grid. A sketch of the concept can be seen in Figure 23.

It should be noted that many studies of jets in crossflows over flat plates have used unsteady or artificially generated turbulent inflows imported into the research grid from other simulations (e.g. [109], [74], [108], [111], [112]). Generally, it is possible to substantially cut down on grid expense when the turbulent boundary layer is allowed to develop in another a priori simulation and is subsequently imported into the research domain. Typically, the turbulence is generated artificially, by methods such as the hairpin model (which produces random artificial vortical hairpins which add velocity fluctuations to a mean turbulent boundary-layer profile) as is discussed by Peterson and Candler [110]. Other approaches include an inflow generator imported into the research domain [112] and a more complex approach which involves the construction of random

number generated velocity perturbations which satisfy the prescribed energy spectrum and turbulent kinetic energy characteristics based on the Reynolds' stresses [108]. Note that these inflow conditions are produced from separate simulations which involve an SRS technique (an LES or hybrid LES/URANS) and are quite computationally expensive themselves.

A simpler approach to generating inflow conditions is to use a RANS model to allow the boundary layer to develop and extract the profile in the location of interest [113], [114]. In this case the approach was used to extract the profile where the boundary layer to injector diameter approaches unity ($\delta/D \rightarrow 1$). Although it has been shown that unsteady turbulent inflow conditions do affect the jet penetration characteristics, it has been shown for a circular *normal walled injector* inflow effects on penetration and turbulence production are negligible [110] [115]. This justification has been used in this study. Figure 24a-b and shows the simulation results velocity profile results for the inflow conditions from a point in the flat plate domain located near the location of where the boundary layer depth

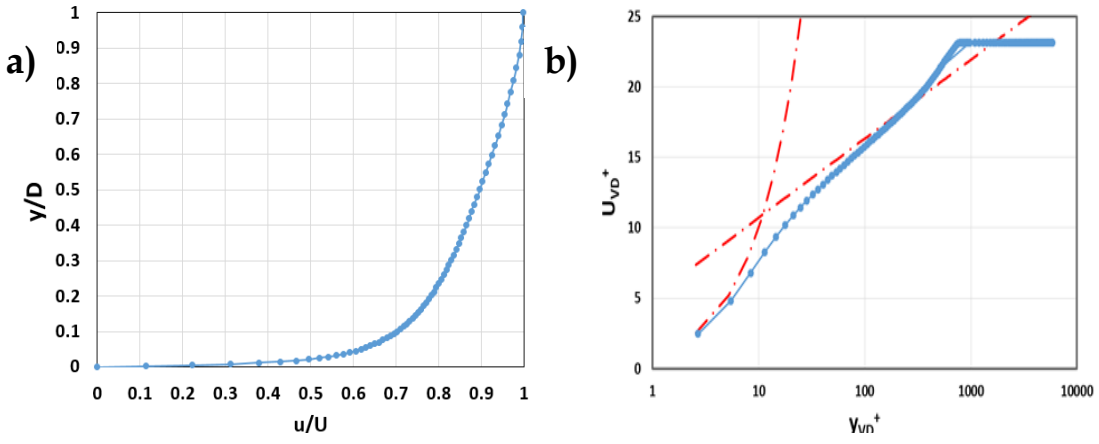


Figure 24: Inflow velocity data at δ=0.125″: (a) Inflow velocity normalized with free stream velocity (U_c = 556 ms^{-1}), (b) Van Driest transformed velocity profile (blue lines) plotted against the log-law and the law of the wall [116].

is the jet injector exit diameter ($\delta = 0.125"$). In Figure 24b it can be seen that Van Driest transformed boundary layer velocity profile scales with the wall $y^+$and thus produces a strong correlation with the theoretical curves for the viscous sub-layer and the law of the wall. The transformation procedure to account for compressibility effects in a turbulent boundary layer can be found in Huang and Coleman [116].

4.2.4 Modeling Approach

4.2.4.1 Computational Resources

The computational resources available for this study include several machines in UTSI's High Speed Computational Resource Center (HIRC). These include a cluster of machines each of which include 256 GB of DDR3 RAM, 4 Intel Xeon e5-4620 CPU's which run at 2.2GHz. Each processor has 16 cores with a total of 64 processor cores per machine. Two sets of machines were used: a pair of nodes running a Linux operating system and a pair of nodes running on a Windows machine. For each of the machines and cases, the ANSYS FLUENT HPC license was used, running double precision accuracy and 32 parallel processes per job scheduler. Each computational grid was partitioned such that a section of the grid was calculated by each processor; thus a total of 32 partitions were used assigning one processor for each partition.

4.2.4.2 Model Description

In this study, the numerical model applied the density based coupled solver (DBCS). A species transport model with the inlet and full multi-component diffusion options selected. The solution methods include an implicit formulation with a Roe-type approximation Riemann solver (as was done in the 2D cases). The spatial discretization scheme included a node-based gradients scheme with second order upwinding. The Algebraic Multi-Grid with the 'F-cycle' and ILU

smoother function was used to improve the CPU performance and cut down the computational time.

Boundary conditions include a no-slip wall condition at the nozzle and domain lower surface, a pressure inlet condition at the nozzle inlet, a non-reflecting pressure outlet condition which extrapolates the conditions in the domain to the outlet wall, and pressure-far-field conditions for the remainder of the boundary faces which represent the extends of the domain. Thus, the steady and pulsed injection simulations represent jet injection from a wall into a semi-infinite supersonic stream. Each simulation consisted of two parts: an initial condition which involves a steady state solution (no injection) with an imported URANS turbulent boundary layer which remains undisturbed and a transient solution in which the jet is 'turned on' and allows flow unsteadiness to develop over time.

4.2.4.3 Initial Steady State Solution

To create an initial boundary condition for the transient simulations, a steady state solution was solved on the same computational grid prior to wall injection. The 2-equation Reynolds' Averaged Navier-Stokes (RANS) k-ω SST turbulence model was used to simulate a developed boundary layer over a flat plate. The turbulent inflow profile was then imported into the computational domain to simulate a turbulent inflow condition. Compressibility effects were also pre-selected in the FLUENT viscous model option. To run the steady state simulation, approximately 4000 iterations (totaling 35 hours running on 32 cores for the 17.8M cell case) were required to reach convergence. Convergence was defined as the point where all of the residuals (e.g. mass, *x*-*y*-*z* momentum, energy) reached an error of ($\varepsilon < 10e^{-5}$), and the domain net mass flux changes were on the order of ($\Delta\dot{m} < 4.5e^{-5}\ kg/s$).

a) b)

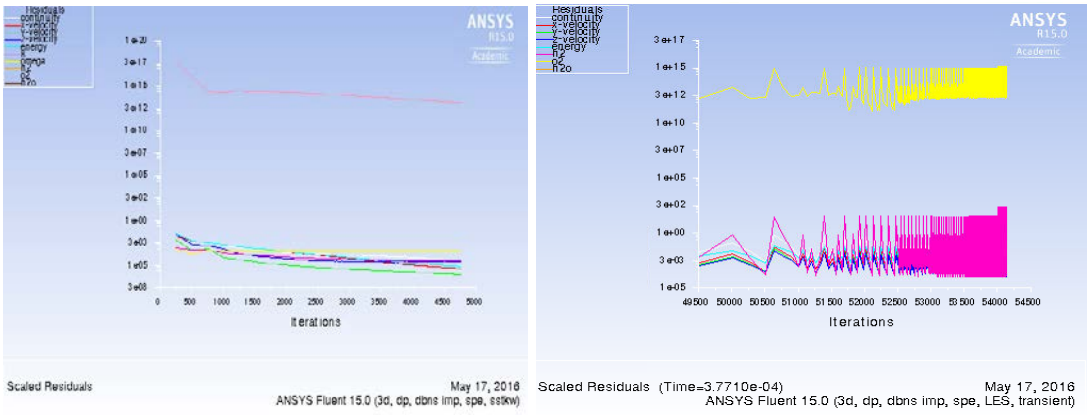


Figure 25: Convergence data from the steady state solution (a) and transient solution (b).

4.2.4.4 Transient Solution

Once convergence was reached (Figure 25a) in the steady state solution, the FLUENT solver settings were switched to transient, with the Large Eddy Simulation setting and the WMLES-S Omega sub-grid scale model turned on. WMLES solutions have been shown to successfully resolve large scale structures in JISF problems where grid economy is important. Examples include Khali and Yao [117] and Peterson and Candler [118]. Khali and Yao [117] simulated a JISF using a WMLES model based on experiment test conditions ($M = 1.6, J = 1$) from Santiago and Dutton [119]. Peterson and Candler [115] used a WMLES approach for a low momentum flux ratio JISF ($J = 1$) on grid sizes of 13.6M and 17.5M cells. Reasonable near and far field LSV resolution was depicted in this study. It was from this justification that WMLES was used in this study.

The WMLES simulation included the following model constraints which are default settings in FLUENT: Energy Prandtl number of ($Pr_e = 0.85$), Wall Prandtl number ($Pr_w = 0.85$) and the Turbulent Schmidt Number ($Sc_t = 0.7$). The use of $Sc_t = 0.7$ was justified from a similar low momentum flux JISF model reported in [120].

The solution applied an implicit spatial method, with a second order upwinding scheme as was used in the 2D simulations (see Sec. 3.2). The transient solution steps was run first order implicit in time.

Furthermore, running second order time created numerical instabilities which often lead to residual increases after the jet fully developed into the computational domain, particularly near the outlet face in the domain. The same flux type and spatial discretization were used in the transient simulation as in the steady state initial solution. A maximum Courant Number of 5 was used, with a maximum time step size of $0.1\mu s$, taking full advantage of the convergence benefits of running an implicit scheme.

The simulations required about 15 iterations per time step for convergence (Figure 25b), with a total of over 40,000 iterations to reach the full run time of 0.3 *ms*. For a pulsed jet pulsing at 16 kHz, this was approximately the length of time in which 4.75 full pulsation cycles occured. Time averaged statistics were taken over 0.3 *ms* during each run. In terms of computational processing time, a simulation with a 17.8M cell grid took approximately 2 minutes per iteration. Several hundred core hours were used to reach the desired flow through time value.

4.3 Baseline Case Results (Steady Injection, *J ~ 1*)

In this section, the results of the baseline simulation (steady injection, *J ~ 1*) are presented. First, demonstration that the computational grids can reasonably resolve the large scale turbulent structures associated with mixing and fluid entrainment is necessary prior to simulation of the PJISF. Furthermore, comparison of the simulation results both with 1D compressible theory and jet penetration correlations are presented. Finally, a comparison between results in the 9.8M and 17.8M cell grids is demonstrated.

4.3.1 Instantaneous Flow Field

Figures 26 and 27 show results from the baseline simulation case. Contours of Mach number in Figure 26 show the salient features of a JISF including the bow shock, barrel shock, Mach disk and the boundary layer separation and recirculation zones. These resolution results compare well with the flow features shown a typical JISF [17]. It can be seen that the large scale strictures quickly roll up, entrain fluid and produce strongly turbulent regions in the flow.

Figure 27 shows an iso-surface of the second invariant of the velocity tensor gradient (Q-criterion), defined as [85]:

$$\boldsymbol{Q} = C\frac{1}{2}(|\boldsymbol{\Omega}| + \overline{\boldsymbol{S}}) = 0 \qquad (4\text{-}1)$$

with constant C = 0.25 (as defined in FLUENT) and absolute value of vorticity ($|\boldsymbol{\Omega}|$) has been used to provide a visualization of the 3D LSV structures simulated in this study. The iso-surfaces have been colored with hydrogen mole fraction (X_{H_2}), with blanking of ($X_{H_2} < 0.1$) to clarify visualization of the jet. The 3D circumferential roll-up structures discussed by Ben-Yakar *et al.* [17] are visible: These are associated with Kelvin-Helmholz instabilities from shear gradients in the flow.

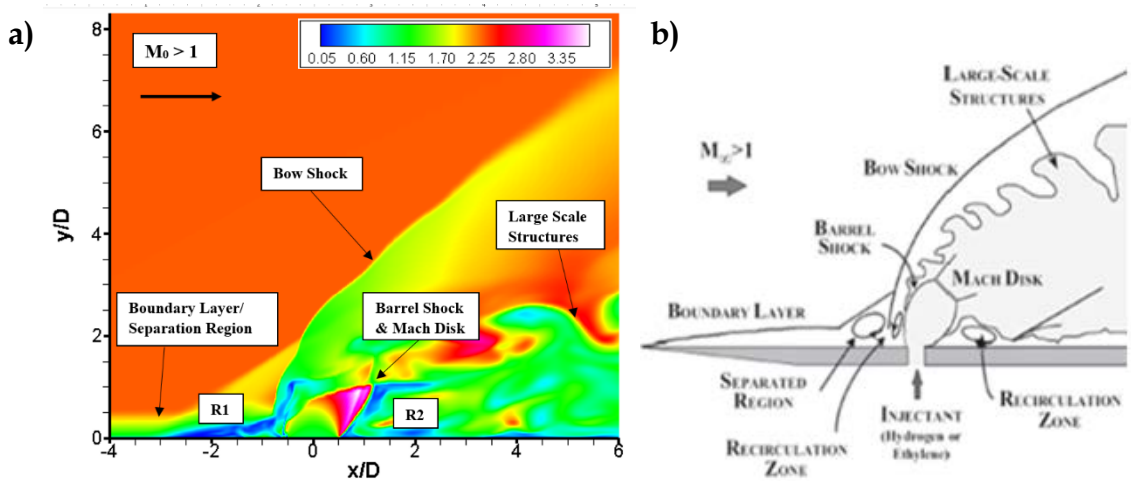


Figure 26: A comparison between the baseline case (Steady injection, *J ~ 1*)(a) and typical features seen in JISF (b) [17]. Contours are of Mach number. Simulation results sampled at time (*t = 0.3 ms*). Reproduced from Ben-Yakar *et al.* [17].

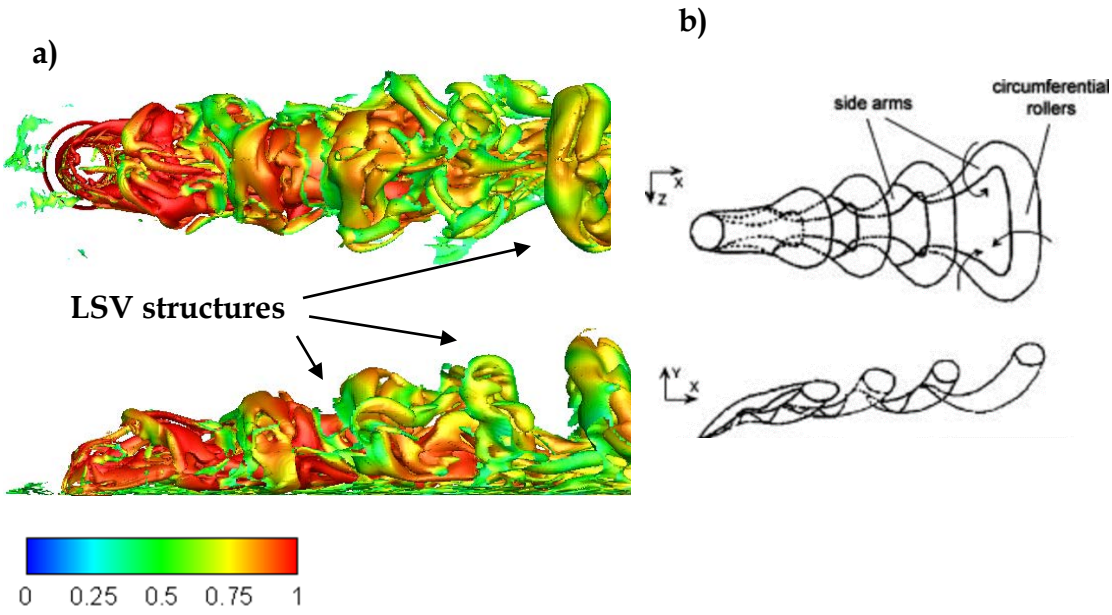


Figure 27: A comparison between the baseline case (Steady injection, *J ~ 1*)(a) and the circumferential roller structures seen in JISF experiments [17]. An iso-surface of Q-criterion (s^{-1}) is colored with hydrogen mole fraction. Image (b) is reproduced from Ben-Yakar *et al.* [17].

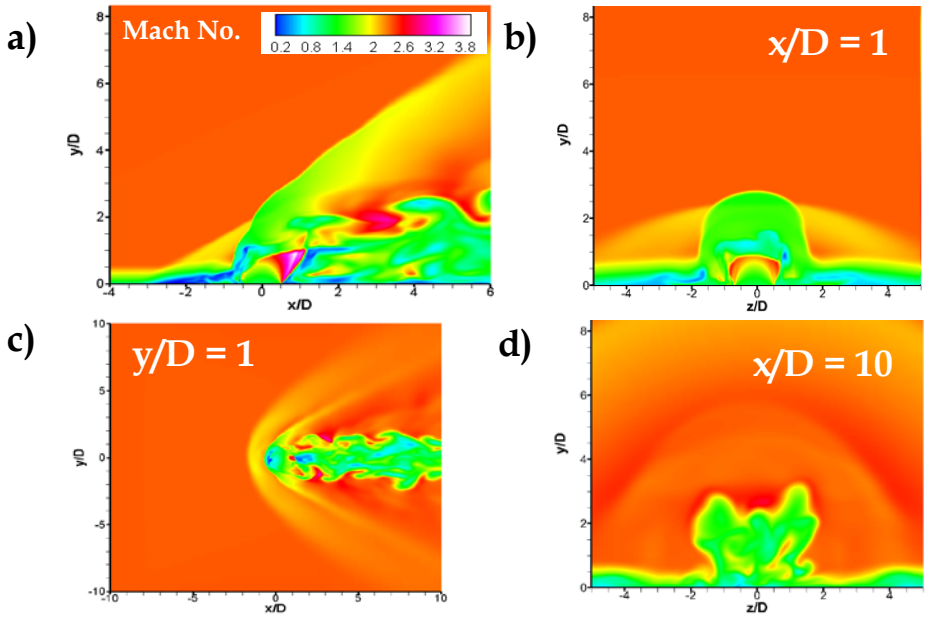


Figure 28: 3D simulation results from baseline case (Steady injection, J ~ 1): (a) Mach number contour of the JISF flow field in the central plane ($x/D < 10$), (b) y-z plane view at $x/D = 1$, (c) x-z plane view ($y/D = 1$) and (d) y-z plane view at $x/D = 10$.

Figure 28 shows planar images of numerically predicted phenomena of the steady JISF. The cross-plane (x-z plane) image at $y/D = 1$ shows the bow shock and reflection shock as well as the near-field regions of the jet including the large scale structures. The y-z plane contours of Mach number show planar cross sections at the wall injector plane, $x/D = 0$ (Figure 28b) and at $x/D = 10$ (Figure 28c). At $x/D = 0$, a slice of the barrel shock produced by the jet expansion shocks emanating from the nozzle is visible, as well as the recirculating fluid from the separated boundary layer on both sides of the barrel shock.

The weaker separation shock is also visible on both sides of the barrel shock, as well as the bow shock; the Mach number immediately above the barrel shock is supersonic, demonstrating that at the height of the barrel shock, the bow shock has oblique behavior at this height. At $x/D = 10$, the counter-rotating vortex pair at an instant in time is visible. The main bow shock is also visible, as well as weak shock-lets produced by CVP.

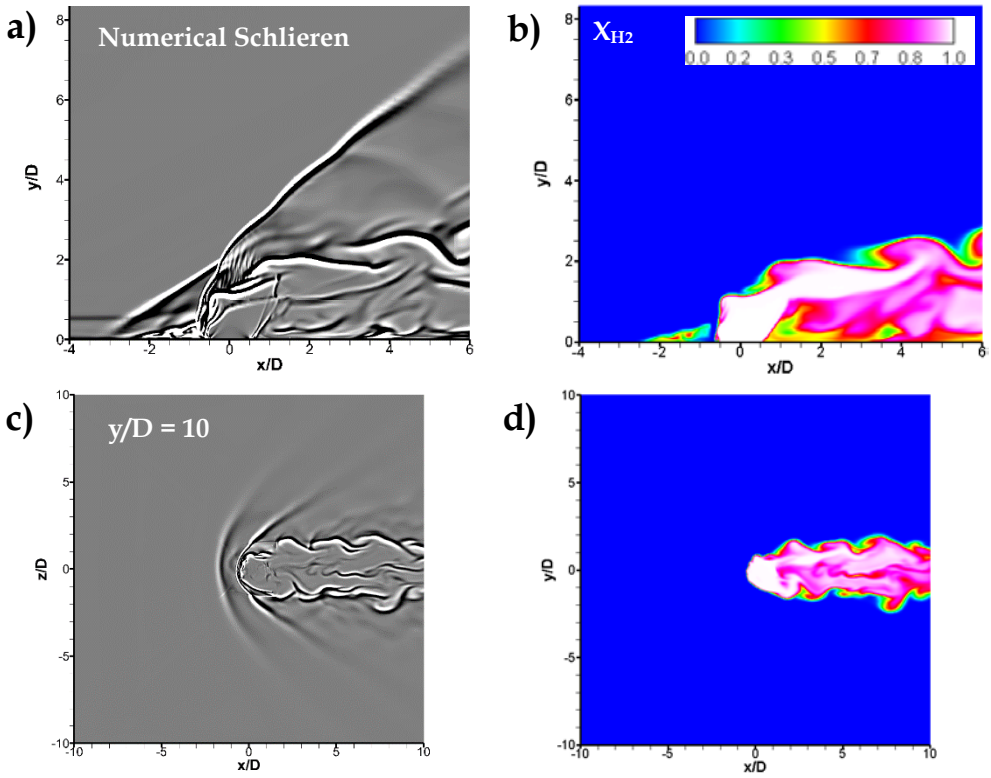


Figure 29: 3D simulation results for baseline case (steady JISF, $J \sim 1$): (a) numerical schlieren image of the central plane ($x/D < 10$), (b) y-z plane view of hydrogen mole fraction at $x/D = 1$, (c) numerical schlieren of the x-z plane view ($y/D = 1$) and (d) mole fraction at $x/D = 10$.

Figure 29 shows baseline case simulation results of numerical schlieren images of the JISF in the central plane (Figure 29a) and the $y/D = 1$ plane (Figure 29c) of the jet/shock structure. Figures 29b and 29d show hydrogen mole fraction in the plane views as the corresponding numerical schlieren images. The same instant in times (t = 0.3 *ms*) are sampled in all images. The potential core and near field region show the development of the large scale eddy structures growing as surrounding fluid is entrained. The numerical schlieren resolves the bow shock and reflections shocks in the near field, as well as the weak shocks produced but the growing eddies. In the far field, the resolution breaks down as the number of grid points is reduced. Outside of the jet region the flow does not impact the solution and thus fewer grid points are required.

The mole fraction contours (Figure 29b) are a measure of the mixing region upstream of the injection site as well as the mixing zones in the potential core region as the jet begins to bifurcate and develop into a pair of counter-rotating vortices. The results attained in this study demonstrate qualitatively the stated goal of concentrating the grid points (with limited computational resources) to resolve the large scale structures especially in the vicinity of the injector and the barrel shocks. Demonstration of large scale resolution is tantamount to the successful observation and understand of how pulsation jet injection affects the typical vortical structures, shock interactions as well as global mixing and penetration effects in comparison to unforced jet injection.

4.3.2 Time Averaged Flow Field

Statistical sampling of the transient numerical solutions were performed after the flow developed. Time averaged samples were taken for approximately 0.3 ms (over 4.75 full pulse cycles). Figure 30 reveals time averaged images of static pressure, root mean squared (RMS) mass concentration fluctuation, and mass concentration in the constant-y plane and constant-z plane. The time averaged static pressure shows the strongest shock resolution in the near field ($y/D < 4$). Immediately downstream of the injection site, the drastic drop off in pressure corresponds to the location of the barrel shock.

These regions are where the pressure losses are most severe; the strength of the shock as well as the steadiness of the barrel shock flow regions are also described by the lowest value of RMS species in Figure 30b. The region where the strongest level of fluctuations occur are immediately around the barrel shock and downstream of the Mach disk location. The strong fluctuations exemplify the location of where the largest velocity gradients between the crossflow (downwind of the shock) and the jet promote instabilities associated with mixing.

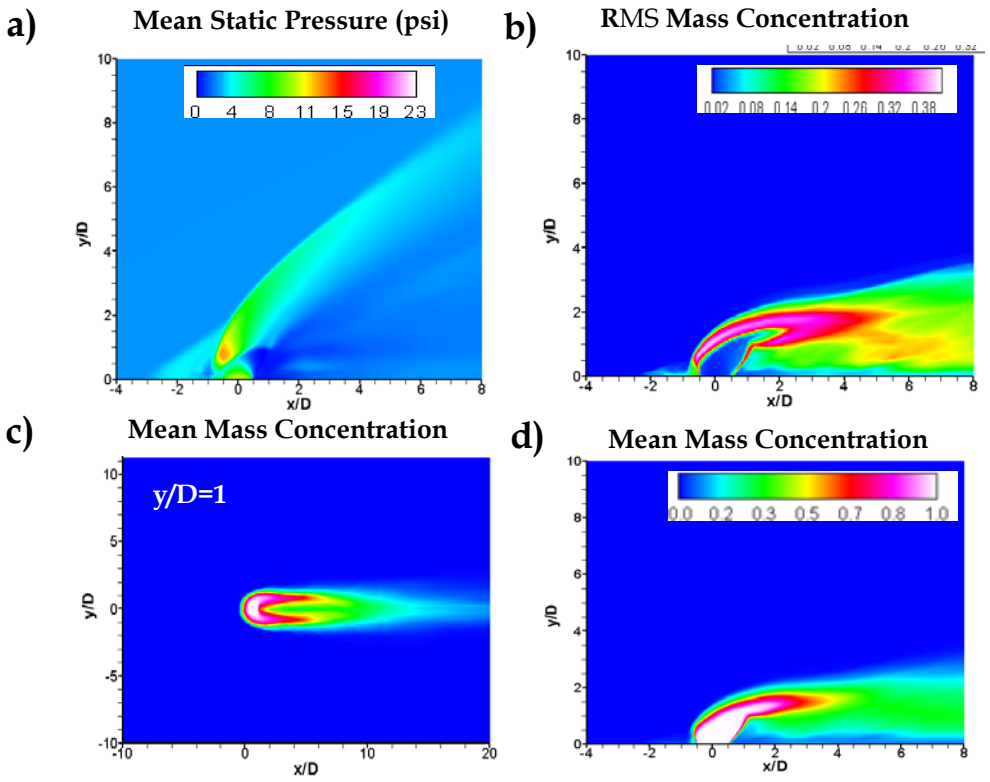


Figure 30: Time averaged views of static pressure (a), RMS hydrogen mass fluctuations (b), hydrogen mass concentration in the *x-z* plane (c), and hydrogen mass concentration in the *x-y* plane (d).

The constant-y plane view of the time averaged jet Figure 30c reveals the jet core bifurcation into a pair of counter-rotating vorticies. These results are consistent with studies of JICF which show that the CVP is strongest in the jet within ($x/D < 10$) and eventually merge in the far field producing a single concentration profile. It is evident that in steady injection, the species concentration is strongest near the injector as the initial jet momentum is mostly vertical.

Time averaged views of transverse axial velocity component and normal velocity component are visualized in Figure 31a-b. These images are consistent with the description of the relationship between jet mass concentration and the influence of the crossflow velocity and jet-velocity gradients on mixing and jet turning. The transverse component of velocity has little influence on the jet near the wall injection location ($y/D < 1$). Since the jet is under-expanded ($P_j < P_{eb}$) an expansion fan is created at the injector exit area to balance the pressure, producing the barrel shock when the jet returns subsonic. In this region the y-velocity and momentum are the strongest (as is seen in the right side image of Figure 30). However, at the Mach disk location the jet y-velocity becomes weaker and the crossflow velocity and momentum dominate; at this juncture, the jet trajectory is

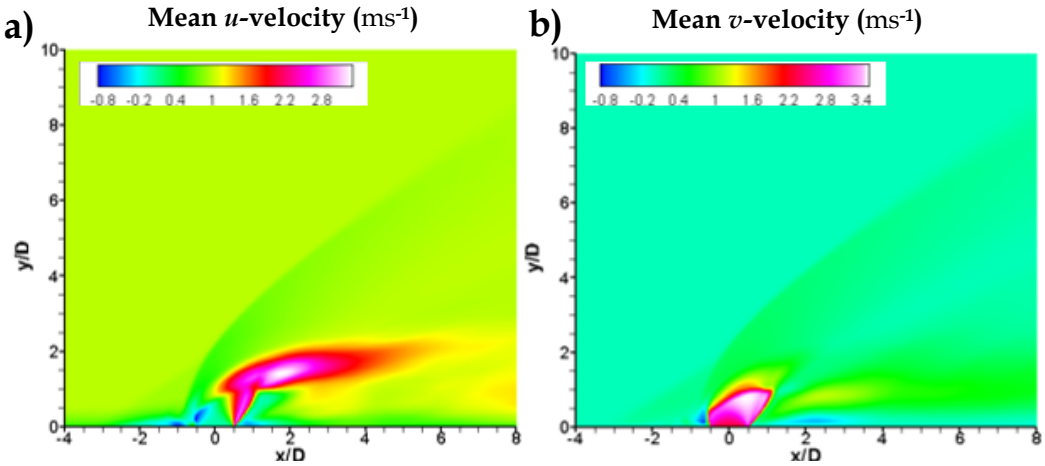


Figure 31: Time averaged images of x-velocity (a) and y-velocity (a) normalized by the free stream velocity (U_c=556 ms^{-1}).

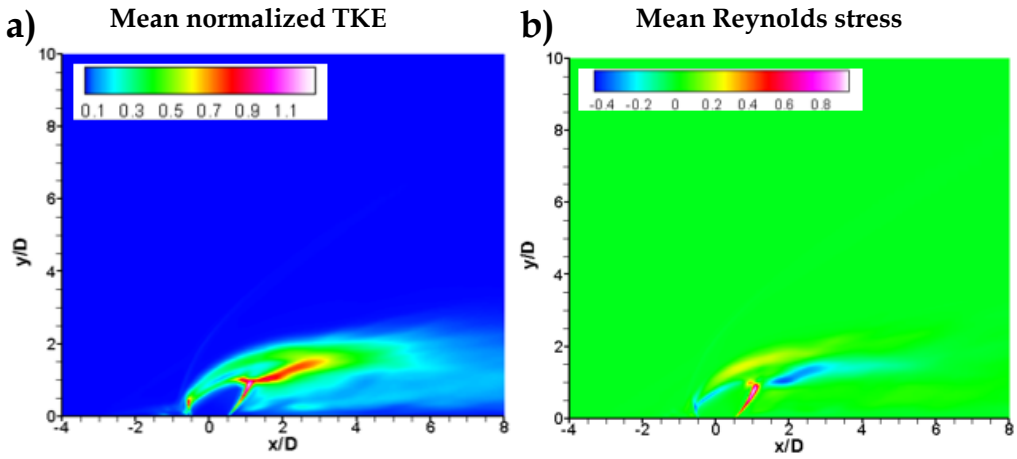


Figure 32: Mean normalized turbulent kinetic energy (TKE) (a) and mean normalized Reynolds stress distribution (b). TKE is normalized by the square of the free stream velocity (U_c = 556 ms^{-1})

dominated by crossflow momentum.

Figure 32 includes contours of mean turbulent kinetic energy or TKE ($(u'u' + v'v' + w'w')/2U_c^2$) (left side) and the *uv*-component of Reynolds stress distribution ($\overline{u'v'}/U_c^2$)(right side), normalized by the square of the free stream velocity ($U_c = 556\ m/s$). Two particularly high regions of TKE occur, one upstream of the barrel shock and a second downstream of the Mach disk, where the jet turns and becomes dominated by crossflow momentum. This is consistent with the works of Kawai *et al.* [74] with notable exceptions.

Kawai *et al.* show the downstream TKE rise to be shorter and less intense than in the current study. Kawai reported a simulation result based on a higher momentum flux ratio ($J = 1.7$) based on the experiment by Santiago *et al.* [119]. Kawai *et al.* suggested that the higher TKE regions are associated with regions of high mixing and fluid dilution. Based on the RMS jet mass concentration contour in Figure 30, the current results are consistent with this description.

The Reynolds stress distribution contour in Figure 32 (right) show that the minimum values of the *uv*-component of Reynold's stress are located upstream of the bow shock (windward facing side) and the region downstream of the Mach

disk location. In other words, *uv*-Reynolds stress minimum corresponds to the regions of maximum normalized TKE. Kawai *et al.* showed the similar trends, suggesting that the large Reynolds stress components exist where the large fluctuations induced by vortices, both upstream and downstream of the barrel shock create strong shear regions. The current results are consistent with this description.

4.3.3 Quantitative Analysis and Theoretical Comparisons

4.3.3.1 Jet Penetration and Trajectory

Thus far the simulation results obtained in this present study and presented so far have all been qualitative. It is imperative to find quantitative means to verify that the models produce adequately accurate results. One of the focal points of this study is prediction of jet penetration into the supersonic crossflow. As was done in the 2D simulations, the ANSYS FLUENT line/rake command was used to produce mass concentration profiles at various axial locations along the jet trajectory. Jet penetration at each sample location (x/D) is defined as the highest location as measured from the wall ($y/D = 0$) where the mean mass concentration profile was 10% of the peak value ($10\%\bar{Y}_{max}$). This was the definition used by Kawai *et al.* for a PJISF. Figure 33 shows a plot of the locations of the jet penetration

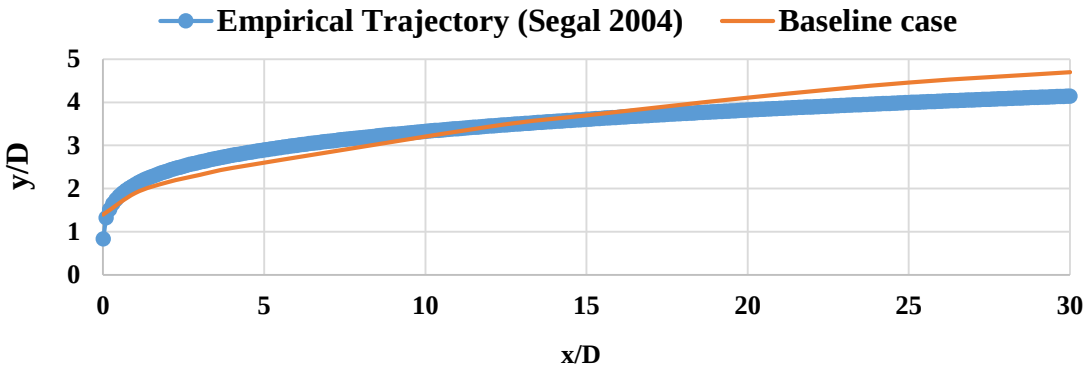


Figure 33: Penetration trajectories (based on 10% of the mean mass concentration profile) scaled with jet diameter (*D*) compared with Segal [3].

trajectory for the baseline case (based on $10\%\bar{Y}_{max}$). The plot in Figure 33 reveals the mass concentration based trajectory data plotted against Eq. (1-7) from Segal [3]. The data in both curves is normalized by jet diameter (D). Both trajectories show similar trends; the baseline model adequately describes mid-field penetration, falling on the curve from Eq. (1-7) at $x/D = 14$. The trajectory is under predicted in the near field ($x/D < 10$) and slightly over predicting in the far field ($x/D > 20$). The largest near field error occurs at $x/D = 3$ (11.3 %) and in the far field at $x/D = 30$ (13.3%).

Segal suggested penetration characteristics for JISF are secondarily sensitive to the boundary layer thickness, which drastically affects near field penetration, but is inconsequential to penetration in the far field. Future investigations should focus on comparing penetration characteristics in the use of an unsteady turbulent inflow boundary layer profile with a RANS turbulent inflow. It remains to be seen whether or not this is the cause of the disagreement.

4.3.3.2 Comparison with Theory

Theoretical comparisons were made to compare the baseline case results against. This section discusses both the use of 1D compressible flow relations and also specific empirical relations related to estimations of predicted reflection shock length and Mach disk height. For 1D compressible flow comparison, flow properties across the bow shock were calculated (assuming it was behaved as a normal shock near the wall), using the normal shock relations from Anderson (with $\gamma = 1.4$ used for air) [121]:

$$M_2^2 = \frac{1 + [(\gamma - 1)/2]M_1^1}{\gamma M_1^2 - (\gamma - 1)/2} \tag{4-2}$$

$$\frac{p_2}{p_1} = 1 + \frac{2\gamma}{\gamma + 1}(M_1^2 - 1) \tag{4-3}$$

$$\frac{T_2}{T_2} = \left[1 + \frac{2\gamma}{\gamma + 1}(M_1^2 - 1)\right]\left[\frac{2 + (\gamma - 1)M_1^2}{(\gamma - 1)M_1^2}\right] \tag{4-4}$$

where the subscripts 1 and 2 represent flow properties upstream and downstream of a normal shock.

Furthermore, to compare the injection properties produced by the simulation with theoretical values, 1D compressible relations for a choked nozzle were used to calculated injection pressure, velocity and temperature using the following expressions (with $\gamma_{H_2} = 1$ used for hydrogen and $M_j = 1$):

$$a_j^* = V_j^* = \sqrt{\gamma \mathrm{RT}_j} \tag{4-5}$$

$$P_j^* = P_{oj}\left(\frac{2}{\gamma_{H_2} - 1}\right)^{\gamma_{H_2}/(\gamma_{H_2} - 1)} \tag{4-6}$$

$$T_j^* = \left(\frac{2}{\gamma_{H_2} - 1}\right) \tag{4-7}$$

Three stations (1, 2 and j) correspond to free stream conditions upstream of the bow shock, immediately downstream of the bow shock and at the injector exit area. Figure 34 and Table 8 show local pressure, local velocity and local temperature results which were taken from the select stations from the central plane surface. This normal shock assumption is based on a conservative estimate of the flow pressure downstream of the base of a bow shock. At this location, the shock angle can be approximated as normal [17].

Normal shock tables were used to estimate local pressure, local velocity and

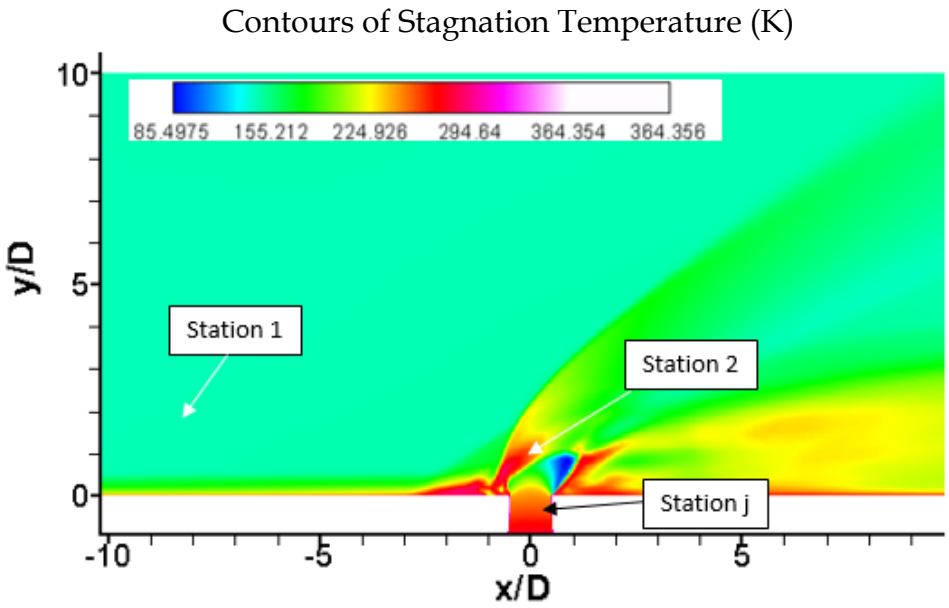


Figure 34: Contours of Static Temperature (K) of the baseline case showing the labeled station locations (1, 2 and j) which correspond to the free stream, downstream of the bow shock and nozzle exit area locations. Data was sampled from these locations for comparison with 1D compressible theory.

Table 8: Stations comparing 1D Compressible Theory with CFD results

Station	Flow Property	Theoretical Value	CFD	% Difference
1	P_1 (psia)	2.4	2.44	1.67
	V_1 (m/s)	556	554.1	0.34
	T_1 (K)	145	145.73	0.5
2	P_2 (psia)	14.412	13.72	4.8
	V_2 (m/s)	179.98	175.54	2.46
	T_2 (K)	282.315	284.77	0.869
j	P_j (psia)	11.95	12.01	0.5
	V_j (m/s)	1203	1202	0.083
	T_j (K)	249	249.87	0.35

local temperature downstream of the shock based on the prescribed free stream conditions (Mach 2.3, p_1 = 2.4, T_1 = 145). The results in Table 8 show that the CFD results compare well with theory. The largest difference for any of the sampled points is %1.67. This builds confidence in the selected model for studies of forced injection on the same grid with the same flow conditions.

For further validation, measurements were taken of the separation shock l_s upstream of the injection site and the Mach disk height h/D_j. The correlations for both measurements are displayed in Figure 35. The correlation from Glagolev [122] was based on the study of separation shocks and the resulting pressure rises on cylinders in supersonic crossflows. The relation for the Mach Disk height was taken from Schetz et al. [11] (see Eq. (1-3)).

$$l_s = 0.46\left(P_{oj}\right)^{0.4} \tag{4-8}$$

The results presented in Table 9 suggest that the CFD model predicts the separation shock length and Mach disk height adequately, with the largest error of 5.6%. Caution must be taken for the specification of Mach disk height. Several studies have used different correlations for estimating P_{eb} which can lead to a different result than what is displayed here. Everett suggested that the effective back pressure is only 35% of the injectant total pressure. This would give a larger estimation of the Mach disk height [123].

Everett suggested that the lower value of P_{eb} was more accurate for low momentum flux flows ($J < 1.5$). An explanation for the different result here is that Everett studied a flow where the crossflow Mach number was 1.6. Since Segal [3] suggests that crossflow Mach number strongly influences penetration one could conclude that for low momentum flux flows with higher Mach numbers the effect of effective back pressure would be more severe.

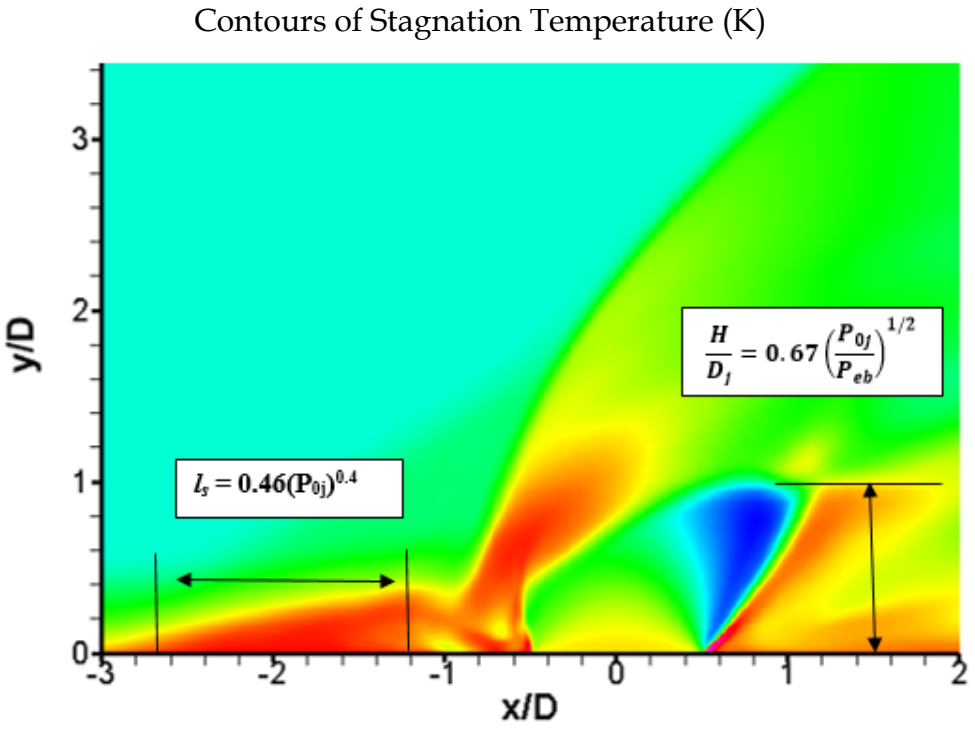


Figure 35: Contours of Stagnation Temperature (K) showing the locations of the separation shock and Mach disk height.

Table 9: Comparison of shock length and Mach disk with theory

Flow Property	Theoretical Value	CFD	% Difference
l_s	1.6	1.69	5.6
h/D_j	1.0785	1.11	2.92

4.4 Grid Independence Study

The previous sections demonstrated that the grid constructed for this study and WMLES model adequately resolves the large scale structures which are prominent in turbulent mixing of steady jets in supersonic crossflows. The large scale features (e.g. mentioned by Ben-Yakar *et al.*) are clearly visible at the grid resolution of the large grid (17.8M). This significant because it shows that the grid is likely to be able to resolve the large scale flow features associated PJISF, which is the primary motivation of this study. In subsequent sections, comparative results from the 17.8M grid and the 10M grid is presented.

4.4.1 Instantaneous Results

Two simulations were run for the unforced injection case: one with 10M cells and the other with 17.8M. Figure 36 shows instantaneous snapshot images of Mach number, numerical schlieren and iso-surfaces of Q-criterion (defined by Eq.(4-1)) colored with vorticity from the 10M grid (left column) and the 17.8M grid (right column). The images in Figure 36a-c for the 10M and 17.8M grids were taken approximately the same instant in time (0.314 *ms*) for direct visual comparison. Figure 36a shows that the Mach number contours for both grids capture the same large scale structures at the same instant in time. The 17.8 M cell grid adds finer detail and resolves smaller scales than the courser grid.

One can see the more detailed shock structure on the finer grid in the numerical schlieren image (middle right of Figure 36). In addition to resolution of the major flow features, the finer grid is able to capture secondary effects such as the horse shoe vortex recirculation region around the periphery of the jet (bottom images of Figure 36). Thus It has been demonstrated that adding (or removing) more grid points effects *resolution* but does not significantly change the general physical simulation results.

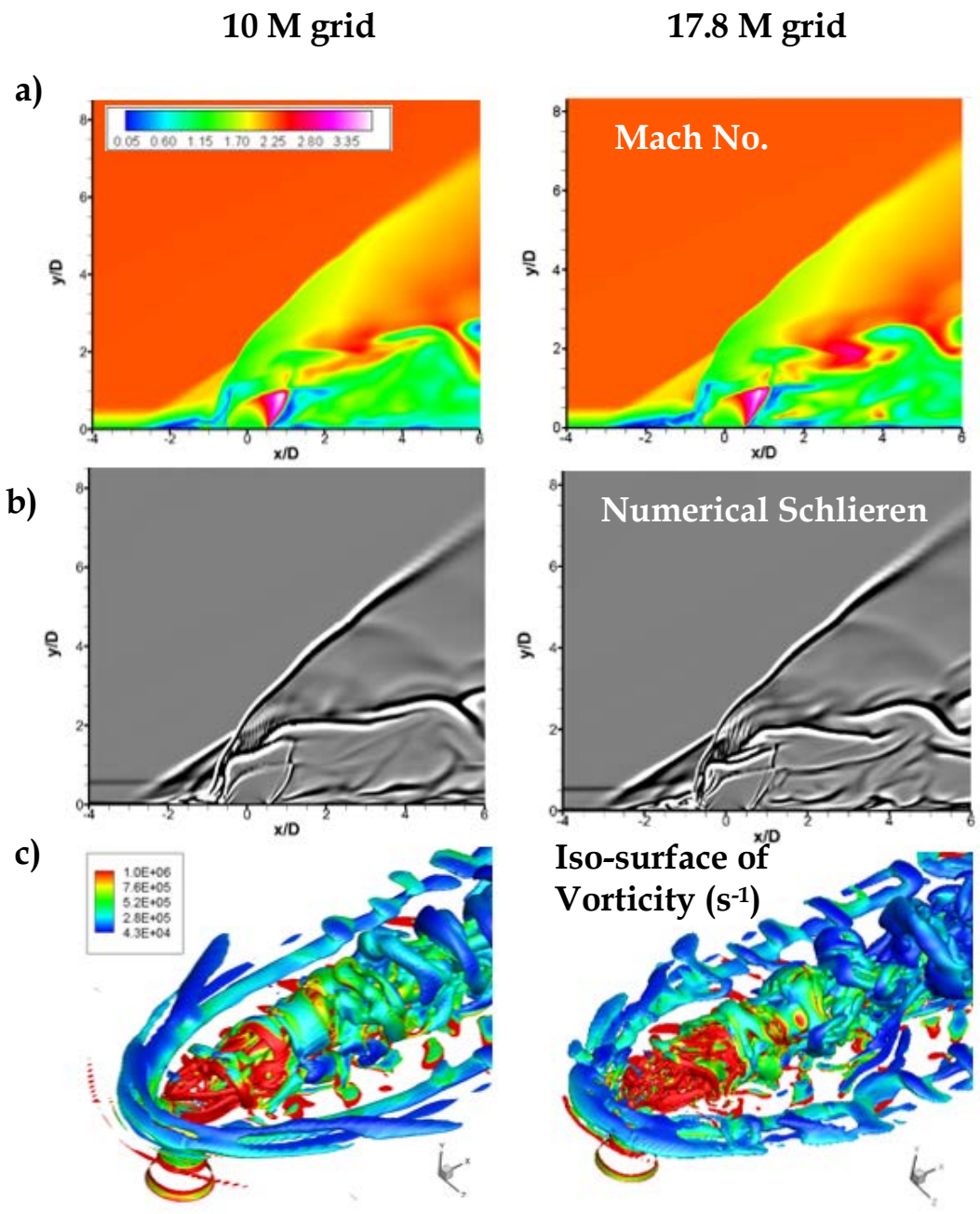


Figure 36: Comparison of simulations results from 10M (left) and 17.8M cell grids.

4.4.2 Time Averaged Results

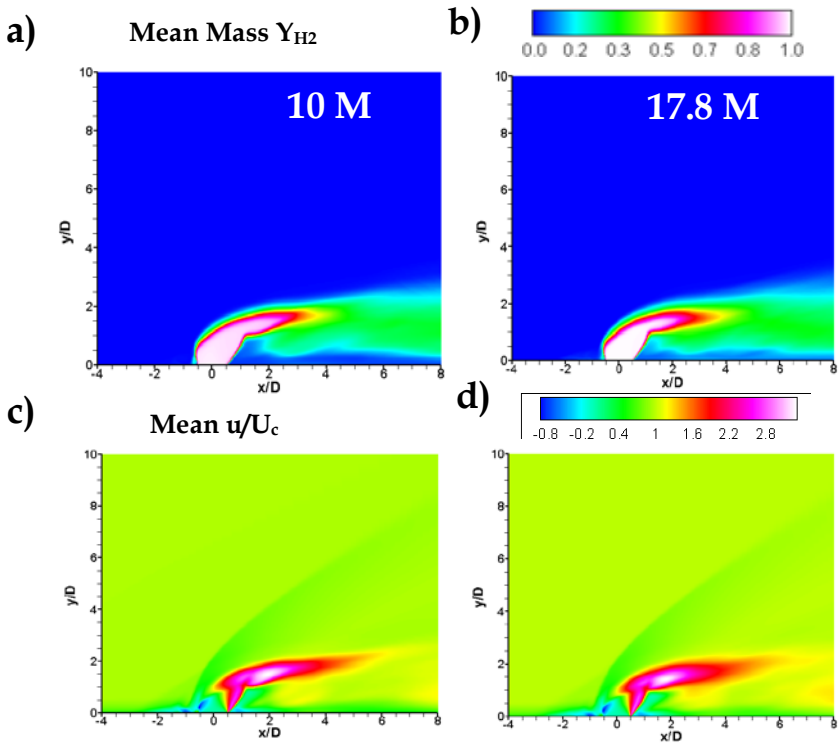


Figure 37: Time averaged images of mass concentration (a-b) and mean velocity (c-d) for 10M and 17.8 M cell grid

Time averaged statistics were taken from simulations on both grids over the same time frame (0.3 *ms*). Figure 37 shows a comparison between time averaged statistics of mass concentration and velocity for the 10M cell grid (left side of image) and the 17.8M cell grid (right). Contours are set to the same scale for all grids. Both grids resolve the same flow features and produce the same results. In addition to producing grid comparisons based on free stream and jet flow properties, it was of interest to compare wall resolution data between the grids.

Figures 38 and 39 shows a comparison between boundary layer profiles and wall pressure data for the 10M and 17.8M grids. The boundary layer profile data

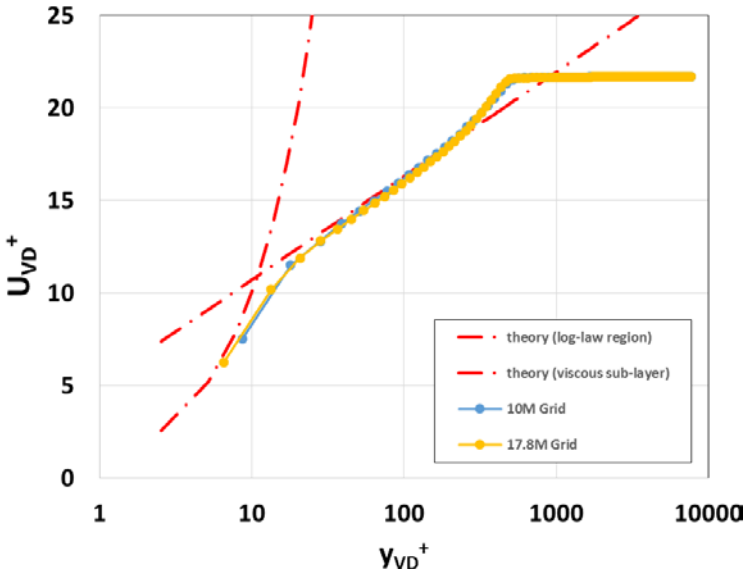


Figure 38: Boundary Layer Profiles compared with theory for 10M and 17.8 M cell grids (taken from the location upstream of the nozzle injector *x/D = -1*).

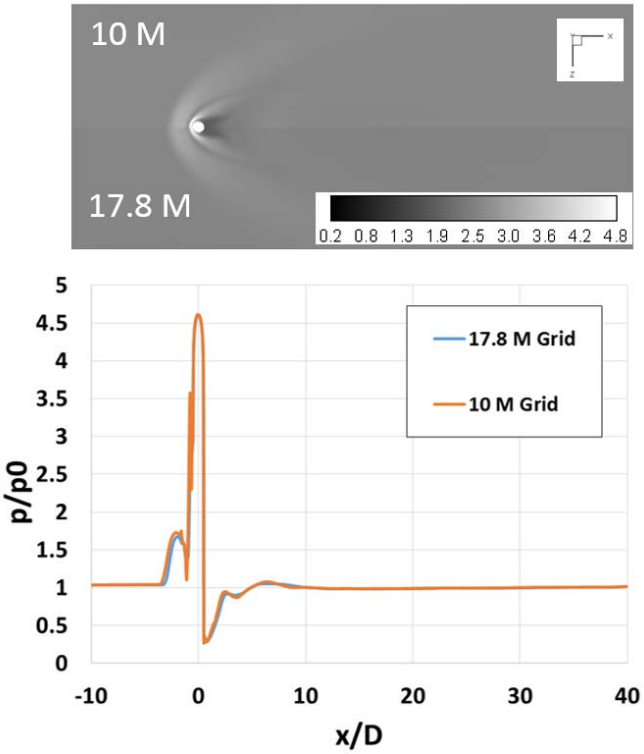


Figure 39: Top: Contours of wall pressure normalized by the free stream local pressure for 10M and 17.8M grids. Bottom: Wall pressure distribution for 10M and 17.8M grids.

were taken at the same location upstream of then nozzle injector $(x/D = -1)$ in both the 10M and 17.8M grids. Both profiles are transformed via the method of Van Driest to account for compressibility effects [116]. Figure 39 shows wall pressure data taken from time averaged statistics. Each grid matches theoretical curves in the log-layer strongly, suggesting that the solution is accurate. The 10M and 17.8M grids have y^+ resolution of about 8 and 5 respectively.

Figure 39 (top) shows contours of wall pressure data taken from time averaged statistics for both the 10M and 17.8M cell grids. Figure 39 (bottom) shows wall pressure distributed across the grid length from 52 jet diameters from the domain inlet. The wall pressure contour plot and axial distribution data shows agreement between the grids, building confidence that the simulation results are independent of grid density.

5 Characteristics of Pulsed Injection in a Supersonic Crossflow ($f = 16\ kHz$)

5.1 Section Overview

In this section, the 3D simulation results from Case 3 (sinusoidal pulsed jet at 16 kHz) is discussed (see Table 9 in Sec. 4.2). The primary goals of this chapter are presented in the following manner. First, the instantaneous flow field during at the time of peak injection is observed and described. Next, a description of the time evolution of pulsed injection over a full pulse cycle $(0 < t/T < 1)$ is presented. This description includes the effects of pulsation on the bow shock, reflected shocks and Mach disk as well as the depiction and resolution of large scale vortical structures which are characteristic of turbulent jets.

Furthermore, qualitative discussion of these results as they compare to previous experiments are also included in Chapter 5. Finally, pulsed jet penetration and mixing characteristics are quantified. A penetration trajectory for pulsed jet injection is constructed from samples of mass concentration, defined as 10% of the highest mass concentration profile as was done for the steady injection case. Mixing is also quantified by observing the axial decay of the mean species profile. These results are compared to the empirical scaling laws to observe the closeness of the simulation predictions with theory.

5.2 Snapshot of Pulsed Injection Flow Environment

3D simulation results of sinusoidal pulsation at 16 kHz is shown in Figure 40. The contours of Mach number (Figure 40a), hydrogen mole fraction (Figure 40b) and the numerical schlieren image (Figure 40c) reveal the highly turbulent nature of the flow field as a result of pulsation. The images displayed in Figure 40 were all sampled at cycle time ($t/T = 0.75$). Four fluid slugs are visible, each exhibiting LSV structures.

The benefit of using a 3D SRS is evident from the improved resolution of the LSV structures in comparison with the 2D simulation results in Chapter 3. The hydrogen mole fraction contour Figure 40b shows a fluid slug leaving the nozzle near location $x/D = 0$ which produces LSV structures near the interface between

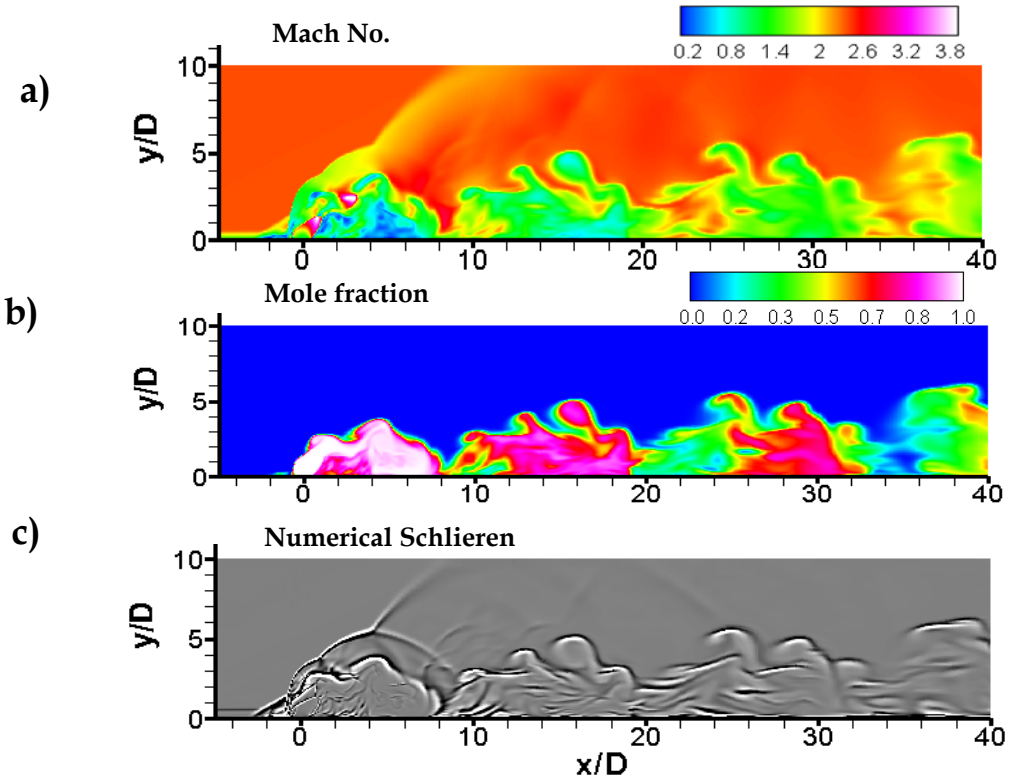


Figure 40: Instantaneous flow field of sinusoidal pulsed injection at f = 16 kHz. Pulse cycle time is t/T = 0.75. Contours are of (a) Mach number, (b) hydrogen mole fraction and (c) numerical schlieren.

the jet-slug and the crossflow. These large scale structures grow as surrounding fluid is entrained and the slug travels downstream due to the momentum of the crossflow. As an individual fluid slug moves downstream, mixing from the free stream flow causes the initially close fluid mass to slowly spread with the initial roll up structures becoming less defined over space and time. Notice that at length $x/D = 40$, the initially compacted fluid slug is an irregular turbulent "puff' of fluid.

In addition to the flow structure, a complex system of intersecting shock waves are visible in Mach number and numerical schlieren images of Figure 40. In addition to the wave-like behavior of the bow shock, weak shocks are produced by each fluid slug, and also by the individual eddies which roll-up on the surface of the fluid slugs. Interestingly, the computational grid presented here resolves the large-scale coherent structures produced by each fluid slug in the near field ($x/D < 40$) but far field resolution is weakened enough that the weaker shocks carried downstream by the fluid slugs are not easily visible at $x/D = 40$. This could be the result of the grid resolution in this region.

Near field inspection ($x/D < 10$) of the numerical schlieren image (Figure 41a) reveals that the emerging jet produces three large scale coherent structures, each of which carries its own local shock wave. The local shocks suggest large local velocity gradients and hence shear levels between the fluid slugs and the flow downstream of the main bow shock. Interestingly, the velocity contour in Figure 41 reveal unsteady shock-diamond like regions within the jet downstream of the Mach disk.

These regions produce high velocities relative to the downstream flow field. Generally, it is well known that the velocity gradients across a JISF immediately downstream of the bow shock creates local roll-up region as a result of Kelvin-Helmholtz instabilities. This phenomena is explained extensively by Ben-Yakar *et*

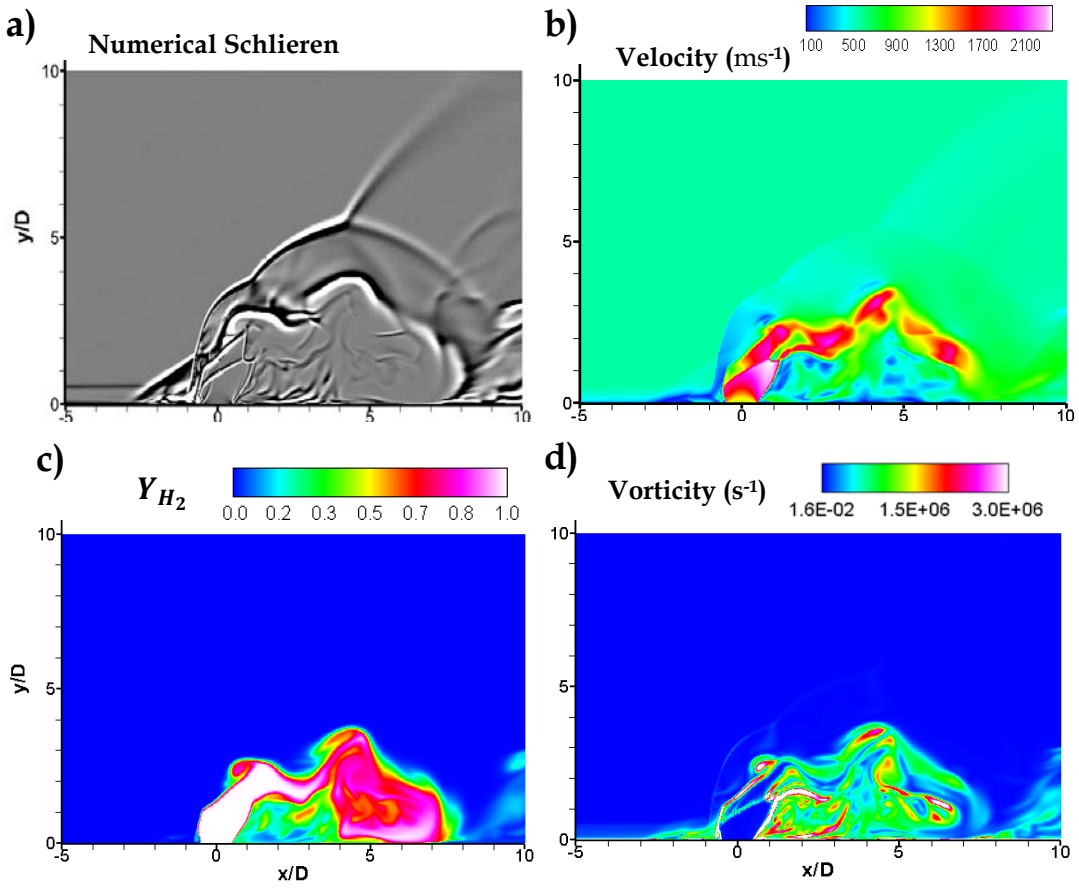


Figure 41: Near field pulsed jet behavior (*x/D < 10*). Contour plots include numerical schlieren (a), velocity magnitude (b), hydrogen mass concentration(c) and vorticity (d).

al. [17]. The velocity contour (Figure 41b) and hydrogen mass concentration contour (Figure 41c) reveal that the regions where the velocity gradient between the fluid slug and cross flow cause local large scale roll-up structures to form, which would tend to promote localized mixing on a similar eddy scale. The contours of vorticity (Figure 41d) reveals that in addition to local mixing in the jet-crossflow interface region, a large re-circulation region is formed downstream of the barrel shock. This corresponds to a similar region downstream of a steady jet where the pressure is lowest. For steady jets, this pressure is estimated by Eq.(1-1) or (1-2). It is well known that reversed flow is formed in this region. Interestingly, the magnitude of vorticity highest in this region, suggesting at this instant in time, entrainment and mixing is best promoted around the jet periphery.

5.3 Time Evolution of the Pulsed Jet (f = 16 kHz)

Figure 41 shows Mach number contours of the pulsed jet sampled over pulse period T (at jet off and quarter stroke increments). A full pulse stroke includes the following flow conditions: "jet off" ($t/T = 0$), a quarter stroke ($t/T = 0.25$), peak injectant pressure ($t/T = 0.5$), 75% stroke ($t/T = 0.75$) and a return to "jet off" condition ($t/T = 0.75$). Pulse cycle time (t/T) is defined in Sec. 3.3.2 (using the definition from Ref. [53]).

Several dramatically different flow features are present during a pulse cycle. At cycle time $t/T = 0$ the emerging jet already interacts with the weakened bow shock from the previous pulse. Also, the crossflow pushes the bow shock and separation shock over the injector; the boundary layer re-attaches near the injector location. At $t/T = 0.25$, the separation shock is already above the injection site. A new shock bubble forms around the injector. The new jet fluid emerging from the nozzle is always choked at the nozzle exit; the flow is never supersonic in the

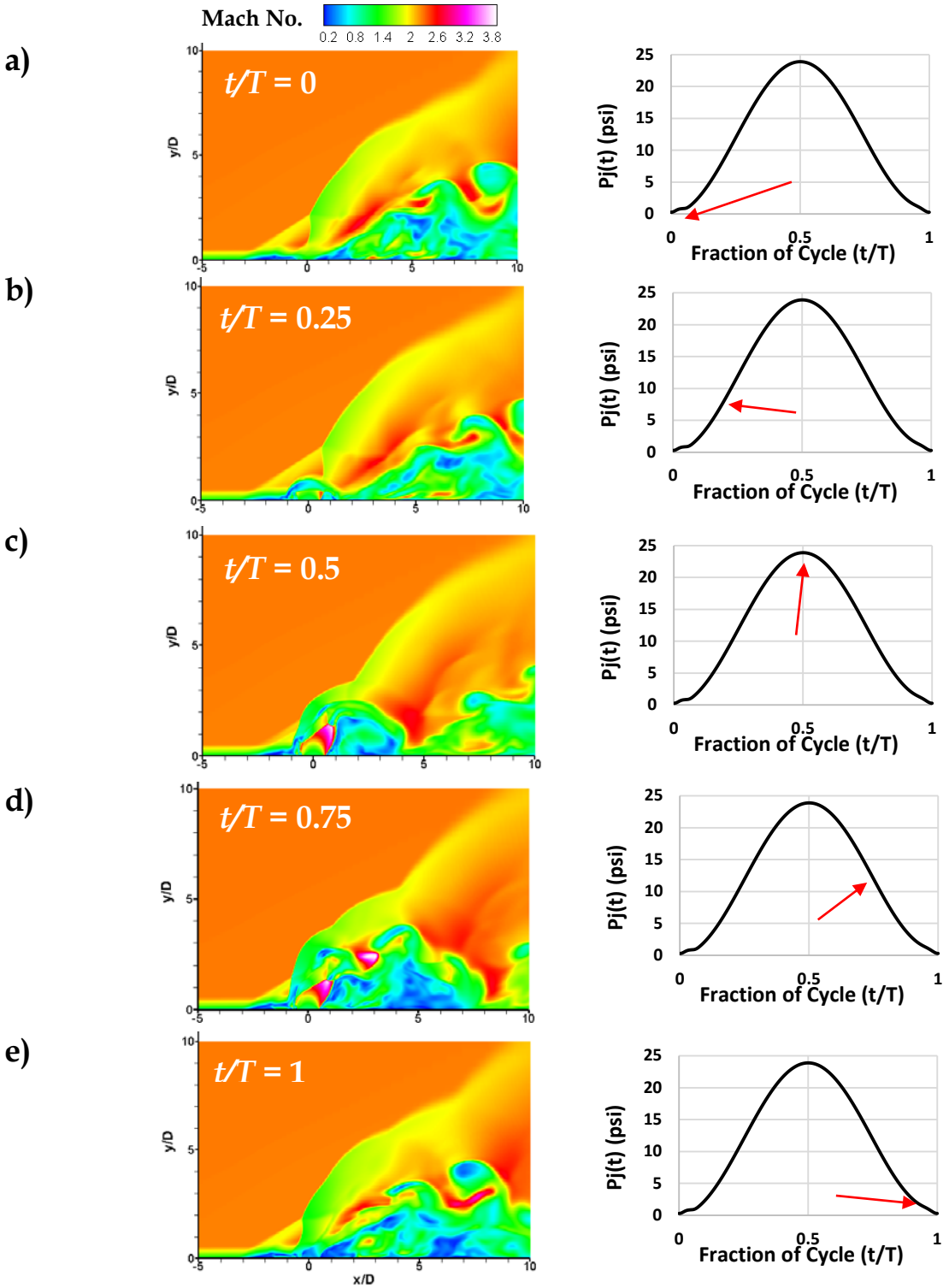


Figure 42: Near field evolution of sinusoidal pulsed injection at 16 kHz over one full pulse cycle. Contours are of Mach number.

nozzle. Since the jet is still under-expanded due to lower back pressure above the injector, a small barrel shock and Mach disk is formed; the barrel shock has a toroidal shape as fluid is rolled up near the injector exit plane. The direction of this Mach disk is in the downstream direction because of the momentum of the crossflow. At $t/T = 0.5$, the injectant pressure reaches the peak value. At this point, the barrel shock is fully formed and the Mach disk is pushed far into the crossflow. As the pulse starts to enter a downward stroke ($t/T = 0.75$), the jet's vertical momentum begins to weaken and the crossflow begins to dominate. The bubble shock has grown and behaves similarly to a standing bow shock, but is still exhibits a wave-like interface with the free stream crossflow. The jet plume now starts to roll-up as the velocity gradients between the jet and the crossflow dominate the jet/crossflow interface. At time $t/T = 1$ the jet is close to 'fully off' and a new cycle begins.

The computations made in the present study indicate that a Mach disk forms almost instantaneously in the emerging jet structure during the rising phase of the pulse cycle. Randolph *et al.* previously suggested that high frequency pulsation might occur over such a small timescale that the Mach disk might not form (fully or partially) and thus reduce total pressure losses in PJISF [55]. The present results indicate that Mach disk formation occurs on a very small time scale ($t <<$ 1μsec). Thus jet pulsation does not circumvent the formation of a Mach disk.

Figure 43 shows the time evolution (over 1 pulse cycle) of the near field of the jet, in terms of the mass fraction, velocity and vorticity. At time t/T = 0 a dissipating fluid slug from the previous stroke is visible in Figure 43a. The velocity contours indicate that the weakened bow shock is being carried downstream, along with the departing slug). The departing slug is still surrounded by and exhibits a strong mixing region as is shown by the contours of mass fraction and

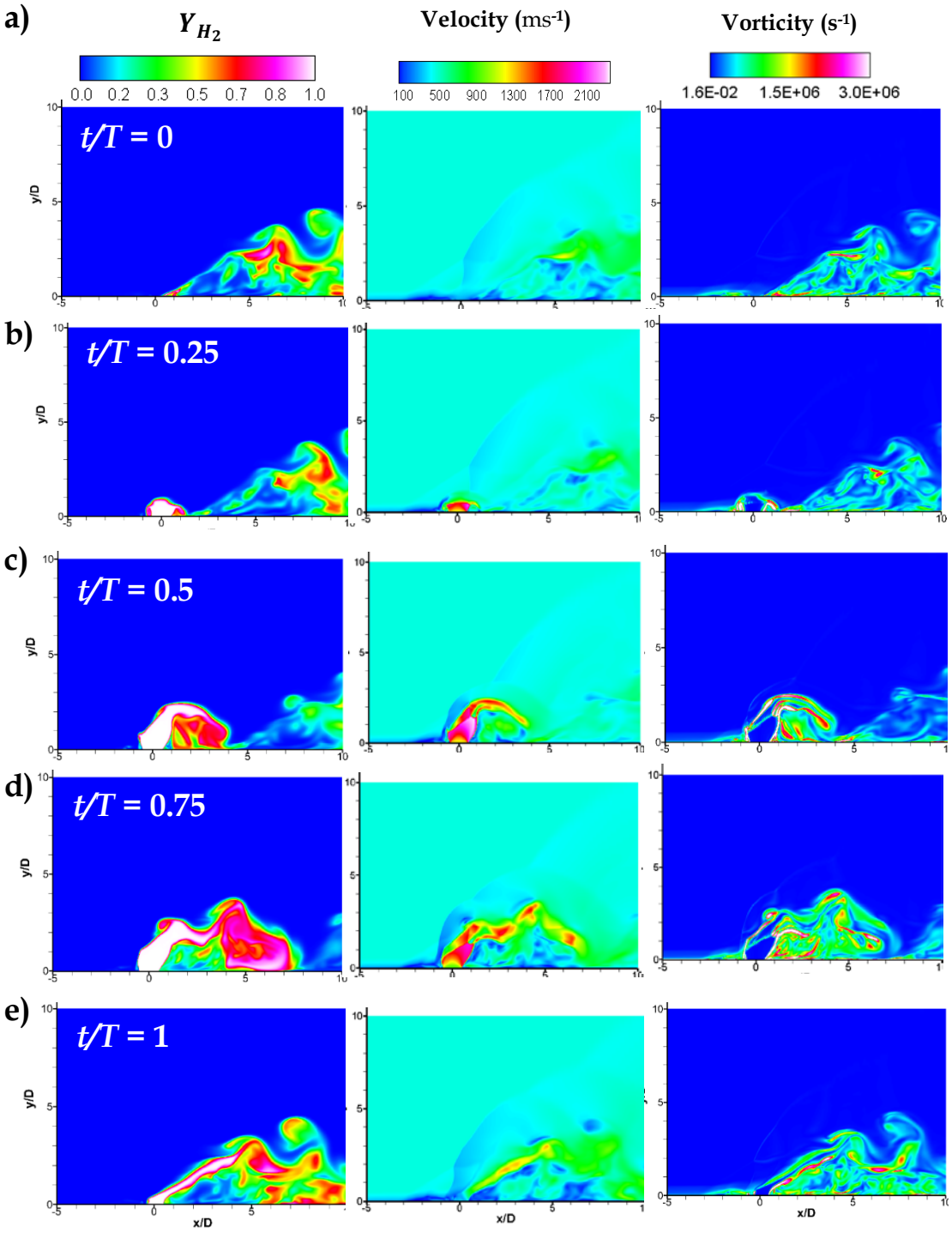


Figure 43: Evolution of pulsed jet injection at 16 kHz over a full pulse cycle. Contours are of hydrogen mass fraction (left column), velocity (middle column) and vorticity (right column). Rows (a) – (e) represent the portions of the pulsation cycle (times t/T = 0 -1).

vorticity (Figure 43b). In fact, as it the slug is carried downstream by the crossflow, it entrains upstream fluid with it, producing a streamer, similar to the streamers visible in pulsed vortex rings in which the stroke ratio L/D is higher than the formation number ($L/D = 4$) [66]. These results indicate that for a low cycle-averaged momentum flux ratio ($J_{cycle} \leq 1$), a turbulent mass forms instead of a distinct vortex ring. This is consistent with the works of Johari for jets with blowing ratio or effective velocity ratios ($r < 2$) [50].

At $t/T = 0.25$, the new jet emerges from the orifice; the mass fraction contour shows a toroidal region of rotating fluid emerging from the lip of the nozzle. This point in the cycle corresponds to a strong local region of vorticity, along with the barrel shock mentioned previously (Figure 43b). At $t/T = 0.5$ the jet pulse has fully emerged, along with the shock structures. Vorticity is promoted strongly in the recirculation region on the leeward side of the barrel shock.

By time $t/T = 0.75$, the pulse stroke is on the declining side of the cycle but the jet momentum forces are still high, and the jet continues to rise, followed by its eventual dominance by the crossflow. The initially small eddies have now grown; three primary eddies are visible in the mass fraction contours. These promote mixing and strong regions of recirculation which carry the fully formed turbulent mass downstream. By time $t/T = 1$, the large scale structures begin to rotate about an axis perpendicular that is to the *x-y* plane. The rising of the turbulent slug may be enhanced by vorticity induced velocities, which describes the increase of jet penetration into the far field during subsequent pulsation cycles.

Figure 44 shows iso-surfaces of Q-criterion (Q = 10^9 s^{-1}), colored with vorticity (left and middle rows) and Y_{H_2} (right row). During the rising phase, the vortex core region immerging from the nozzle displays high concentration of vorticity. As the jet emerges, the large scale roller regions are seen to grow. Three

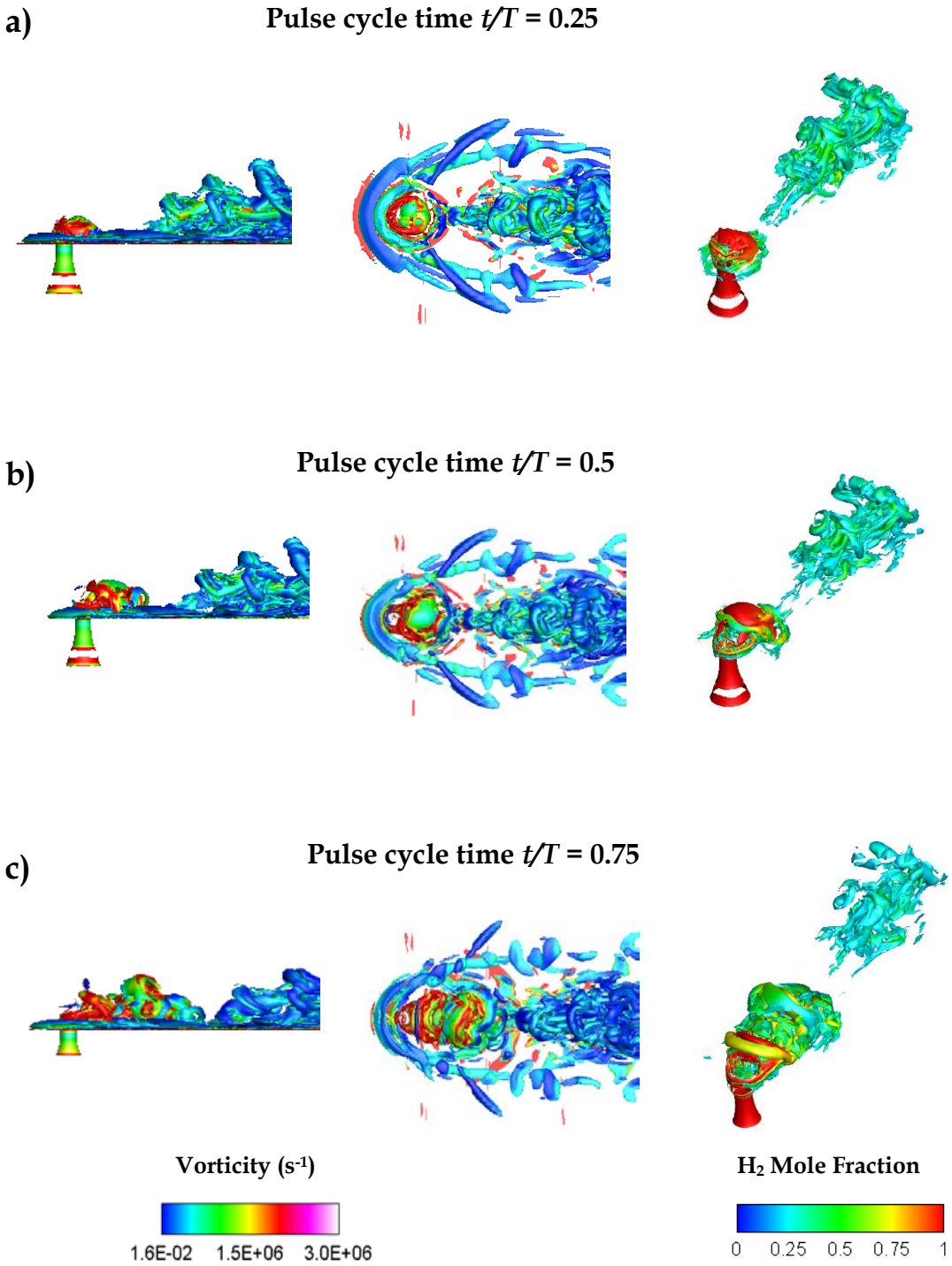


Figure 44: Iso-surfaces of Q-criterion (Q = 10^9 s^{-1}) during the rising (a), peak (b) and falling phase of a pulse cycle. Iso-surfaces include *x-y* plane views (left column), *y-z* plane vies (middle column) and (profile views of jet development). Contours are colored by vorticity (left and middle columns) and hydrogen mole fraction.

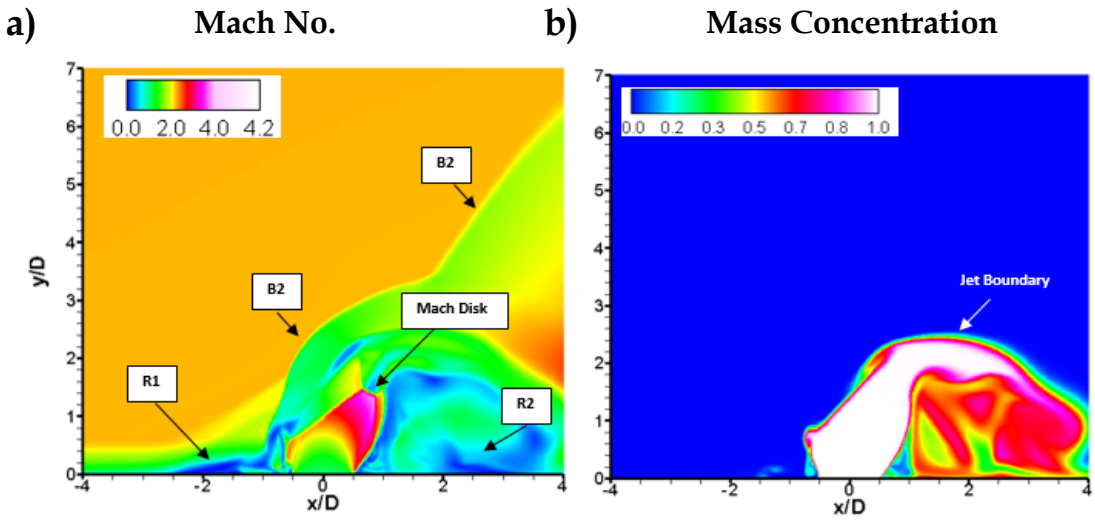


Figure 45: Jet penetration and shock structure at cycle time t/T = 0.5. Contours of Mach number (a) and hydrogen mass concentration of jet near field (b) are displayed in this frame

predominant large scale structures emerge as the jet moves downstream. The middle column of images in Figure 44 show the unsteady horse-shoe vortex region forming during the pulsation cycle. The horseshoe vortex region begins to increase its circulation strength in tandem with the rising phase of the cycle. The vorticity is strongest at this instant in the cycle ($t/T = 0.5$). The far field jet slug continues to lose shape (even further) as the slug is pushed downstream and eventually mixed into the flow field. This is demonstrated in the iso-surface contours colored by Y_{H_2}(Figure 45b). Thus penetration and mixing are promoted during one pulsation cycle of the PJISF.

Figure 45a shows the computed near field region of a jet pulse at $t/T = 0.5$. Features similar to steady injection including the upstream and downstream re-circulation zones (R1 and R2), are visible. The Mach disk is also more clearly defined. The peak Mach number in the barrel shock is $M = 4.1$, which shows that at this instant, the jet is highly under-expanded. The bow shocks (B1 and B2) represent the newly forming shock (bubble shock) and the shock from the previous pulse (B1).

Interestingly, the recirculation zone R2 is enlarged, suggesting that this area could be used to promote mixing. The recirculation zones are dependent on the pulsation frequency rise and fall time (20 to 30 μsec for pulsation at 16 kHz). Thus any mixing improvements due to the rise and all time due to pulsation. At the peak phase of the pulse, the peak jet boundary location ($y/D = 2.54$) is well above the Mach disk location ($y/D = 1.45$) in terms of height. However, both locations suggest that during the peak portion of the cycle, penetration of the jet is improved over unforced injection.

5.4 Time Averaged Characteristics of Pulsed Injection

Figure 46a shows the time averaged statistics of the mass concentration near fields. The time averaging was performed over approximately 0.3 *ms*

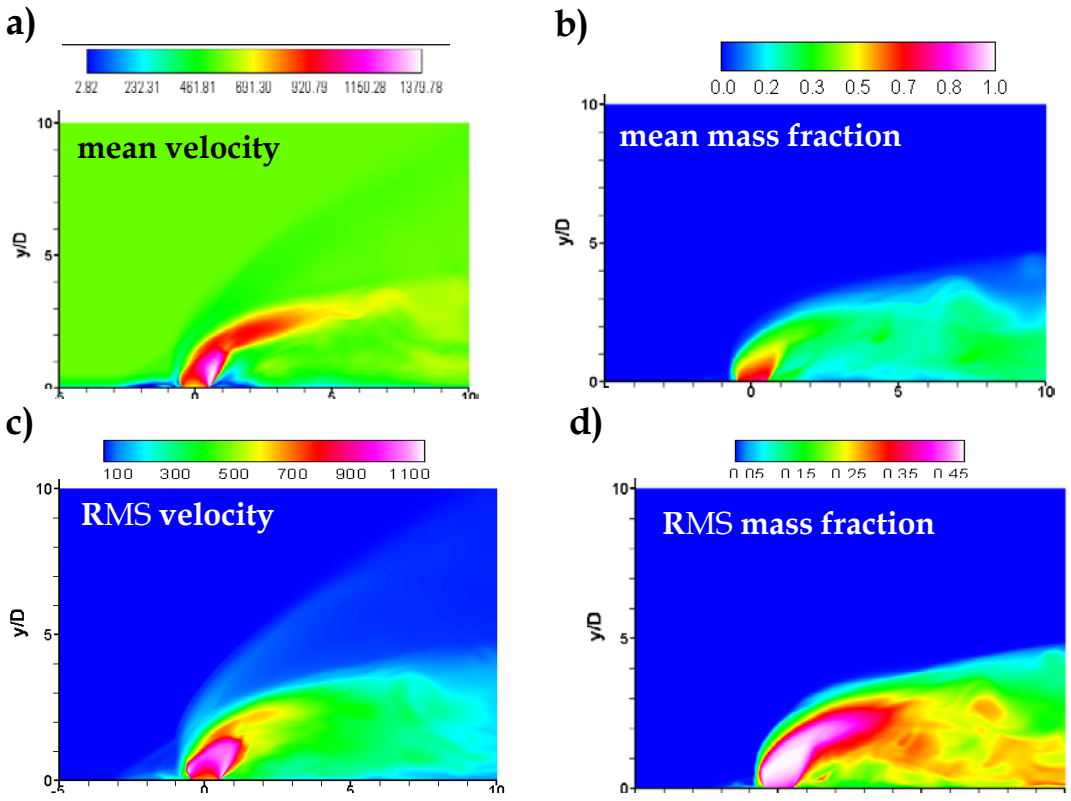


Figure 46: Time averaged views of pulsed injection: (a) and (b) are mean velocity and hydrogen mass concertation, (c) and (d) are RMS velocity and hydrogen mass concentration

(over 4.75 pulse cycles). The time averaging was set up to match the averaged time of the steady injection case. From the time averaged results, it is seen that pulsed injection pushes the time averaged jet deep into the crossflow. The velocity contour reveals a jet in which the Mach disk and barrel shock are higher and larger than the steady injectant case. The RMS velocity contour (Figure 46c) shows the significant changes of the fluctuating velocity, peaking in the barrel shock region and slowly dissipating along the jet trajectory as the jet is forced downstream. The species concentration and RMS species concentration images (Figure 46d) show increased mixing zones in the flow field downstream of the jet. The RMS magnitude peaks where the jet plume is strongest (in the barrel shock), but also promotes significant changes and fluctuating species concentration downstream of the jet.

Figure 47 shows contours of u-velocity and v-velocity (top), RMS u-velocity and v-velocity (middle) and Turbulent Kinetic Energy or TKE ($(u'u' + v'v' + w'w')/2U_c^2$), and the uv-component of Reynolds stress ($\overline{u'v'}/U_c^2$); both are normalized by the free-stream velocity ($Uc = 556\ m/s$). The contour of u-velocity (Figure 47c) shows how dominant the crossflow velocity is on the jet penetration. The jet locally is accelerated in the y-direction near the injection site, where the jet peak velocity is 2.04 times the crossflow velocity.

In the far field, especially downstream of the barrel shock/Mach disk location, the jet is immediately turned toward the free stream direction. Momentum gains by pulsation (on average) are not fully lost as the jet boundary exhibits a higher arc than in the unforced case. The magnitude of velocity is significantly diminished in the far field however. The contour of Turbulent Kinetic Energy show that the strongest turbulence generation in the jet occur in the barrel shock region. This is significantly different than in the unforced injection case. The

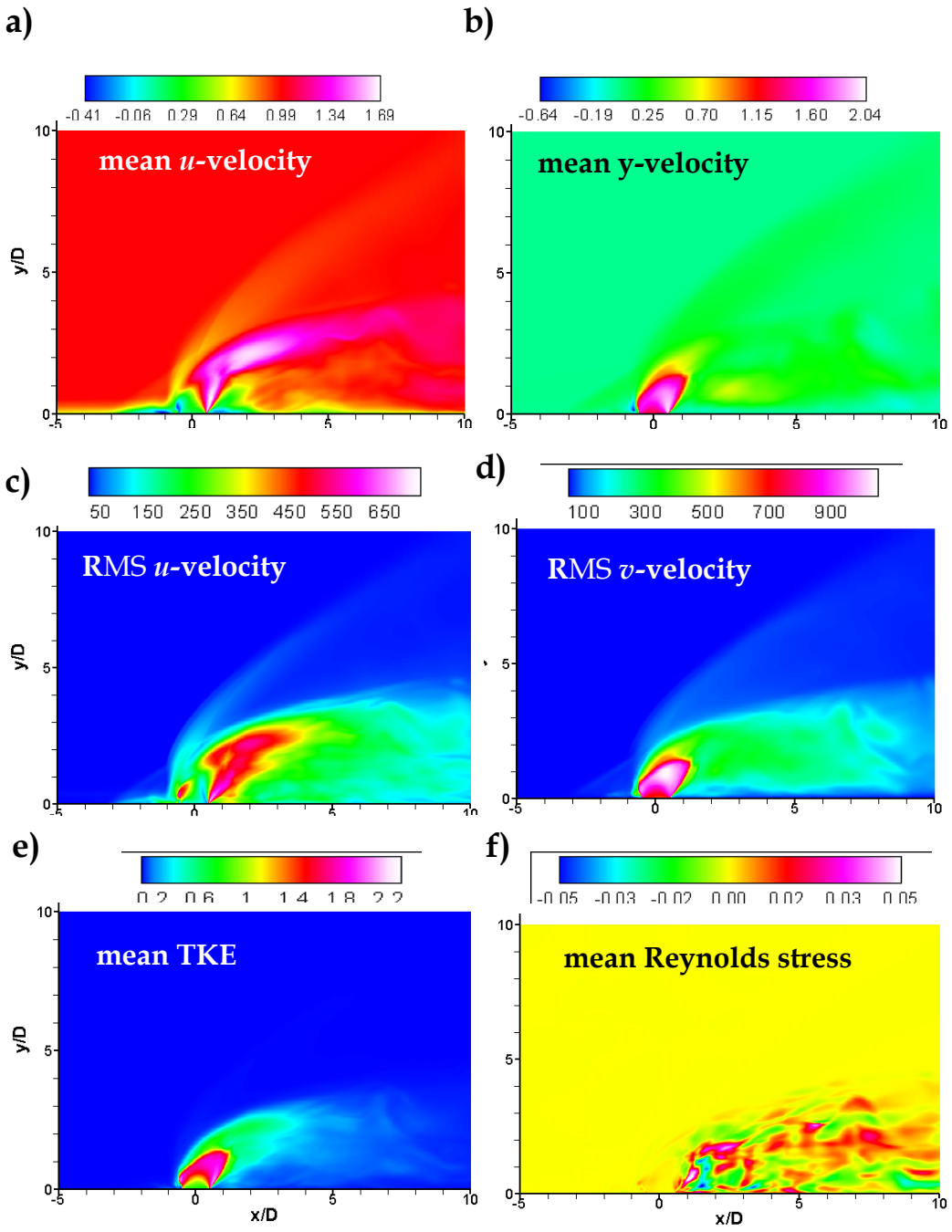


Figure 47: Time averaged images of *u*-velocity and *v*-velocity (scaled with crossflow velocity U_c=556 ms^{-1}) (a-b), RMS *u*-velocity and RMS *v*-velocity (c-d). Time averaged turbulent kinetic energy (TKE) and Reynolds stress (e-f) of the PJISF.

implication is that mixing occurs at a quicker rate as a result of pulsation. The contour of Reynolds stress also exhibit drastically different characteristics than for the unforced injection. Some consistency with the unforced case (and other works in literature) include the trend in which the most negative value of Reynolds stress still occurs where the peak TKE values occur. This time it is in the barrel shock and its periphery. It remains to be demonstrated experimentally if the turbulent physics is adequately captured for the PJISF case.

5.5 Theoretical Trajectory and Species Decay of Pulsed Injection

To measure the performance of jet pulsation on penetration, the time averaged species concentration (based on 10% $\bar{Y}_{max}$) was used to compare directly with the approach used for the unforced injection case. Concentration profiles of mass concentration were taken using the line rake function in ANSYS FLUENT at several locations in the jet near field and far field. This data was plotted against the theoretical pulsed jet penetration curve from Pasmurti *et al.* (Eq. (1-33) [72]. The theoretical curve proposed by Pasmurti *et al.* accounts for both an effective

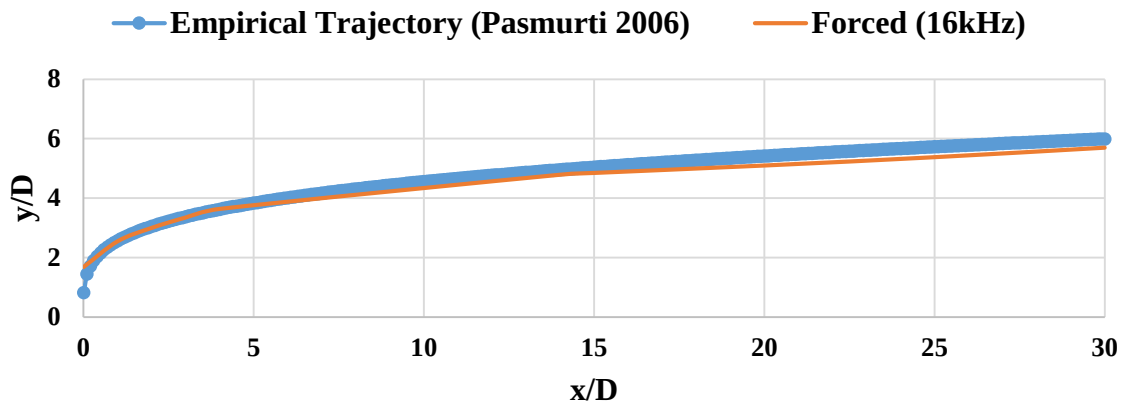


Figure 48: Trajectory comparisons between Eq.(1-33) and the time averaged jet penetration of the pulsed jet.

momentum flux ratio based on mean jet velocity characteristics and also the stroke length, L/D. For the present study, the pulsed jet pulse cycle implemented results in a stroke ratio of $L/D = 18$ calculated based on the mean jet exit velocity, measured at the nozzle exit. Figure 48 shows a comparison between the jet trajectories proposed by Pasmurti *et al.* and the current study results. The pulsed jet trajectory based on the results presented in this study are consistent with the theory curve of Pasmurti *et al.* (1-34) for k = 1.25. Studies which used previous forms of this equation have proposed a variety of values for k from 2.1 – 3. None of the other previous studies have developed theoretical curves for pulsed jet injection into a supersonic crossflow. The values for k have been modified in other computational simulations to account for discrepancies in the simulation approaches [72].

In the current study, when k = 1.25, the empirical expression and the pulsed injection data produced by the LES CFD correlate strongly beyond $x/D = 15$. The jet boundary in the near field $x/D < 5$ is less conservative than is predicted by theory. Pasmurti *et al.* suggested that an exact match from CFD to Eq. (1-36) would be not be exact. Overall, the strong correlation in the near field beyond $x/D = 5$ produces confidence in the model, the approach and the use of a the 17.8M grid

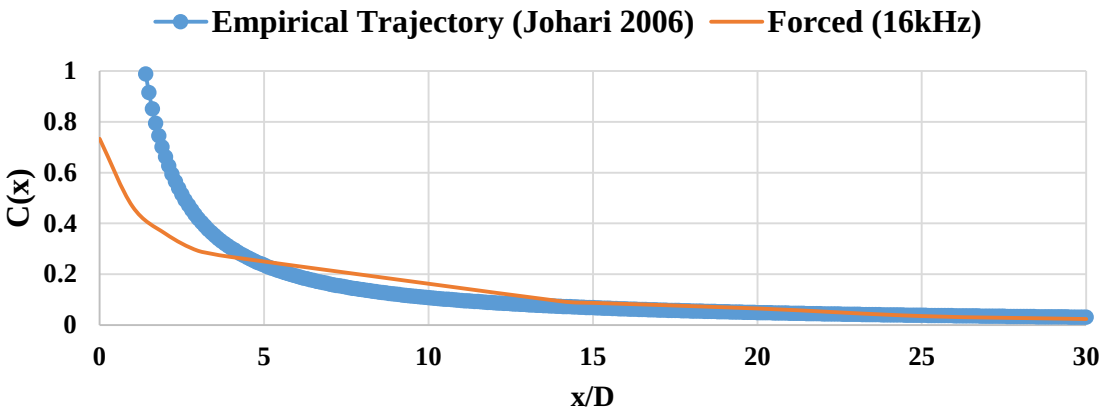


Figure 49: Mass concentration decay curve (Eq. 1-36) [50] compared with current simulation results.

to model pulsed injection. Measuring mixing of a jet in crossflow is challenging, since a variety of definitions and approaches to what 'mixed' actually means exists in literature. In the current study, a measure of mixing is estimated by the rate of mass concentration decay as is described by Johari [50]. Several authors since Johari have used or modified this curve to fit their concentration data. Pasmurti *et al.* compared simulations of heated compressible jet concentration decay to the curve produced by Johari [50].

It was suggested that since Johari assumed transport of turbulent puffs along the flow wise axis that error between the theory curve and simulation results may affect the fit for $x/D < 5$ [72] . The current simulation shows this; in the near field the decay rate is less steep, and the species concentration is lower than theory predicts. However, in the far field region ($x/D = 15$) the theory and CFD data correlate strongly.

6 The Effects of Pulsed Injection on Jet Penetration and Mixing

6.1 Primary Investigation Overview

The previous chapters (3-5) presented results from 2D and 3D simulations of steady and pulsed injection. In Chapter 3 it was demonstrated in the 2D simulations that pulsed injection improved time averaged (and instantaneous) penetration of fuel jets in supersonic crossflows across the range of frequencies under investigation (8 - 48 kHz). It was also demonstrated that operating at 16 kHz improved penetration the most in both the near field and far field.

Chapter 4 described a 3D model of unforced injection constructed in this research study, which resolves the important large scale structures important in observing mixing of a JISF. Furthermore, the 3D model was shown to produce flow variables that compare reasonably well to compressible flow theory as well as to empirical trajectory results. Chapter 5 showed important numerical results which describe 3D pulsed injection at 16 kHz. In this chapter, the important comparisons between unforced injection and pulsed injection at 16 kHz is presented. In addition to instantaneous and time averaged physics, performance metrics including jet penetration, species decay, and total pressure loss are presented.

6.2 Comparisons of Steady and Pulsed Injection

6.2.1 Instantaneous Results

A comparison of Mach number, hydrogen mole fraction and numerical schlieren contours between steady and pulsed injection can be seen in Figure 50. Mach number contours of the flow field between steady and forced injection reveal drastically different flow features both in the near field and further downstream of the injection location. The most notable different features between the cases are the large scale structures that are generated. The computational domain used in this study is large enough to capture four full jet pulse cycles; in Figure 50 four fluid slugs can be seen in the pulsed injection case. The Mach disk structures are very different between the steady and pulsed. For a pulse cycle time of $t/T = 0.75$, the instantaneous large scale structures in the shock wave are larger for pulse injection but they collapse within 1 *ms*.

Figure 50b-c shows instantaneous images of hydrogen mole fraction and numerical schlieren for both pulsed and unforced cases. The mole fraction contours show that each pulsed fluid slug produces larger scale eddies which roll up and entrain ambient fluid into the jet and its wake. Also, steep gradients of mass between the jet core regions in each fluid slug suggest active mixing regions are present in the jet.

The major importance of larger vortical structures during pulsation include the increasing of the size of the interface between the jet and the crossflow during the pulse. The surface contact improvement (such as that suggested by Heiser [1]) is demonstrated to become improved for pulsed injection. Maximum penetration during the highest portion of the interface between the fluid slug and the free stream occurs downstream of the injection site ($x/D = 40$). It is evident that instantaneously, pulsed injection improves jet penetration. The numerical

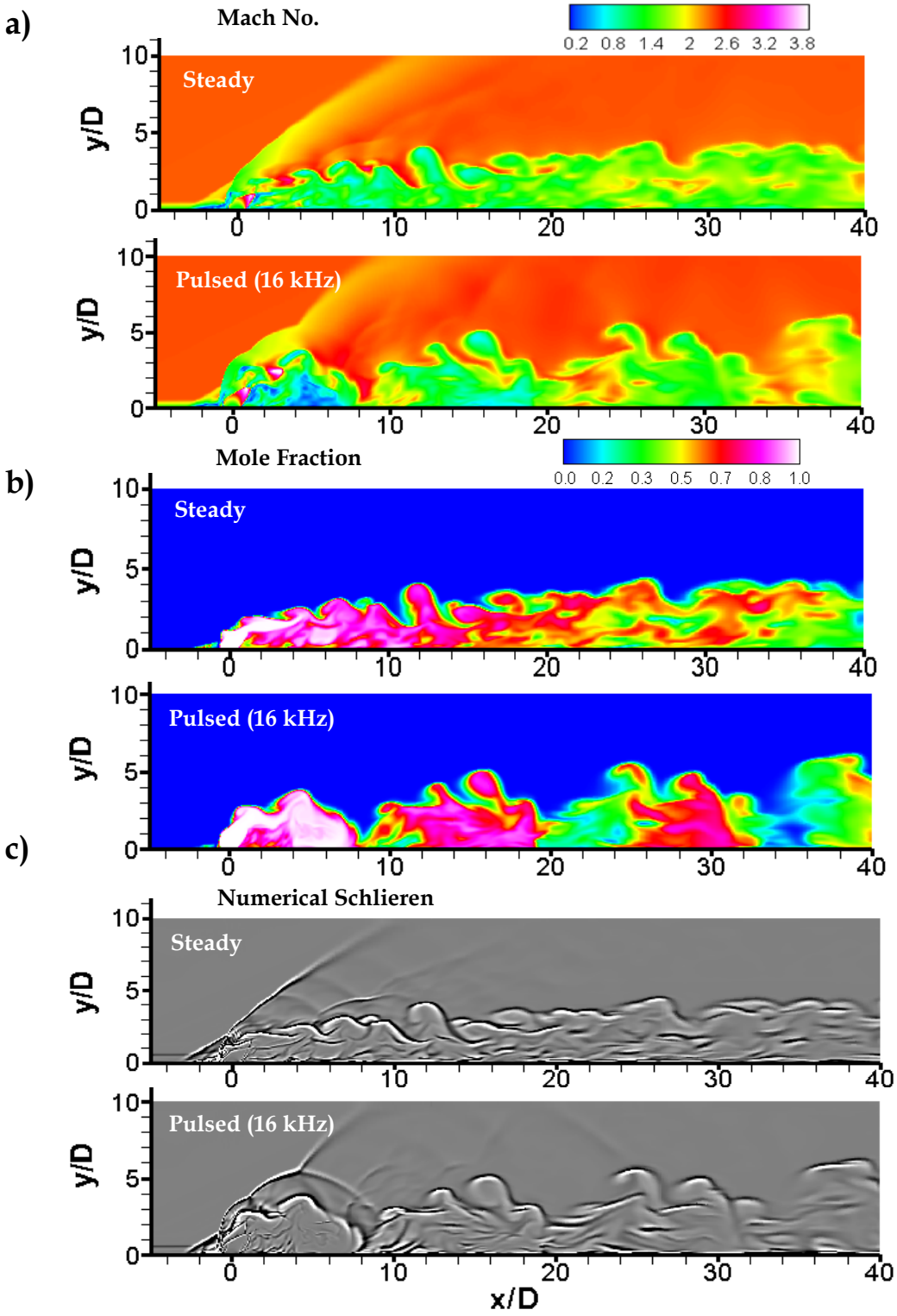


Figure 50: Comparison of steady (*J~1*) and pulsed injection (16 kHz) at (*t = 0.134 ms*). Contours shown are : (a) Mach number, (b) hydrogen mole fraction and (c) numerical schlieren. Pulse time is *t/T = 0.75*.

schlieren image shows the unsteady nature of the bow shock in comparison to the steady jet. Pulsation of the jet produces a continuously unsteady and thus an average weaker bow shock in comparison to the steady jet.

6.2.2 Time Averaged Results

Time averaged comparisons of hydrogen mass concentration and the RMS variation of species concentration are presented in Figure 51 for steady and pulsed injection. All contours are set to the same scale for consistent comparison. Several notable differences can be presented between the two cases. In the steady jet, the time averaged mass concentration shows greater local vertical penetration near the injector, but mostly horizontal direction. The pulsed mass concentration shows a lower peak concentration magnitude near the jet and in the far field but the time averaged jet boundary is higher than in the steady case.

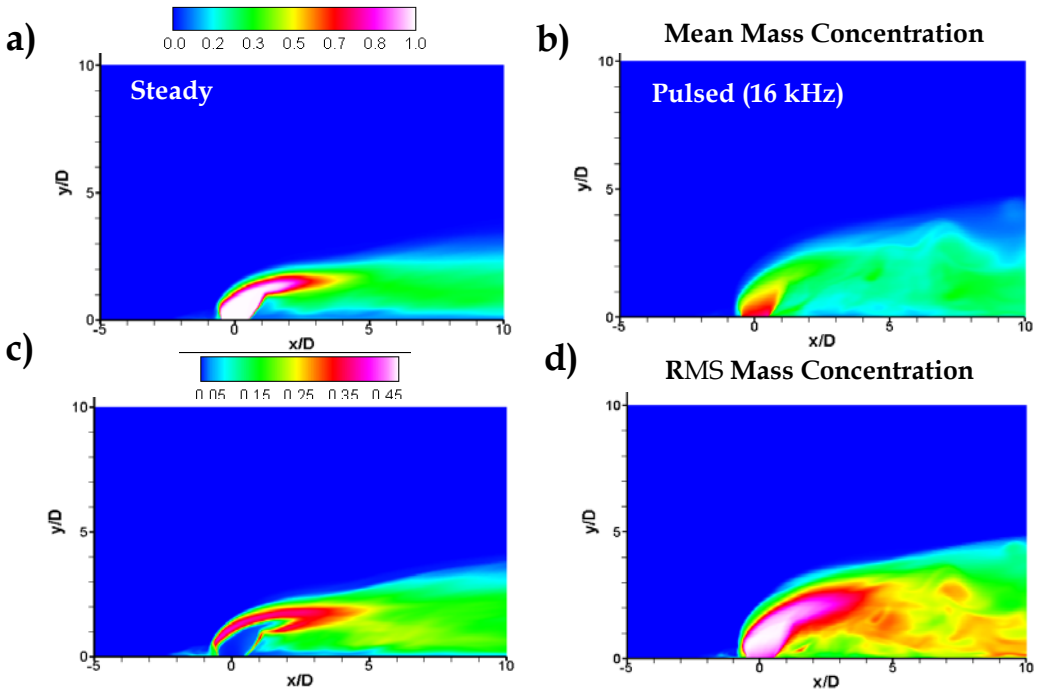


Figure 51: Time averaged comparison of hydrogen mass concentration (top) and RMS of mass concentration (bottom) for steady (a,c) and pulsed (b,d) injection.

The RMS values of the mass concentration also are very different where fluctuations in the hydrogen mass fraction are much higher in the pulsed jet case. The higher RMS mass concentration in the pulsed jet corresponds to large eddy transport of the fuel specie. For the steady jet, there is virtually no fluctuation in the barrel shock region. The most significant level fluctuations in the steady jet occur near above the barrel shock, extending from the windward side, above the Mach disk region and in the direction of the flow in the downstream direction. The RMS of the pulsed mass concentration shows fluctuation in the barrel shock, above the barrel shock and in the recirculation zone downstream of the injection site. In addition to the improved RMS fluctuations of the mass concentration, observing the RMS values of v-velocity also show differences between steady and pulsed

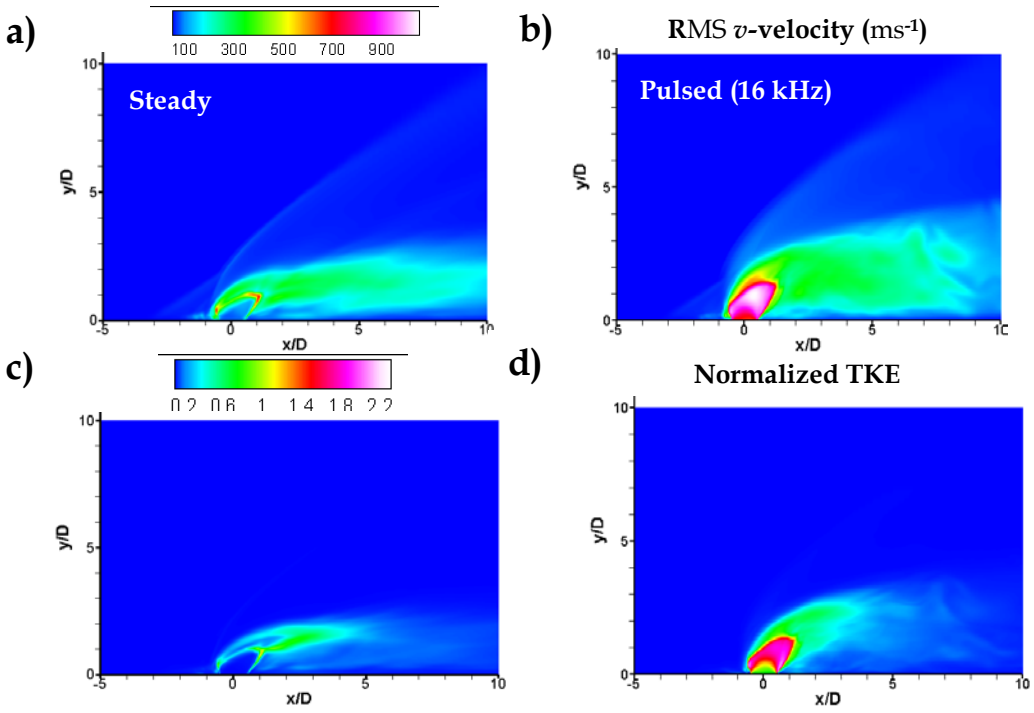


Figure 52: (Top): time averaged contours of RMS v-velocity for unforced and pulsed injection. (Bottom): turbulent kinetic energy (TKE) comparison between steady and pulsed injeection.

injection. The magnitude of maximum fluctuation of mass concentration in the pulsed jet is approximately 200% times that of the unforced jet.

In Figure 52 the differences between RMS v-velocity for the steady and pulsed injection are dramatically different also. The RMS v-velocity of the steady jet peaks near the location upstream of the barrel shock and immediately above the Mach disk. These regions experiences the most fluctuation of the unforced jet, resulting in self-sustained oscillations which are commonly present in jets which are not externally excited.

The jet boundary of the pulsed jet in the v-velocity direction is more pronounced, significantly improving the near field penetration. The barrel shock region drastically fluctuations, reaching peak RMS v-velocities of approximately 1000 m/s. The peak fluctuation magnitude for the pulsed jet is up to 300% in the barrel shock and Mach disk regions. The RMS v-velocity differences between steady and pulsed injection were also visible in terms of turbulent kinetic energy distributions (Figure 52c-d). The distribution of turbulent kinetic energy is increased in the pulsed jet in comparison to the steady jet. Pulsed jet TKE peaks in the barrel shock region as well as the re-circulation zone behind the barrel shock. This suggest a significant improvement in the dilation regions of the jet periphery surrounding the injection site. The study of the time averaged images presented here generally suggest that pulsation of the jet improves the spread by larger eddy and turbulent structures of the regions available for fuel-air mixing which has significant implications on improving scramjet fuel performance.

6.3 Performance Comparisons

From the instantaneous and time averaged data created by the WMLES numerical model constructed in this study it is evident that excitation of a fuel jet in a supersonic crossflow significantly changes the flow field both in the near field

and far field locations. Primarily, the penetration and mixing of the jet are improved by pulsation, including an increase in regions of localized mixing. It is helpful to compare this data on trajectory plots.

Figure 53 shows a comparison of the trajectories of the forced and unforced jets, based on the time averaged mass concentration profiles, taken at various locations in the computational domain and based on the 10% $\bar{Y}_{max}$ location. The trajectory results from Figure 53 suggest that pulsation improves both near field and far field penetration when compared with unforced injection. The lower plot in Figure 53 shows the penetration improvement factor (PIF) plotted against axial location. PIF is defined as the ratio of the pulsed to steady injection trajectories. The PIF values show that improvement is most dramatic in the near field ($x/D < 10$) and drops of exponentially until about ($x/D = 25$) where it has a near

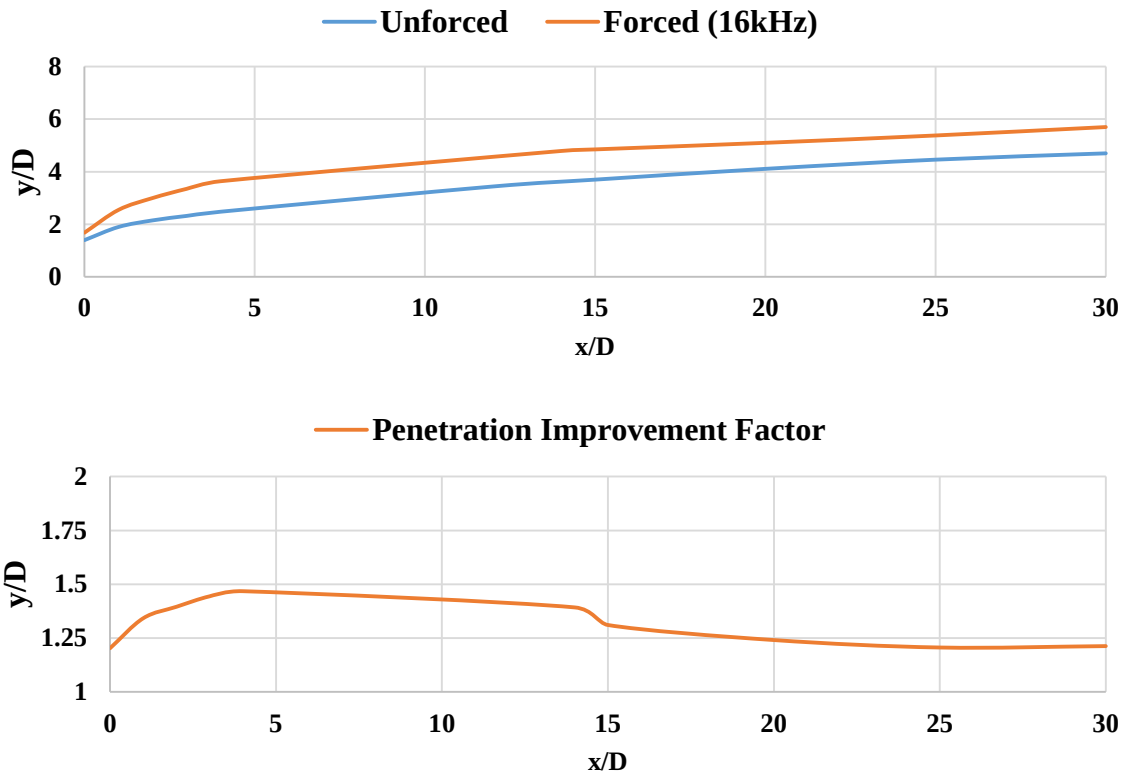


Figure 53: Top image: trajectory comparison between steady and pulsed injection cases. Bottom image: penetration improvement factor (PIF) trajectory.

horizontal slope. The peak PIF value is about 1.5, near $x/D = 5$, suggesting that in the near field, pulsation of the jet improves penetration in comparison with an unforced jet by 50%. The improved penetration in the far field isn't nearly as dramatic, leveling out at around 25%, measured at $x/D = 30$. Figure 54 shows a comparison of the mass concentration decay for steady and pulsed injection.

Maximum values of mean mass concentration profiles ($\bar{Y}_{max}$) were taken at several locations using the line/rake function in ANSYS FLUENT. The results indicate that the pulsation of the jet causes the fuel concentration to decay at a faster rate than for an unforced case. The decay of mass concentration is a direct measure of jet mixing. The drastic drop off is even more pronounced in the near field ($x/D < 5$) than further downstream, which suggests that if a turbulent flow can be sustained near its fuel injector, it will be hotter (with a higher equivalence ratio) than for the equivalent steady jet case.

This is consistent with the RMS mass concentration contours in Sec. 6.2 which showed higher fluctuations in the pulsed jet near field. The suggested mixing improvement favors pulsed injection both in the near field; however, in the far field beyond $x/D = 20$, the mixing mass concentration decay rate levels off. Thus mixing enhancement is only significantly improved in the near field.

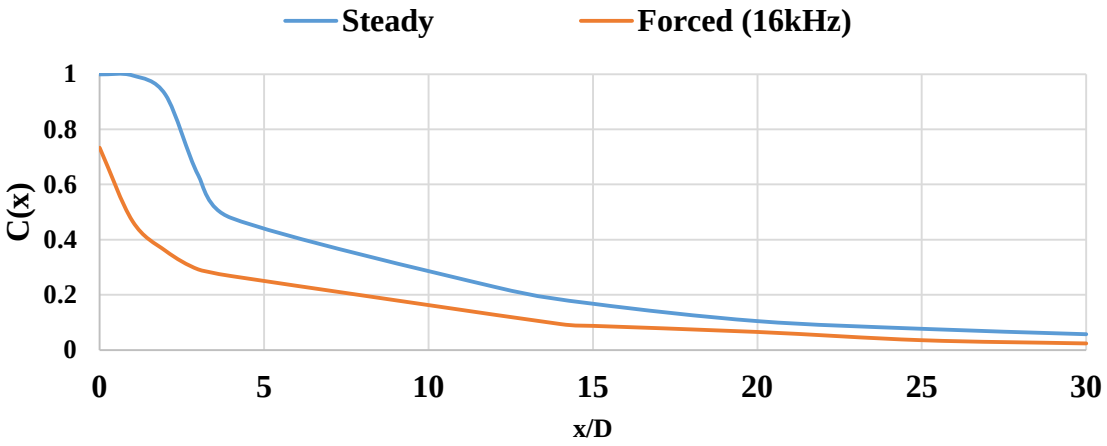


Figure 54: Mass concentration decay plots comparing steady and pulsed cases.

Figure 55 shows time averaged total pressure profiles for both continuous and pulsed injection obtained using the ANSYS FLUENT line/rake function. Sample data was taken from locations (x/D) of 10, 30, and 40. Total pressure is normalized by the free stream total pressure, (P_{tc} = 30 psi). It is evident that pulsation of the jet does not improve total pressure recovery in the near field. At $x/D = 10$, the drop off in total pressure is greater during in the pulsed jet trajectory. However, as the jet moves downstream of the injector location, the overall total pressure recovery improves for the pulsed jet. At $x/D = 20$, the total pressure recovery is approximately the same as in the continuous case.

In the far field $x/D = 40$, the total pressure recovery still is higher for the pulsed case, except in the region above which the pulsed jet penetrates deeper than the unforced jet at $y/D > 0.75$. Outside of this region the decrease in total pressure insignificant.

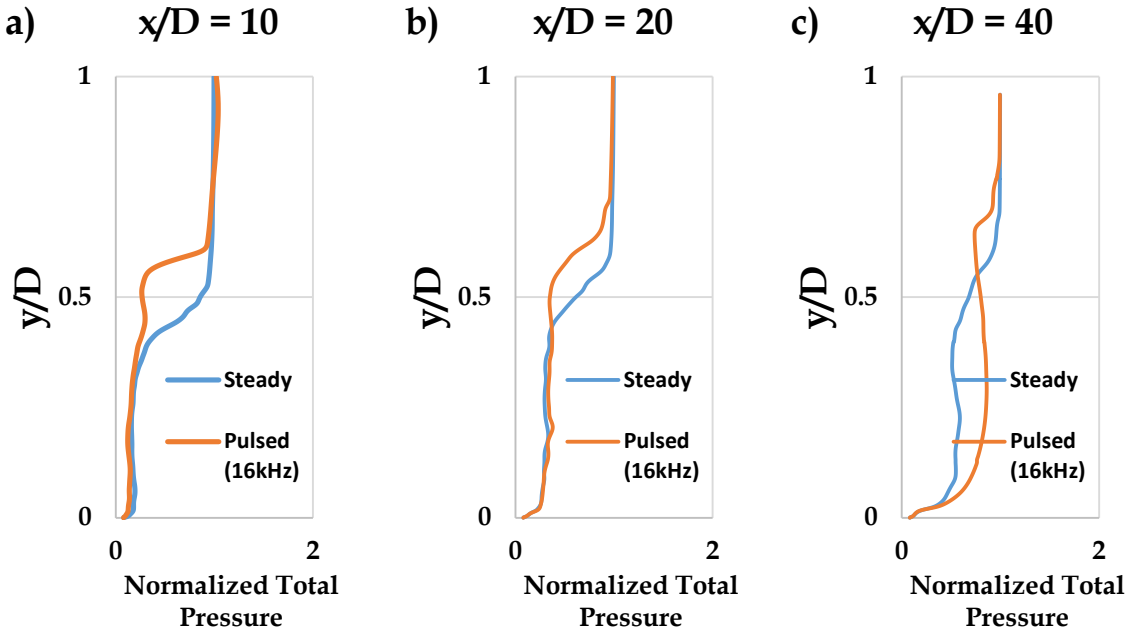


Figure 55: Comparison of time averaged total pressure profiles for steady and pulsed injection: (a) *x/D = 10*, (b) *x/D =20* and (c) *x/D = 40*. Total pressure is normalized by the free stream value (P_{tc} = *30 psi*).

The results presented suggest that in the far field, beyond $x/D = 10$, pulsed injection does improve total pressure recovery over an unforced jet. A consideration for future investigations might include a mass averaged total pressure recovery. This would allow for a more direct comparison between how much total pressure is lost to the jet as a result of pulsation when compared to steady injection.

Also, it must be noted that the term "total pressure recovery" is a misnomer though it is often used in literature. "Total pressure recovery" as it is used here actually refers to "total pressure loss efficiency". The goal is to keep the total pressure in the jet as close to the free stream value as is possible. The results presented here suggest that pulsation of the jet is more "total pressure loss efficient" in the jet far field than it is near the wall injector or the near field.

6.4 Implications

Thus far, the discussion of results in this study has focused on the jet penetration, mixing and total pressure recovery of unforced and pulsed jets in supersonic crossflows assuming a single injector in which the cycle averaged mass flow rate of the pulsed jet matches the instantaneous injector flow rate condition. However, in real supersonic combustors, other performance characteristics of fuel delivery systems include flame holding capability and flammability limits (i.e. a measure of where combustion will occur relative to stoichiometric properties).

In steady jets, the recirculation zones upstream and downstream of the injection site are generally stable and act as recirculation zones. Figure 56 shows results presented in this study which indicate improved instantaneous recirculation zones and higher RMS mass concentration spread for pulsed injection. Generally, these are promising results, since the localized recirculation zones theoretically should promote increased mixing rates and thus improve the

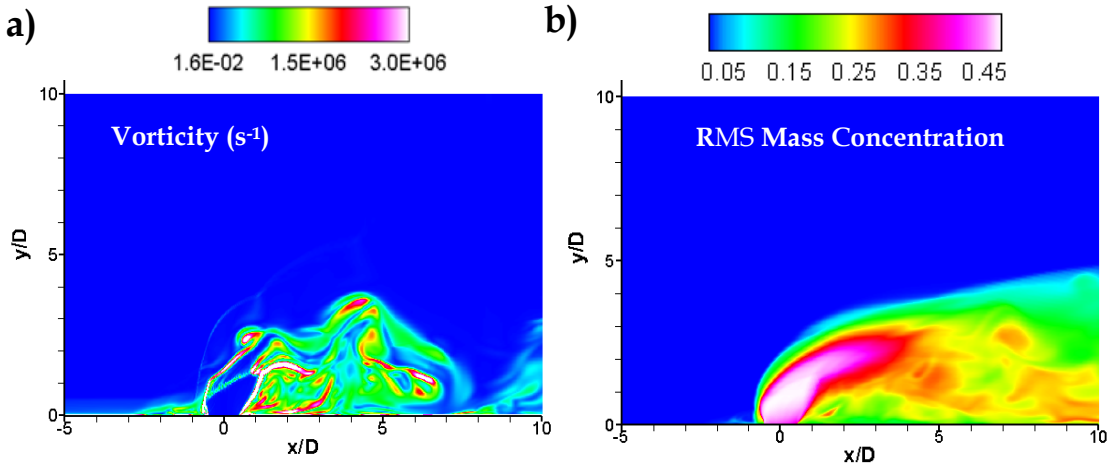


Figure 56: Contours of instantaneous vorticity (a) and RMS hydrogen mass concetration (b) for pulsed injection displaying large regions of reciculation downwind of the wall injector

residence time of the air-fuel mixture during a pulsation stroke. However, there are also potential draw backs of jet pulsation on mixing.

A simple analysis of the flame propagation speed (S_L) might present a description of how flame characteristics might be affected by high frequency pulsation. Assuming the pulsed fluid slug moves at free stream velocity of 556 m/s at Mach 2.3 (with p_1 = 2.4 psia and T_1 =145 K) one could compare the speed of the fluid slug with the flame propagation speed. Kuo gives suggested values of flame speeds based on laminar and turbulent flow conditions [124]. For brevity, the laminar flame speed is assumed, corresponding to a flame temperature (T_f = 1873). Thus, the flame speed is (S_L = 0.16 m/s). A pulsed jet at the current simulation conditions would quickly blow the flame out! Therefore, it is clear that pulsed injection schemes must require some type of localized flame holding devices or other mechanisms to reignite the flames burning around the pulsed jet during all phases a pulse cycle.

Figure 57 shows mole fractions at an instant in time at axial stations ($x/D = 10, 20$) for both unforced and pulsed cases. The slices are taken at two locations where the pulsed slug was near maximum penetration. Glassman and

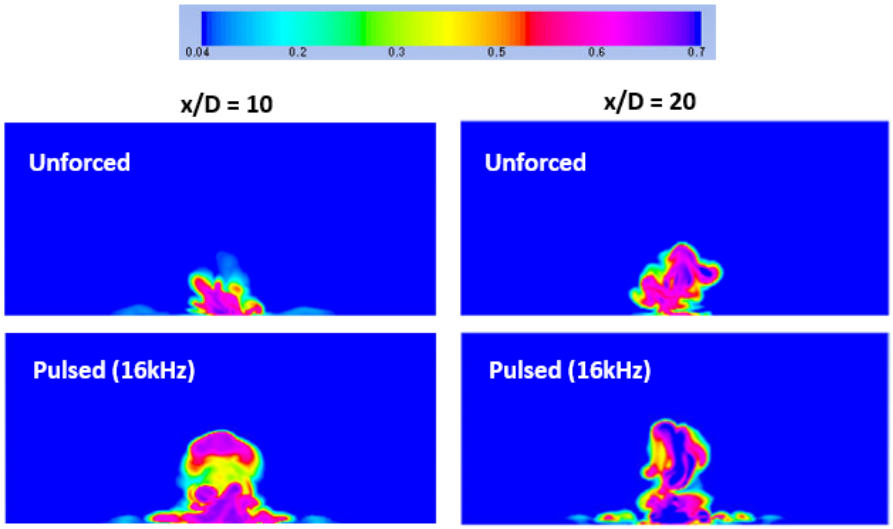


Figure 57: Comparison of instantaneous (t = 0.3 ms) mole fraction contours displaying the flammability limits of hydrogen for steady and pulsed injection at axial locations x/D = 10 and 20.

Yetter [125] provide suggested ranges of the flammability limits in air for various fuels. For hydrogen, the lean limit and rich limits (based on mole fraction by volume %) are 4.0 and 0.75. Contours limited in these ranges are presented in Figure 57. The regions where no combustion would occur are marked in dark blue (beyond the lower limit) and dark purple (beyond the upper limit).

The results suggest that pulsation improves the surface contact area (and thus increases the mixing zones) above an unforced jet. Also, each pulse slug drags along a region of horseshoe vortices in the jet periphery near the wall, improving the potential combustion zones in comparison with unforced injection. Based on the results presented, pulsed jet injection appears to have the potential to improve fuel distribution and mixing in high speed supersonic combustion engines but flame holding and ignition will most likely be required. Much further investigation is needed to confirm these results, including wind tunnel experiments and the development of high frequency pulsed fuel injectors.

7 Conclusions and Future Work

7.1 Primary Investigation Summary

A 3D SRS computational model using a wall-modelled Large Eddy Simulation approach was used to investigate the primary effects of high frequency gaseous hydrogen pulsed fuel jet injection into a supersonic crossflow. The focus of the study was limited to cold flow conditions which ignore the effects of combustion. A literature review was conducted which describes major studies of the physics of JISF and various approaches to improve the penetration, mixing and pressure recovery performance of fuel injection in scramjet engines.

Further investigation from the literature review indicated that pulsed jet injection was a good candidate for fuel injection performance improvement and guided the direction of this study. Pulsed injection potentially provides a minimally-intrusive fuel delivery mechanism which does not reduce the normal flow direction momentum, but still improves penetration into the core flow. The lack of extensive quantitative and qualitative data suggested that a detailed study on the effects of pulsed injection in supersonic crossflows was a promising area to focus research.

To build off previous theory and work related to PJISF, 2D and 3D models of a sinusoidal pulsed injection of a gaseous hydrogen fuel jet into a supersonic flow

for a low cycle averaged momentum flux ratio ($J \approx 1$) at frequencies in the kHz range was presented. Steady injection cases were also modeled to compare the effects of pulsation to those without external excitation. The study relied on conducting computational fluid dynamics analysis using the ANSYS FLUENT computational tool. The 3D model used a wall-modeled Large Eddy Simulation approach to the turbulence description of the fluid phenomena. The main flow field variables which were computed demonstrated reasonable agreement with 1D compressible theory for the steady 3D case. Results demonstrated improved penetration and mixing in pulsed injection, with far field total pressure efficiency improvement over unforced injection.

7.2 Primary Accomplishments and Conclusions

At the start of this study, specific research questions were asked, with implications to research contributions. The research questions focused on jet penetration improvement, mixing improvement and total pressure recovery. Also, investigation of fluid phenomena mentioned in literature (e.g. Mach disk behavior over a pulsation cycle and the pulsed jet regime map proposed by Sau and Mahesh) are also addressed [70].

The results presented in this study suggest that when the cycle averaged total pressure is matched with the injectant total pressure of a steady jet, sinusoidal pulsation at 16 kHz improves overall jet penetration; peak penetration improvement reached a maximum penetration improvement factor (PIF) of up to 50% in the near field ($x/D \approx 5$). The mixing rate near the wall jet injector region is also improved as a result of pulsed injection. Along the length of the jet, pulsation increases species decay rates in the near field ($x/D < 10$). In the far field the improvement is less appreciable. Total pressure recovery is less however for the pulsed jet in comparison to the steady jet. For ($x/D < 10$), the total pressure is lost at a higher rate for pulsed injection. However, outside of the neat field ($x/D > 10$)

total pressure performance is improved over steady injection. Future studies should focus on observing mass averaged total pressure loss efficiency when comparing steady and pulsed jet injection.

Randolph [55] suggested that pulsed injection into a supersonic crossflow would occur on such small time scales that jet losses associated with the Mach disk formation could be avoided. Specifically, the highly impulsive fluid slug would form and penetrate so rapidly that the shock formation would not occur at all, thus producing improvement of penetration performance. The results presented in this study disproves this hypothesis. At 16 kHz, the Mach disk formation is almost instantaneous, forming weakly around the downstream injectant periphery as soon as the injector chokes and produces an under-expanded jet. The Mach disk formation was shown to occur on the order of time scale $t_f << 1\mu sec$.

Pulsation at high frequencies with ($J_{cycle} \leq 1$) produce turbulent puff-like structures instead of distinct vortex rings, for larger stroke ratios ($L/D = 18$). Thus it is demonstrated that even with a supersonic crossflow, for the case investigated, the pulsed regime map presented by Sau and Mahesh holds. Further investigation across a wider range of frequencies and cycle averaged momentum fluxes would improve confidence in these assertions.

The following bulleted summary describes the major research contributions in this study as was suggested in Chapter 1:

- A Large Eddy Simulation investigation of a pulsed jet in supersonic crossflow, which improves large scale structure description was conducted
- The hypothesized improvement of jet penetration, mixing and total pressure recovery (in the far field) of pulsed injection was investigated
- Physical description of the mechanisms of how increased large scale structures in pulsed jets improve mixing, and flammability performance was provided

- Comparison of the pulsed jet regime to supersonic crossflow conditions was made with confirmation

7.3 Suggested Future work and Research Direction

The first priority of future theoretical work should be investigation of a PJISF using an LES approach with the same inlet flow properties and jet properties as is investigated here but with a more powerful set of computational capabilities (e.g. faster machines with higher RAM). Some of the future points of investigation in such a study might include investigating a PJISF with a higher density computational grid while using higher order spatial and temporal accuracy. Furthermore, a detailed investigation of the total pressure loss efficiency using mass averaged total pressure integrated over the entire outflow region might provide extensive knowledge of whether or not jet injection total pressure efficiency can be improved by jet pulsation.

Experiments would include formation of a high speed mechanical device (similar to those proposed by Epstein [52]) which can operate at a wide range of frequencies in the kilohertz range. It should be noted that a limited number pulsed injection experiments have been carried out but none at the flow conditions specified in this study. Computational models can be improved to include higher number of grid points (over 20 – 40M cells) to further improve resolution of mixing. Also, the use of an unsteady turbulent velocity profile inlet condition to observe the effects of an unsteady turbulent boundary layer on pulsed injection is a crucial step in modeling scramjet engine inlet flow paths which use pulsed injection as a fuel deliver approach.

Other research investigations might include the study of how a heavier hydrocarbon (e.g. ethylene) might behave in pulsed jet injection conditions. Scramjets employing pulsed jet injection with a hydrocarbon gas might require

different frequency ranges to improve jet penetration and mixing than those presented in this study. Square pulse wave forms have been shown to improve jet penetration of pulsed subsonic jets over sinusoidal pulses. Numerical models showing improved penetration with square pulses over sinusoidal ones, or even sinusoidal pulsed injection with multiple frequencies might improve penetration characteristics.

Finally, since scramjets generally employ multiple wall injectors, it should be worth investigating the use of alternating pulsed injectors, perhaps operating out of phase by a half-cycle to keep mass flow going into the crossflow marginally fixing (but locally unsteady). Pulsed injection into supersonic crossflows for scramjet fuel performance has much potential. It is the hope of the author that this field of study will grow both experimentally and numerically and ultimately in real flight application.

List of References

[1] W. Heiser and D. Pratt, Hypersonic Airbreathing Propulsion, Los Angelos: AIAA Education Series, 1991.

[2] E. Curran and S. Murthy, Scramjet Propulsion (Progress in Aeronautics and Astronautics), AIAA, 2001.

[3] C. Segal, The Scramjet Engine: Process and Characteristics, 1st ed., Cambridge Aerospace Series, 2009.

[4] D. W. Bogdanoff, "Advanced Injection and Mixing Techniques for Scramjet Combustors," *Journal of Propulsion and Power,* vol. 10, no. 2, pp. 183-190, 1994.

[5] K. M. Pandey and T. Sivasakthiviel, "Recent Advances in Scramjet Fuel Injection- A Review," *International Journal of Chemical Engineering and Applications,* vol. 1, no. 4, pp. 294-301, 2010.

[6] J. M. Seiner and S. M. K. D. C. Dash, "Historical Survery of Enhanced Mixing in Scramjet Engines," *Journal of Propulsion and Power,* vol. 17, no. 6, pp. 1273-1286, 2001.

[7] A. Ben-Yakar and R. K. Hanson, "Cavity Flame-Holers for Ignition and Flame Stabilitzation in Scramjets: An Overview," *Journal of Propulsion and Power,* vol. 17, no. 4, pp. 869-877, 2001.

[8] M. M. V. M. M. Gamba, "Density Ratio and Velocity Ratio Effects on the Structure of Transverse Jets in Supersonic Crossflow," in *International Symposium on Turbulence and Shear Flow Phenomena*, Poiliers, France, 2013.

[9] J. Lee, K. Lin and D. Eklund, "Challenges in Fuel Injection for High Speed Propulsion Systems," *AIAA Journal,* vol. 53, no. 6, 2015.

[10] E. E. Zukoski and F. W. Spaid, "Secondary Injection of Gases into a Supersonic Flow," *AIAA Journal,* vol. 2, no. 10, pp. 1689-1696, 1964.

[11] J. A. Schetz and F. S. Billig, "Penetration of Gaseous Jets Injected into a Supersonic Stream," *Journal of Spacecraft,* vol. 3, no. 11, pp. 1658-1665, 1966.

[12] J. A. Schetz, P. F. Hawkins and H. Lehman, "Structure of Highly Underexpanded Transverse Jets in a Supersonic Stream," *AIAA Journal,* vol. 5, no. 5, pp. 882-884, 1966.

[13] J. T. C. Adamson and J. A. Nicholls, "On the Structure of Jets from Highly Underexpanded Nozzles into Still Air," *Journal of the Aerospace Sciences,* vol. 4, no. 1, pp. 68-71, 1959.

[14] S. Crist, P. M. Sherman and D. R. Glass, "Study of the Highly Underexpanded Sonic Jet," *AIAA Journal,* vol. 4, no. 1, pp. 66-71, 1966.

[15] R. C. Orth and J. A. Funk, "An Experimental and Comparative Study of Jet Penetration in Supersonic Flow," *Journal of Spacecraft,* vol. 4, no. 9, pp. 1236-1242, 1967.

[16] Ashkenaz and Sherman, Rarefied Gas Dynamics, New York: Academic, 1966.

[17] A. Ben-Yakar, M. Mungal and R. Hanson, "Time Evolution and Mixing Characteristics of Hydrogen and Ethylene Transverse Jets in Supersonic Crossflows," *Physics of Fluids,* 2006.

[18] R. Orth, S. J. and F. Billig, "The Interaction and Penetration of Gaseous Jets in Supersonic Crossflows," John Hopkins University, Washington, D.C., 1969.

[19] F. P. Povinelli, L. A. Povinelli and M. Hersch, "Supersonic Jet Penetration (up to Mach 4) into a Mach 2 Airstream," *Journal of Spacecraft,* no. August 1970, pp. 988-992, 1970.

[20] F. Billig, R. C. Orth and M. Lasky, "A Unified Analysis of Gaseous Jet Penetration," *AIAA Journal,* vol. 9, no. 6, pp. 1048-1058, 1971.

[21] G. N. Abramovich, The Theory of Turbulent Jets, Cambridge, MA: Massachusetts Institute of Technology Press, 1963.

[22] D. Papamoschou and D. Hubbard, "Visual Observations of Supersonic Transverse Jets," Experiments in Fluids, Irvine, 1993.

[23] M. Gruber, N. A. S., T. Chen and J. Dutton, "Mixing and Penetration Studies of Sonic Jets in a Mach 2 Freestream," *Journal of Propulsion and Power,* vol. 11, no. 2, pp. 315-324, 1995.

[24] M. Gamba, V. Terrapon, A. Saghafian, M. Mungal and H. Pitsch, "Assessment of the Combustion Characteristics of Hyrdogen Transverse Jets in Supersonic Crossflow," *Center for Turbulence Research Annual Research Briefs,* 2011.

[25] B. Pratte and W. Baines, "Profiles of the Round Turbulent Jet in a Crossflow," *Journal of Hydrodynamics,* 1967.

[26] Sau, 2004.

[27] K. Mahesh, "The Interaction of Jets with Crossflow," *Annual Review of Fluid Mechanics,* vol. 45, pp. 379-407, January 2013.

[28] D. Papamoschou and A. Roshko, "The Compressible Turbulent Shear Layer: An experimental Study," *Journal of Fluid Mechanics,* vol. 197, pp. 453-477, 1988.

[29] P. Dimotakis, Turbulent Mixing, 1977.

[30] D. Liscinsky and M. Holdeman, "Crossflow mixing of noncircular jets," *AIAA,* 1995.

[31] V. Kopchenov and K. and Lomkov, "The enhancement of the mixing and combustion processes applied to scramjet engines," *AIAA,* 1992.

[32] L. Maddelena, J. Schetz and R. Neel, "Vortical Interactions with a Jet in a Supersonic Crossflow," in *46th AIAA Aerospace Sciences Meeting and Exhibit*, Reno, 2008.

[33] P. King, R. Thomas and J. Schetz, "Combined Tangential-Normal Injection Into a Supersonic Flow," in *Aerospace Sciences Meeting*, Reno, 1989.

[34] J. P. Drummond, M. Carpenter, D. Riggins and M. Adams, "Mixing Enhancement in a Supersonic Combustor," AIAA, Hampton, VA, 1989.

[35] A. Karagozian, K. Wang, A. Le and O. Smith, "Transverse Gas Jet Injection Behind a Rearward Facing Step," *Journal of Propulsion and Power,* vol. 12, no. 6, 1996.

[36] L. Cohen, L. Coulter and J. W. Egan, "Penetration and Mixing of Multiple Gas Jets Subjected to a Crossflow," *AIAA Journal,* vol. 9, no. 4, June 1970.

[37] S. Lee, "Characteristics of Dual Transverse Injection in Scramjet Combustor, Part 1: Mixing," *Journal of Propulsion and Power,* vol. 22, no. 5, October 2006.

[38] H. Ebrahimi, F. Malo-Molina and D. Gaitonde, "Numerical Simulaiton of Injection Strategies in a Cavity-Based Supersonic Combustor," *Journal of Propulsion and Power,* vol. 28, no. 5, pp. 991-999, 2012.

[39] R. Gosse, R. Kimmel and H. Johnson, "CFD Study of the HIFiRE-5 Flight Experiment," in *40th Fluid Dynamics Conference and Exhibit*, Chicago, 2010.

[40] A. Saghafian, L. Shunn, D. Philips and F. Ham, "Large Eddy Simulations of the HIFiRE Scramjet using a Compressible Flamelet/Progress Variable Approach," in *Proceedings of the Combustion Institute*, Palo Alto, 2015.

[41] T. Juliano, D. Adamczak and R. Kimmel, "HIFiRE-5 Test Results," *Journal of Spacecraft and Rockets,* vol. 52, no. 3, pp. 650-663, 2015.

[42] H. Viets, "Flip-Flop Jet Nozzle," *AIAA Journal,* vol. 13, no. 10, pp. 1375-1379, 1979.

[43] M. Narayanan, "Behavior of Excited Jets," *Sadhana,* vol. 12, no. 2, pp. 31-43, 1988.

[44] J. C. Hermanson, A. Wahba and H. Johari, "Duty-Cycle Effects on Penetration of Fully Modulated, Turbulent Jets in Crossflow," *AIAA Journal,* vol. 36, no. 10, pp. 1935-1937, 1998.

[45] S. Crow and F. Champaign, "Orderly structure in jet turbulence," *Journal of FLuid Mechanics,* vol. 48, no. 3, pp. 547-591, 1971.

[46] P. Vermeulen, C. Ching-Fatt and W. Yu, "Mixing of an Acoustically Pulsed Air Jet with a Confined Crossflow," *Journal of Propulsion,* vol. 6, no. 6, 1990.

[47] R. M'Closkey, M. King, L. Cortelezzi and A. Karagozian, "The Actively Controlled Jet in Crossflow," *Journal of Fluid Mechancs,* vol. 452, pp. 325-355, 2002.

[48] A. K. J. Shapiro, A. Karagozian and R. M'Closkey, "Optimization of Contrelled Jets in Crossflow," in *41st AIAA Aerospace Sciences Meeting and Exhibit*, Reno, NV, 2003.

[49] B. Eroglu, "Structure, Penetration, and Mixing of Pulsed Jets in Crossflow," *AIAA Journal,* vol. 39, no. 3, 2001.

[50] H. Johari, "Scaling of Fully Pulsed Jets in Crossflow," *AIAA Journal,* vol. 44, no. 11, 2006.

[51] M. Dziuba and T. Rossmann, "Super Sonic Mixing Enhancement by means of High Powered Jet Modulation," in *44th AIAA Aerospace Sciences Meeting and Exhibit*, Reno, NV, 2006.

[52] M. J. Epstein, W. Chester and J. P. H. Kutschenreuter, "Fuel Injection System for Scramjet Engines," United States Patent Office 5,280,705, Washington, DC, 1994.

[53] A. D. Cutler, G. C. Harding and G. S. Diskin, "High Frequency Pulsed Injection into a Supersonic Duct Flow," *AIAA Journal,* pp. 1-9, 2012.

[54] T. Kouichi, K. Sasaya, J. Watanabe, H. Sibayama and G. Masuya, "Penetration Characteristics of Pulsed Injection into Supersonic Crossflow," in *46th AIAA/ASME/SAE/ASEE Joint Propulsion Conference & Exhibit*, Nashville, TN, 2010.

[55] H. Randolph, L. Chew and H. Johari, "Pulsed Jets in Supersonic Crossflows," *Journal of Propulsion and Power,* vol. 10, no. 5, pp. 746-748, 1994.

[56] A. D. Vakili and J. M. Wu, "Scramjet Combustion Mixing Improvements Using Pulsed Transverse Jets," ONR Grant/Navy N00014-89-J-1696, Tullahoma, TN, 1995.

[57] K. H. Yu, K. J. Wilson and K. C. Schadow, "Effect of flame-holding cavities on supersonic-combustion performance," *Journal of Propulsion and Power,* vol. 17, no. 6, pp. 1287-1295, 2001.

[58] S. Murugappan, E. Gutmark and C. Carter, "Control of penetration and mixing of an excited supersonic jet into a supersonic cross stream," *Physics of Fluids,* vol. 17, 2005.

[59] T. Kouchi, N. Sakuranaka, M. Izumikawa and S. Tomioka, "Pulsed Transverse Injection Applied to a Supersonic Crossflow," in *43rd AIAA/ASME/SAE/ASEE Joint Propulsion Conference & Exhibit*, Cincinnati, 2007.

[60] E. Binder, D. Miller, B. Smith and P. Yagle, "Simulation of Pulsed Injection in a Cross Flow using 3-D Unsteady CFD," in *Fluids 2000*, Denver, 2000.

[61] K. Shapiro, J. King, A. Karagozian and R. M'Closkey, "Optimization of Controlled Jets in Crossflow," in *41st AIAA Aerospace Sciences Meeting and Exhibit*, Reno, 2003.

[62] A. Glezer and M. Amitay, "Synthetic Jets," *Annual Review of Fluid Mechanics,* 2002.

[63] S. Lardeau and M. Leschziner, "The Interaction of Round Synthetic Jets with a Turbulent Boundary Layer Separating from a Rounded Ramp," *Journal of Fluid Mechanics,* vol. 683, pp. 172-211, 2011.

[64] M. Gharib, E. Rambod and K. Shariff, "A Universal Time Scale for Vortex Ring Formation," *Journal of Fluid Mechanics,* vol. 360, pp. 121-140, 1998.

[65] R. Sau, "Control of Jets in Crossflow using Direct Numerical Simulations," Doctoral Dissertation, Chicago, 2010.

[66] M. Gharib, *Optimal Vortex Formation as a Unifying Principle in Biological Propulsion,* California Institute of Technology, 2004.

[67] K. Mohensi and M. Gharib, "A model for universal time scale of vortex ring formulation," *Physics of Fluids,* vol. 10, no. 10, 1998.

[68] I. Sullivan, J. Niemela, R. Hershberger, D. Bolster and R. Donnelly, "Dynamics of thin vortex rings," *Journal of Fluid Mechanics,* vol. 609, pp. 319-347, 2008.

[69] R. Sau and K. Mahesh, "Optimization of Pulsed Jets in Crossflow," *Journal of Fluid Mechanics,* vol. 653, pp. 365-390, 2010.

[70] K. Sau and K. Mahesh, "Dynamics and Mixing of Vortex Rings in Crossflows," *Journal of Fluid Mechanics,* vol. 604, pp. 389-409, 2008.

[71] A. D. Vakili, Y. K. Chang and J. M. Wu, "Supersonic Mixing Enhancement Using Pulsed Transverse Fuel Jets," ONR Grant Navy N0014-89-J-1696, Tullahoma, TN, 1995.

[72] R. Pasumarti, J. Schulz, J. Seitzman, J. Jagoda and S. Menon, "Large Eddy Simulaiton of Pulsed Jets in High Speed Turbulent Crossflow," in *48th AIAA Aerospace Sciences Meeting*, Orlando, FL, 2010.

[73] A. Glezer and A. Cole, *Dynamics of Vortex Rings.*

[74] S. Kawai and S. Lele, "Large-eddy simulation of jet mixing in a supersonic turbulent crossflow," *Conference for Turbulence Research,* 2008.

[75] C. Gibson, "Introduction to Turbulent Flow and Mixing," in *Fundamentals of Fluid Mechanics*, New York, John Wiley and Sons, Inc., 1999, pp. 83-85.

[76] H. Versteeg and H. Malalasekra, An Introduction to Computational Fluid Dynamics, 2nd ed., New Delhi: Pearson, 2007.

[77] P. Dimotakis, "The mixing transition in turbulent flows," *Journal of Fluid Mechanics,* vol. 409, pp. 96-98, 2000.

[78] A. Kolmogorov, ""The Local Structure of Turbulence in Incompressible Viscous Fluid for Very Large Reynolds Numbers"," *Dokl. Akad. Nauk SSSR,* vol. 30, pp. 301-305, 1941.

[79] S. Pope, Turbulent Flows, Cambridge: University Press, 2000.

[80] D. Wilcox, Turbulent Modeling for CFD, Palm Drive: DCD Industries, 1994.

[81] F. Menter, "Best Practice: Scale-Resolving Simulations in ANSYS CFD," ANSYS, Inc, 2012.

[82] J. Tannehill, D. Anderson and R. Pletcher, Computational Fluid Mechanics and Heat Transfer, 2nd ed., Washington D.C.: Taylor and Francis, 2010.

[83] Garnier, "Large Eddy Simulation Theory," *Journal of Computational Physics,* 2011.

[84] B. Vremen, B. Geurts and H. Kuerten, "Subgrid-Modelling in LES Compressible Flow," *Applied Scientific Research,* vol. 54, pp. 191-203, 1995.

[85] F. Menter, "Two-Equation Eddy-Viscosity Turbulence Models for Engineering Applications," *AIAA Journal,* vol. 32, no. 8, 1994.

[86] M. Shur, P. Spalart, M. Strelets and A. Travin, "A hybrid RANS-LES approach with delayed-DES and wall-modelled LES capabilities," *International Journal of Heat and Fluid Flow,* vol. 29, pp. 1638-1649, 2008.

[87] U. Piomelli and E. Balaras, "Wall-layer models for large-eddy simulations," *Annual Review of Fluid Mechanics,* vol. 34, pp. 349-374, 2002.

[88] J. Smagorinsky, "General Circulation Experiments with the Primitive Equations I: The Basic Experiment," *Mon. Weather Rev.,* vol. 91, pp. 99-164, 1963.

[89] D. Lily, "On application of the Eddy Viscosity Concept in the Inertial Subrange of Turbulence," NCAR , 1966.

[90] P. Spalart, W. Jou, M. Strelets and S. Allmaras, "Comments on the Feasibility of LES for Wings, and on a Hybrid RANS/LES Appraoch," in *Proceedings of the 1st AFOSR International Conference on DNS/LES*, Columbus, 1997.

[91] M. Strelets, "Detached eddy simulation of massively separated flows," *AIAA Journal,* 2001.

[92] F. Menter and M. Kunz, "Adaption of Eddy-Viscosity Turbulence Model to Unsteady Separated Flow Behind Vehicles," in *Symposium on the Aerodynamics of Heavy Vehicles: Trucks, Buses and Trains*, 2002.

[93] P. Spalart, S. Deck, M. Shur, K. Squires, M. Strelets and A. Travin, "A New Version of Detached-Eddy Simulation, Resistant to Ambiguous Grid Densities," *Journal of Theoretical and Computational Fluid Dynamics,* vol. 20, no. 3, pp. 181-195, 2006.

[94] ANSYS, "ANSYS FLUENT Theory Guide R15," ANSYS Inc, 2012, 2015.

[95] T. Barth and D. Jespersen, "The design and application of upwind schemes on unstructured meshes," AIAA, Reno, 1989.

[96] D. Holmes and S. Connell, "Solution of the 2D Navier-Stokes Equations on Unstructured Adaptive Grids," in *AIAA 9th Computational Fluid Dynamics Conference*, 1989.

[97] R. Rauch, J. Batira and N. Yang, "Spatial Adaption Procedures on Unstructured Meshes for Accurate Unsteady Aerodynamic Flow Computations," AIAA, 1991.

[98] R. Levesque, Finite Volume Methods for Hyperbolic Problems, New York: Cambridge University Press, 2002.

[99] R. Rogers, "Mixing of Hydrogen Injected From Multiple Injectors Normal to a Supersonic Airstream," NASA , Langley, 1971.

[100] M. Hersch, L. Povinelli and F. Povinelli, "Optical Study of Sonic and Supersonic Jet Penetration From a Flat Plate into a Mach 2 Airstream," NASA, Cleveland, 1970.

[101] C. McClinton, "The Effect of Injection Angle on the Interaction Between Sonic Secondary Jets and a Supersonic Free Stream," NASA, Langley, 1972.

[102] Y. You, H. Ludeke and K. Hannemann, "On the flow physics of a low momentum flux ratio jet in a supersonic turbulent crossflow," *Europhysics Lectures,* vol. 97, no. 2, pp. 1-6, 2012.

[103] D. Cecere, A. Ingenito, E. Giacomazzi, L. Romagnosi and C. Bruno, "Hydrogen/air supersonic combustion for future hypersonic vehicles," *International Journal of Hydrogen Energy,* vol. 36, pp. 11969-11984, 2011.

[104] M. Smart, N. E. Hass and A. Paull, "Flight Data Analysis of the HyShot 2 Scramjet Flight Experiment," *AIAA,* vol. 44, no. 10, pp. 2366-2375, 2006.

[105] N. Williams and T. Moeller, "Preliminary Investigations of Pulsed Fuel Injection into Supersonic Crossflows," in *Aviation 2015*, Dallas, TX, 2015.

[106] S. Karl, K. Hannemann, J. Steelant and A. Mack, "CFD Analysis of HyShot Supersonic Combustion Flight Experiment Configuration," in *14th AIAA/AHI Space Planes and Hypersonic Systems and Technologies Conference*, 2006.

[107] W. Huang, J. Yang and L. Yan, "Multi-objective design optimization of the transverse gaseous jet in supersonic flows," *Acta Astronautica,* vol. 93, pp. 12-22, 2014.

[108] A. Ferrante, G. Matheou and P. Dimtakis, "LES of an inclined sonic jet into a turbulent crossflow at Mach 3.6," *Journal of Turbulence,* vol. 12, no. 2, pp. 1-13, 2010.

[109] J. Watanabe, T. Kouchi, K. Takita and G. Masuya, "Numerical Study on the Turbulent Structure of Transverse Jets into Supersonic Flow," *AIAA Journal,* vol. 49, no. 9, 2011.

[110] D. Candler and D. Peterson, *Numerical Jet in Supersonic Crossflow,* 2011.

[111] E. Hassan, H. Aono, J. Boles, D. Davis and W. Shyy, "Multi-Scale Turbulence Model in Simulation of Supersonic Crossflow," in *49th AiAA Aerospace Sciences Meeting*, Orlando, 2011.

[112] X. Chai and K. Mahesh, "Simulations of High Speed Turbulent Jets in Crossflow," in *40th Fluid Dynamics Conference and Exhibit*, 2010, 2010.

[113] W. Vickery and H. Iacovides, "Computation of Gas Turbune Blade Film Cooling," Manchester, UK, 2015.

[114] J. DeSpirito, K. Kennedy, C. Mikkelsen and R. Chaplin, "Predictions of a Supersonic Jet-in-Crossflow: Comparisons Among CFD Solvers and with Experiment," in *AIAA Aviation*, Atlanta, 2014.

[115] D. Peterson and G. Candler, "Hybrid Reynolds-Average and Large-Eddy Simulation," *Journal of Propulsion and Power,* vol. 26, no. 3, 2010.

[116] P. Huang and G. Coleman, "Van Driest Transformation and Compressible Wall-Bounded Flows," AIAA Journal, 1994.

[117] E. H. Khali and Y. Yao, "Mixing flow characteristics for a transverse sonic jet injecting into a supersonic crossflow," in *53rd AIAA Aerospace Sciences Meeting*, Kissimmee, 2015.

[118] D. Peterson and G. Candler, "Hybrid Reynolds-Averaged and Large-Eddy Simulation of Normal Injection into a Supersonic Crossflow," *Journal of Propulsion and Power,* vol. 26, no. 3, pp. 533-542, 2010.

[119] J. Santiago and J. Dutton, "Velocity Measurements of a Jet Injected into a Supersonic Crossflow," *Journal of Propulsion and Power,* vol. 13, no. 2, pp. 264-273, 1997.

[120] E. Hassan, A. Hikaru, J. Boles, D. Davis and W. Shyy, "Multi-Scale Turbulence Model in Simulation of Supersonic Crossflow," in *49th AIAA Aerospace Sciences Meeting Including the New Horizons Forum and Aerospace Exposition*, Orlando, 2011.

[121] J. Anderson, Modern Compressible Flow Theory, McGraw Hill, 1990.

[122] A. Glagolev, A. Zubkov and Y. A. Panov, "Supersonic Flow Past a Gas Jet Obstabcle Emerging From a Flat Plate," *Izv. AN SSSR. Mekhanika Zhidkosti i Gaza,* vol. 2, no. 3, pp. 97-102, 1967.

[123] D. Everett and M. Morris, "Wall Pressure Measurements for a Sonic Jet Injected Transveresly into a Supesonic Crossflow," *Journal of Propulsion and Power,* vol. 14, no. 6, 1998.

[124] K. Kuo, Principles of Combustion, New York: John Wiley and Sons, 1986.

[125] I. Y. R. Glassman, Combustion, London: Academic Press, 2008.

Vita

Nehemiah Joel Williams is a graduate student at the University of Tennessee Space Institute in Tullahoma. After subsequently finishing a B.S. in Biblical studies from Philadelphia Biblical University (2004) and a B.S. in Mechanical Engineering from Temple University (2008), Nehemiah moved to Tennessee to attend graduate studies in Aerospace Engineering at UTSI. Nehemiah finished his M.S. in Aerospace Engineering (Fall 2010) and subsequently received a Pathways Internship at NASA's Johnson Space Center in Houston. He also entered the PhD program at UTSI, receiving full admission to candidacy and starting his dissertation research in the Spring 2013 semester. Nehemiah hopes to successfully defend his dissertation and finish his PhD; he eventually plans to research advanced propulsion systems in support for future human missions to Mars.